A lost Tethyan evaporitic basin: Evidence from a Cretaceous hemipelagic meta-selenite – red chert association in the Eastern Mediterranean realm

(Article begins on next page)

26 April 2024

A lost Tethyan evaporitic basin — Evidence from Cretaceous hemi-pelagic meta-selenite in the Eastern Mediterranean realm

A lost Tethyan evaporitic basin — Evidence from Cretaceous hemi-pelagic meta-selenite in the Eastern Mediterranean realm

Franziska Scheffler[1,2], Adrian Immenhauser[3], Amaury Pourteau[1,4],

Marcello Natalicchio[5], Osman Candan[6] and Roland Oberhänsli[1]

[1]University of Potsdam, Institute of Earth and Environmental Science, Karl-Liebknecht-Straße 24-25, 14476 Potsdam-Golm, Germany,

[2]Friedrich Schiller University Jena, Otto Schott Institute of Materials Research, Department of Chemistry and Earth Sciences, Fraunhoferstraße 6, 07743 Jena, Germany, Franzi.Scheffler@uni-jena.de

[3]Ruhr-University Bochum, Institute of Geology, Mineralogy and Geophysics, Universitätsstraße 150, 44801 Bochum, Germany

[4]Curtin University, School of Earth and Planetary Sciences, Bentley, Perth, Australia

[5]University of Torino, Department of Earth Sciences, via Valperga Caluso 35, 10125 Torino, Italy

[6]Dokuz Eylül Universitesi, Department of Geological Engineering, 35160 Bornova Izmir, Turkey

28 **ABSTRACT**

29 Ancient evaporite deposits are geological archives of depositional environments characterized by a

30 long-term negative precipitation balance and bear evidence for global ocean element mass balance

31 calculations. Here, Cretaceous selenite pseudomorphs from western Anatolia ('Rosetta Marble')—

32 characterized by their exceptionally morphological preservation—and their 'marine' geochemical

33 signatures are described and interpreted in a process-oriented context. These rocks recorded Late

34 Cretaceous high-pressure/low-temperature, subduction-related metamorphism with peak conditions

35 of 1.0–1.2 GPa and 300–400°C. Meter-scale, rock-forming radiating rods, now present as fibrous

36 calcite marble, clearly point to selenitic gypsum as the precursor mineral. Stratigraphic successions

37 are recorded along a reconstructed proximal-to-distal transect. The cyclical alternation of selenite

38 beds and radiolarian ribbon-bedded cherts in the distal portions are interpreted as a two type-of-

39 seawater system. During arid intervals, shallow marine brines cascaded downwards into basinal

40 settings and induced precipitation. During more humid times, upwelling-induced radiolarian blooms

41 caused the deposition of radiolarite facies. Interestingly, there is no comparable depositional setting

42 known from the Cenozoic world. Meta-selenite geochemical data (δ^{13}C, δ^{18}O values and ^{87}Sr/^{86}Sr

43 ratios) plot within the range of reconstructed middle Cretaceous sea water signatures. Possible

44 sources for the ^{13}C-enriched (mean 2.2‰) values include methanogenesis, gas hydrates, and cold

45 seeps fluid exhalation. Spatially resolved component-specific analysis of a rock slab display isotopic

46 variances between meta-selenite crystals (mean: δ^{13}C 2.2‰; δ^{18}O -0.7‰) and host matrix (mean:

47 δ^{13}C 1.3‰; δ^{18}O -2‰). The Cretaceous evaporite-pseudomorphs of Anatolia represent a basin wide

48 event coeval with the Aptian evaporites of the Proto-Atlantic and shares many attributes, including

49 lateral distribution of 600km and stratigraphic thickness of 1.5–2km, with the evaporites formed

50 during the younger Messinian salinity crisis. The Rosetta Marble of Anatolia may represent the best-

51 preserved selenite pseudomorphs worldwide and have a clear potential to act as template for the

52 study of meta-selenite in deep time.

53

54

55

56

59

60 **INTRODUCTION**

61 Sedimentary rocks are exploited by means of proxy data that serve both for hindcasting purposes but

62 also provide fundamentally important input parameters for climate models (e.g. Veizer *et al.*, 1999;

63 Fleitmann *et al.*, 2004; Della Porta, 2015; Immenhauser *et al.*, 2016). With reference to sediments

64 and sedimentary rocks in oceanic basins, work performed in the context of ocean drilling has added

65 significantly to our understanding of Earth's history, the evolution of life, and past climate dynamics

66 (e.g. Zachos *et al.*, 2001; Miall, 2013). This becomes particularly important when dealing with earth's

67 deep time record that, in many cases, has seen variable degrees of diagenetic to metamorphic

68 overprint. Deep burial and subsequent uplift or folding and thrusting in mountain belts affect

69 sedimentary rocks and commonly alter their petrographic, mineralogical, or geochemical signatures

70 (e.g. Schneider *et al.*, 2008; Swart, 2015).

71 Evaporites are peculiar amongst earth's sedimentary archives as they represent a rather

72 unique depositional environment. The nucleation of evaporite minerals and their morphologies is

73 directly influenced by environmental parameters such as salinity, temperature, and availability of

74 organic matter (e.g. Cody & Cody, 1988; Ortí, 2011; Aquilano *et al.*, 2016; Warren, 2016). Further,

75 evaporitic minerals have the potential to preserve the trace element distribution, fluid inclusion

76 composition, and isotope ratios of brines from which they precipitated (e.g. Deer *et al.*, 1992; Lu *et*

77 *al.*, 2001, 2002; Natalicchio *et al.*, 2014; Warren, 2016), and, therefore, they represent an important

78 archive for paleoenvironmental reconstructions (Warren, 1999). Nevertheless, evaporites are prone

79 to dissolution, which may result in a preservation bias in the geological record. The authors here

80 argued that the potential of meta-evaporites and their pseudomorphs as archives in the deep-time

81 geological record has been hampered by a dearth of dedicated studies. To address this, the present

82 paper explores the potential of metamorphosed Cretaceous evaporitic successions in Turkey. Meta-

83 evaporites and related meta-sedimentary rocks, now present as marble fabrics and cherts, are

84 regionally referred to as "Rosetta Marble", a casual catch-it-all-term that is applied throughout this

85 paper. Previous studies (Scheffler *et al.*, 2014, 2016) established the fundamental stratigraphic

86 distribution, lithological associations, primary versus metamorphic mineralogies, and metamorphic

87 pressure–temperature (P–T) evolution of the Rosetta Marble deposits and the reader is referred to

88 these sources for details.

89 Building on previous work, this paper takes the next step and places these findings in a

90 conceptual and process-oriented context by documenting macro- and mesoscopic sedimentary and

91 stratigraphic features of the Rosetta meta-evaporites. This includes the distribution of different

92 meta-selenite morphotypes in their respective depositional environments based on a conceptual

93 model from proximal-to-distal settings. Subsequently, the Rosetta Marble deposits are compared

94 with non-metamorphosed analogue facies from the Middle (Badenian) and Late (Messinian) Miocene

95 evaporite deposits of the Paratethys and the Mediterranean basins, respectively. Finally, light stable

96 and radiogenic isotope data (δ^{13}C, δ^{18}O, ^{87}Sr/^{86}Sr) are combined with petrographic observations to

97 assess the diagenetic pathways of these rocks and their corresponding proxy data from deposition

98 via subduction to exhumation. The data shown here highlight the potential of Cretaceous meta-

99 evaporites—conventionally not considered as suitable palaeoenvironmental archives due to their

100 high degree of recrystallization—when placed in their paleoenvironmental context and direct

101 implications for the Neotethyan palaeogeography and tectonic evolution of the Eastern

102 Mediterranean are proposed. Beyond that, this paper is of clear generic importance for those

103 interested in deep time archive research in general and has significance for reconstructions of

104 seawater salinity over geological time.

105

106 **PLATE TECTONIC SETTING, REGIONAL TECTONOSTRATIGRAPHIC FRAMEWORK, AND STUDY SITES**

107 The Anatolian microplate formed due to the collision of several microcontinents during the closure of

108 the Tethyan realm (e.g. Celâl & Yilmaz, 1981; Okay *et al.*, 1986; Şengör, 1990). Whereas northern

109 Anatolia is composed of Eurasia-derived units, the domains south of the Izmir–Ankara Suture Zone

110 were derived from Gondwana, such as the Anatolide–Tauride Block (Fig. 1). The passive margin of

111 this former microcontinent is represented by the metamorphic Ören–Afyon Zone and the thrust-and-

112 folded, low-grade to non-metamorphosed Tauride Platform (Fig. 1). The Ören–Afyon Zone and

113 Tauride Platform present a continuous Mesozoic stratigraphic sequence of Lower Triassic siliciclastic

114 rocks to Middle Triassic to Upper Cretaceous carbonaceous (marine) sediments deposited in neritic

115 to pelagic environments (e.g. Gutnic *et al.,* 1979; Candan *et al.*, 2005). The transition from neritic to

116 pelagic deposition was constrained paleontologically to Valanginian–Aptian times (Özcan *et al.*, 1988,

117 1989, 1990; Göncüoğlu, 2011). The uppermost pelagic carbonate formation correlates

118 lithostratigraphically to the Cenomanian–Maastrichtian (Özcan *et al.*, 1989; Göncüoğlu *et al.*, 1992;

119 Candan *et al.*, 2005; Cohen *et al.*, 2013). During the latest Cretaceous, the Ören–Afyon Zone were

120 overlain by olistostromal formations and serpentinite mélanges (de Graciansky, 1972; Robertson &

121 Ustaömer*,* 2009) and subducted (Pourteau *et al.*, 2013). In this process, the Ören–Afyon Zone

122 reached maximum metamorphism at around 70 Ma, coevally with ophiolite obduction onto the

123 Tauride Platform (Collins & Robertson, 1997; Pourteau *et al.*, 2016). From the Eocene to the

124 Miocene, the westernmost extension of the Ören–Afyon Zone (Ören Unit) was transported

125 southwards over the uplifting Menderes Massif (Güngör & Erdoğan, 2001; Rimmelé *et al.*, 2003,

126 2006; van Hinsbergen *et al.*, 2010; Pourteau *et al.*, 2013). Former evaporite relicts within the pelagic

127 carbonate formations are distributed widely in the Anatolide–Tauride Block (Scheffler *et al.,* 2016).

128　The present study focuses on the neritic to pelagic carbonate sequence (the "Rosetta Marble") of the

129　Ören Unit, which crops out near the villages of Fesleğen, Akçakaya, and Karaböğürtlen

130　(supplementary Fig. A).

131

132　**CASE SETTING: THE ROSETTA MARBLE**

133　Below we provide a condensed review of previous work that is relevant to the reader of this paper.

134　Please consider cited work for details. This paper refers to what has been addressed as the 'Rosetta

135　Marble' by Rimmelé *et al*. (2003), i.e. calcitic marble exhibiting three-dimensional, fan-shaped

136　morphologies resembling typical selenite megacrystals (Scheffler *et al.*, 2014, 2016). Rosetta Marble

137　in Cretaceous strata are restricted to the Ören–Afyon Zone (Fig. 1), in which they form part of the

138　upper Mesozoic hemi-pelagic sequence composed of marble–chert couplets. Analogues to this meta-

139　evaporite are lacking in portions of the Tauride platform that have not been metamorphosed to an

140　equal degree. So far, the sedimentary information archived in Rosetta Marble stratigraphic unit have

141　been underappreciated. Previous detailed stratigraphic studies did not refer to the abundant, meter-

142　sized crystal splays (Brunn *et al.*, 1970; Bernoulli *et al.*, 1974; Brinkmann, 1967; Poisson, 1977, 1984;

143　Gutnic *et al.*, 1979; Özkaya, 1990; Özer *et al.*, 2001). Candan *et al*. (2005), Rimmelé *et al*. (2005),

144　Oberhänsli *et al*. (2010), and Pourteau *et al*. (2010) described Rosetta Marble horizons and applied

145　them as markers for stratigraphic correlation in the frame of regional tectonic reconstructions.

146　Morphological attributes of calcitic Rosetta Marble crystals, revealing important similarities with

147　selenite crystals, were described by Scheffler *et al.* (2014, 2016). Imprints of minerals with typical

148　selenite morphologies in formerly soft, siliceous layers document the syn-depositional nature of

149　these minerals. Based on arguments including crystal morphologies and paleo-depositional

150　information, it is postulated that the Rosetta Marble represents pseudomorphs after selenite gypsum

151　forming cm- to m-sized, three-dimensional fans (Scheffler *et al.*, 2014, 2016). The authors inferred

152　that selenite transformed to aragonite during early diagenesis and subsequent subduction, and

153　aragonite was replaced by calcite during exhumation. In contrast, evidence that these radiating

154　calcite rods represent former aragonitic mega-botryoides nucleating and precipitating on the

155　seafloor is lacking altogether.

156　　　The Rosetta Marble deposits of the Ören Unit have been subjected to high-pressure/low-

157　temperature (HP/LT), i.e. subduction-related metamorphism, as evidenced by (i) high Sr contents

158　measured in fibrous calcite, which represent pseudomorphs after aragonite fibers (Rimmelé *et al.*,

159　2003), (ii) aragonite inclusions in quartz (Scheffler *et al.*, 2016), (iii) *P–T* estimates for pelitic layers

160　enclosing the Rosetta Marble deposits (Scheffler *et al.*, 2016), and (iv) *P–T* estimates for adjacent

161 formations (Oberhänsli *et al.,* 2001, Rimmelé *et al.*, 2003, 2005; Pourteau *et al.*, 2014). Peak *P–T*

162 conditions were estimated as 1.0–1.2 GPa and 300–400°C (Fig. 2). Following Gillet & Goffé (1988),

163 the overall lack of aragonite indicates that it was replaced by calcite above 200°C, i.e. at pressures

164 >0.5 GPa (Fig. 2). No pseudomorphs after anhydrite were found in the Rosetta Marble units. The

165 gypsum-to-carbonate transformation therefore took place before pressure–temperature conditions

166 of stable anhydrite were reached. The replacement of gypsum by carbonate can be either induced by

167 bacterial sulphate reduction or by thermochemical sulphate reduction (e.g. Machel, 2001). With

168 reference to thermochemical sulphate reduction, thermodynamically stable conditions allow for

169 gypsum to directly transform to aragonite along a subduction-type geothermal gradient

170 (<160°C/GPa; Fig. 2). Moreover, thermochemical sulphate reduction allows the preservation of

171 former evaporite morphologies as opposed to bacterial sulphate reduction that is usually attributed

172 to fabric-destructive alteration (Fernández-Díaz *et al.*, 2009). Additional evidence for thermochemical

173 sulphate reduction as main mechanism transforming selenite to carbonate comes from the elevated

174 Sr concentrations in calcite fibers (>3500 ppm) agreeing with an aragonitic replacement of selenite

175 (Scheffler *et al.*, 2016). Cathodoluminescence imaging of pseudohexagonal meta-gypsum crystals

176 shows generally concentric zonation reflecting trace element variations from core to rim. Although

177 gypsum was transformed into aragonite that was in turn pseudomorphed into calcite, a primary

178 zoning of gypsum is preserved and suggests a relative immobility of the trace elements during

179 metamorphism and neomorphosis (Scheffler *et al.*, 2016).

180

181 **MATERIALS AND METHODS**

182

183 **Field work and sample material**

184 Extensive fieldwork was performed in the Ören Unit, south-west Turkey. Structural and stratigraphic

185 data were collected along three measured sections. Particular care in sampling was taken to avoid a

186 stratigraphic bias induced by faults and folds. Criteria to establish the lithostratigraphic orientation of

187 strata in three dimensions included erosional surfaces, fluid-escape structures, and characteristic

188 growth textures of evaporites. Rock samples of meta-carbonate, meta-sandstone, and meta-chert

189 were collected and processed for petrographic examination (thin sections) and geochemical analysis.

190

191 **Optical analyses**

192   32 polished thin section were investigated with optical polarization microscopes at Potsdam

193   University (Leica DMRXP) and Friedrich-Schiller-University Jena, both Germany (AXIO Zeiss

194   Imager.M2m, AudioCam MRcS Zeiss). The HC6-LM Cathodoluminescence microscope at Potsdam

195   University was used at 14 kV with a beam current of 0.2 mA and an operating vacuum of $5*10^{-4}$

196   mbar. A coupled polarized light microscope allows for navigation and documentation. Samples were

197   carbon coated to avoid electrical charging. Cathodoluminescence images were used to choose

198   appropriate minerals for isotope analysis, because altered and primary areas can be distinguished.

199

Geochemical analyses

201   184 rock powders for isotope analysis were produced by using a low-speed micro-drill equipped with

202   diamond-studded drilling heads. Homogeneous sample sides were drilled on freshly cut and cleaned

203   rock slabs. Micro-drilled carbonate powders were analyzed for their carbon (δ^{13}C) and oxygen (δ^{18}O)

204   isotopic values using a Thermo Fisher Scientific Gasbench II carbonate device coupled to a Thermo

205   Fisher Scientific Delta S Isotope Ratio Mass Spectrometer at Ruhr-University, Bochum, Germany.

206   Isotopic values were standardized to V-PDB. See Christ *et al.* (2012) for details on lab-specific

207   analytical procedures. The uncertainty on the plotted values is equal or smaller than 0.06‰ for δ^{13}C

208   and 0.1‰ for δ^{18}O. Strontium isotopes (^{87}Sr/^{86}Sr) were analyzed using a Finnigan MAT 262 thermal-

209   ionisation mass spectrometer (TIMS) at Ruhr-University Bochum, Germany. ^{87}Sr/^{86}Sr sample

210   corrected to difference: NBS 987 value McArthur and NBS 987 Bochum mean value. Refer to Geske

211   *et al.* (2012) for lab-specific analytical details. The maximal error for ^{87}Sr/^{86}Sr is $\pm 2\sigma_{mean}$ = 0.000008.

212   Stable and radiogenic isotope analytical results are given in the supplementary material.

213

DATA PRESENTATION

215

Stratigraphy and Sedimentology

217   Two types of end member facies were identified. One is build up by grayish, thickly bedded (up to 2

218   m) marble successions with intercalated calcareous quartzite (medium to coarse grained meta-

219   sandstone) beds and occasional whitish to grayish aligned nodular and ribbon bedded chert (Fig. 3A;

220   type locality Fesleğen: N 37°03.396'' E 27°47.457''). Meta-sandstones locally display fine lamination,

221   a fining-upward trend and they are occasionally overlying an irregular erosional surface. All of these

222   attributes suggest a turbiditic origin of these beds. The other end member facies is present in the

223   form of reddish, thinly bedded (cm's to a few dm's) marble-chert alterations, intercalated with thin

224   radiolarian-bearing meta-wackestones (Fig. 3C; type locality Karaböğürtlen: N 37°04.388'' E

225   28°34.081''). Intermediate types include grayish marble beds (several dm's thick) alternating with

226   whitish cherty beds and nodules (Fig. 3B; type locality Akçakaya: N 37°04.588'' E 27°51.042'';

227   supplementary Fig. A).

228   Three sections representing the three Rosetta Marble facies associations (type localities)

229   were sampled for O, C, and $^{87}Sr/^{86}Sr$ isotope analysis: The Fesleğen, the Karaböğürtlen, and the

230   Akçakaya sections. The Fesleğen section consists of thickly bedded marble beds, rarely intercalated

231   with chert layers and nodules (Fig. 4 and supplementary Fig. C). In the stratigraphically lowermost

232   part, calcareous-sandy turbiditic horizons are common features. The marble layers are mainly

233   composed by fans of large selenite-pseudomorphs. Occasionally, these fans are embedded in a dark

234   grey marble matrix. The upper part of the section contrasts with the lower intervals and is mainly

235   built by a regular alternation of marble beds bearing gypsum-pseudomorphs and a few cm-thick

236   chert layers. The Karaböğürtlen section show two intervals characterized by their different facies

237   associations. The lower one is composed of rather uniform thickly to moderately bedded meta-

238   selenite–chert alternations (Fig. 5A, D and supplementary Fig. D). The frequency of chert beds

239   increases upsection and their thickness decreases. The upper interval of the section consists of a

240   reddish, thinly bedded marble-chert alternation (Fig. 5A, B and E). Chert ribbons are in part

241   embedded in a host facies of meta-wackestones rich in radiolaria tests. The third section, located

242   near the village of Akçakaya, shows a facies pattern that is intermediate between the Karaböğürtlen

243   and Fesleğen endmember sections. Based on its structural position, the Akçakaya section is most

244   likely stratigraphically older than the Fesleğen section. These rocks consist of very regular thickly to

245   medium thickly bedded selenite-pseudomorph bearing marble-chert alternations but they are devoid

246   of the turbiditic meta-sandstones typical for the Fesleğen locality. Generally, these units are

247   lithological homogeneous in their appearance relative to the more diverse other sections

248   (supplementary Fig. E).

249

250   **Morphological features and growth orientation of meta-selenites**

251   Meta-selenite textures display a variety of systematic morphotypes (growth forms and crystal habit).

252   The most common ones are described in the following (Figs 6 to 8).

253

254   *Selenite growth orientation*

255 Four main growth orientations of selenite pseudomorphs, relative to the bedding plane, are

256 recognized: (i) upward growth (Fig. 6A and B); (ii) downward growth (Fig. 6C), (iii) up- and downward

257 growth (Fig.6D, E and F), and (iv) horizontal/in-plane orientation (Fig. 7A and B).

258 Upward growing meta-selenites ('Rosettas') are predominantly fan or dome shaped (Fig. 6A).

259 Tilted crystal fans (subparallel to the bedding plane) are frequently observed (Fig. 6B). Downward

260 growing meta-selenite fans/domes (Fig. 6C) are uncommon. Up- and downward oriented fans are

261 comparable in size and symmetrical. The nucleation points are aligned with chert-ribbons and –

262 nodules (Fig. 6A-D); often, the top of a lower crystal fan serves as nucleation for the next crystal

263 dome (Fig. 6A) or they grow from impurity-rich surfaces (Fig. 6E). Selenite fans growing from a

264 nucleation point devoid of silica are restricted by top and bottom chert/marble-layers (Fig. 6F).

265 Amongst the horizontally growing (in-plane) Rosetta fans (Fig. 7), three subtypes can be

266 identified: (i) Radial Rosettas with long crystal rods radiating from a central nucleation site; (ii)

267 flower-like Rosettas showing basal sections of crystals in the centers of the radiating fans. Small rods

268 radiate away and gradually change to longer crystals with increasing distance to the center; and (iii)

269 concentric Rosettas. Here, long rods start radiating from a certain distance to the rod-free center.

270 The diameters of individual fans are remarkable and may reach 3 m. The length of individual meta-

271 selenite crystals within fans range from a few cm's to 1.5 m's (Fig. 7A). Where fans compete for

272 space, typical features of converging crystallization fronts are observed (Fig. 7B). Where fans are

273 spatially separated, crystals grow idiomorphic and form mega-crystals.

274

275 *Selenite crystal habits and morphotypes*

276 The most common morphotypes and crystal habits of selenite pseudomorphs are cm- to meter-long,

277 straight to curved-radiating rods composed of calcite crystals (morphotype i, Fig. 7). Many marble

278 layers are mostly made up of calcite Rosettas with only limited amounts of fine-grained matrix (Fig.

279 7). Locally, calcite rods are embedded in a fine-crystalline homogeneous dark grey marble matrix (Fig.

280 8A). A thin layer of marly-quartzitic sediment often fringes individual calcite rods (Fig. 8A, Scheffler *et*

281 *al.*, 2016). Less common morphotypes are: (ii) stacked swallowtail crystals (Fig. 8B), (iii) fishbone-like

282 crystals, restricted to coarse-grained sandy levels (Fig. 8C), (iv) Christmas-tree shaped selenites

283 pseudomorphs similar to dendritic habits (Fig. 8D), (v) flower-like arranged curved sabre crystals (Fig.

284 8E), and (iv) crystals forming palisade layers (Fig. 8F).

285

286   *Petrography and mineralogy: microscale crystal habits and their relation to matrix and meta-*
287   *radiolarites*

288   The selenite pseudomorphs are composed of fibrous calcite that in turn is a pseudomorph after
289   aragonite. The material that often fringes individual meta-selenite crystals comprises microcrystalline
290   quartz, dolomite rhombs, mica, and opaque accessory phases (Fig. 9A and B). Monoclinic crystals
291   habits (former gypsum) are visible in the case of small (mm-scale) rods floating in matrix meta-
292   sediments (Fig. 9A to D). Crystal habits resemble elongated rods or pseudo-hexagonal sections
293   (perpendicular to the c-axes of the rods) with crystallographic angles typical for gypsum (Buick &
294   Dunlop, 1990; Fig. 9D). Within the pseudo-hexagonal crystal outlines calcitic pseudomorphs after
295   aragonite fibers are mostly well preserved (Fig. 9E). The contact between meta-selenite marble and
296   chert layers is usually distinct and rather abrupt (Figs 9F and 10A). Chert layers consist of a ribbon
297   bedded or nodular siliceous core and an increasingly dolomitic outer zone (Fig. 9F). Insoluble material
298   and minor calcite crystals increase in number towards the chert-rich center of individual beds (Fig.
299   10A). Raman spectroscopy indicates that dolomites were in part dedolomitized and are now calcitic
300   or dissolved. Some of these dedolomitized rhombs exhibit an internal zonation. Molds with a
301   rhombic habit are common on the weathered and fresh sample surfaces, most likely indicating
302   former dolomite crystals. Calcified relicts of radiolarian tests are present in meta-wackestone layers
303   (Fig. 10B) whereas microcrystalline silicified radiolarian tests are preserved within chert layers (Fig.
304   10C and D). The degree of preservation of altered radiolarian tests changes from locality to locality
305   and ranges from neomorphosed but morphologically well-preserved to barely recognizable.

306   Under cathodoluminescence imaging, different crystallization stages and fluid-related
307   alteration are recognized. Authigenic carbonate after gypsum appears in dark bluish-blackish
308   luminescence colors, whereas the surrounding, recrystallized fine-grained matrix displays orange
309   luminescence (Fig. 11). Under normal light microscopy, zoning of pseudohexagonal crystals is not
310   obvious. These crystals show, however, four, arguably primary and distinct cathodoluminescence
311   zones (Fig. 11A). This is considered remarkable when taking the complex metamorphic pathway of
312   these rocks into consideration.

313

314   **Geochemical data**

315   *Carbon and oxygen isotope data of selenite pseudomorphs and stratigraphic patterns in carbon*
316   *isotope signatures*

317   Most of the bulk δ^{13}C values obtained from selenite pseudomorphs and their bulk sediments (*matrix*)

318   plot within the range of reconstructed mean mid-Cretaceous sea water DIC (0.3 – 3.2 δ^{13}C) and even

319   the oxygen isotope data are only moderately depleted in ^{18}O (0 to -3.1 δ^{18}O; Fig. 12, Veizer *et al.*,

320   1999). Carbon and oxygen isotope data show cluster that fit with their sampling sites and

321   stratigraphic levels (Fig. 12, Table 1). Although Bodrum samples are lacking selenite pseudomorphs,

322   they yield similar values as the other localities in which selenite pseudomorphs are observed.

323   The data serve to test if stratigraphic facies changes are detectable in their bulk geochemical

324   pattern. For details on the carbon, oxygen, and radiogenic strontium isotope data from all three

325   sections, refer to figures 5, 12, 13 and tables 1 and 2. Additional figures and extended data tables can

326   be found in the digital appendix. Below we briefly describe the isotope trends for each facies.

327   In the Fesleğen section, the transition from the lower (selenite bearing marble layers with

328   rare cherts and intercalated quartzite) to the upper (marble-chert couplets) section is well depicted

329   by the isotope pattern (supplementary Fig. C). Carbon bulk isotope values from the upper part of the

330   section yield slightly heavier values (mean: 2.2‰) than samples from the lower part of the section

331   (mean: 2.0‰; Table 1). In the Karaböğürtlen section, the upper part exhibits the most ^{13}C-enriched

332   carbon isotope (mean: 3.3‰) whereas the lower part is consistent with the majority of measured

333   samples (mean: 1.7‰; Fig. 5E, Table 1, supplementary Fig. D). The oxygen isotope values are lower in

334   the upper (mean: -2.7‰) than in the lower part of the section (mean: -1.3‰). Fife samples from the

335   upper part of the section show the lowest oxygen isotope values (mean: -4.4‰; Figs 12 and 13). In

336   the Akçakaya section, C and O isotope values display an invariant pattern, mirroring the absence of

337   major lithological changes (Table 1). Nevertheless, carbon (mean: 1.3‰) and oxygen (mean: -2‰)

338   curves have their lows and highs at the same positions and hence display covariance (supplementary

339   Fig. E). δ^{13}C values of all three sections plotted in one diagram show an offset of 4‰ in the upper

340   portions (Fig. 13).

341   Although the ^{87}Sr/^{86}Sr isotope values in this study are limited, they show an interesting trend

342   similar to those of carbon (and oxygen) isotope values. In the Fesleğen section, ^{87}Sr/^{86}Sr isotope

343   ratios are slightly less radiogenic in the upper part of the section (mean: 0.707522) and more

344   radiogenic in the lower part (mean: 0.707551). In the upper red part of the Karaböğürtlen section the

345   ^{87}Sr/^{86}Sr ratios continuously increase (mean: 0.7075578) with a peak value upsection, that coincide

346   with a color change to yellow (Fig. 5E, Table 2). In the lower portion, lower ^{87}Sr/^{86}Sr values are

347   measured (mean: 0.7074066). The Akçakaya section shows no chemostratigrahic variances in

348   ^{87}Sr/^{86}Sr isotope values (mean: 0.707368).

349

350   *Spatial distribution of carbon and oxygen isotope values across a selenite-pseudomorph and its host*

351   *sediment*

352   A total of 36 samples for carbon and oxygen isotope analyses were drilled in a selenite-pseudomorph

353   rock slab (Fig. 14). Carbon isotopes within meta-selenite-crystals (i) are clearly enriched in [13]C (mean:

354   2.2‰), whereas the host sediment is depleted (mean: 1.7‰). The host sediment can be separated in

355   (ii) matrix, (iii) matrix with small meta-selenite crystals and (iv) rod-fringing material. The matrix

356   *sensu stricto* exhibits the lowest δ^{13}C values (mean: 1.3‰). Although δ^{18}O isotopes in metamorphic

357   rocks are potentially strongly overprinted, a purely descriptive subdivision of different clusters of

358   isotope data becomes obvious: (i) selenite-pseudomorphs (mean: -0.7‰), (ii) matrix (mean: -2‰),

359   (iii) matrix with small meta-selenite crystals (mean: -1.2) and (iv) rod-fringing material (mean: -0.2‰;

360   supplementary figures F and G).

361

362   **INTERPRETATION AND DISCUSSION**

363

364   **Sections studied in the bathymetric context of a lost Cretaceous evaporitic basin**

365   Morphological features evidencing former selenite mega-crystals were reported from Rosetta Marble

366   localities across the 400-km-long Ören–Afyon Zone (Scheffler *et al.*, 2016). The widespread

367   distribution of these peculiar stratigraphic intervals in the uppermost part of the Mesozoic carbonate

368   sequence, bears witness to a middle Cretaceous evaporitic basin, now mostly lost in a subduction

369   zone during Late Cretaceous to Early Paleocene times. Middle Aptian palaeogeographic

370   reconstructions of the Mediterranean area (Barrier & Vrielynck, 2008) depicted the Ören–Afyon Zone

371   as part of a deep-marine basin bordered to the south by extensive shallow-marine areas represented

372   by the shelf carbonate sequences of the Tauride Platform. Remnants of the evaporitic, turbiditic, and

373   siliceous sedimentary cover of this basin (or these basins) are now exposed in the sections discussed

374   in the context of this paper. Acknowledging the considerable difficulties resulting from an attempt to

375   reconstruct a former basin based on incomplete, spatially separated sections that are only indirectly

376   dated by means of regional correlations (e.g. Özcan *et al.*, 1989; Göncüoğlu *et al.*, 1992; Candan *et*

377   *al.*, 2005), some tentative suggestions are made and their implications discussed. To reconstruct the

378   internal architecture of the evaporitic basin, the three studied stratigraphic successions are restored

379   along a proximal-to-distal transect (Fig. 15). The observed facies associations reflect slope to basinal

380   domains. Thick-bedded, graded sandstone is ascribed to the relatively proximal, i.e. base-of-slope

381 environments, whereas radiolarite (now chert) are pelagic deposits and generally a predominant

382 component of the most distal formations.

383   Meta-evaporites as such are not diagnostic of any specific bathymetric domain since

384 evaporites precipitate from hypersaline water masses that may form on the shelf or in basins

385 (Warren, 1999). Schmalz (1969) pointed out that the precipitation of evaporites in (marginal) basinal

386 settings takes place where parental brines underlie waters of normal salinity. These dense fluids do

387 not mix with marine surficial waters and sink to the floor of basins. Roveri *et al.* (2014) reported on

388 recent Mediterranean high density fluids forming at shelf levels and cascade downwards to the basin

389 center. These 'Dense Shelf Water Cascading' (DSWC) currents play an important role in shelf erosion

390 and sub-marine canyon formation (Roveri *et al.*, 2014). Two high-salinity-water-producing scenarios

391 are proposed: (i) silled shallow sub-basins that suffered periodically spillovers and subsequent

392 desiccation forming hypersaline brines or (ii) cascading semi-dense waters that accumulate in deep

393 marine basins and get to the oversaturation state down there. On the base of these considerations,

394 Roveri *et al.* (2014) supported a deep-water–deep-basin-model (e.g. Schmalz, 1969; Hsü *et al.* (1973)

395 ; Debenedetti, 1982) for the long standing debate on the formation of Messinian saline giant.

396   The lower part of the Fesleğen section comprises predominantly thickly bedded (proximal)

397 turbidite intervals. This significant terrigenous influx is evidence that the lower Fesleğen section

398 represents the most proximal (landward) environment among the Rosetta Marble sections studied

399 here (Fig. 15). Upsection, the proportion of meta-selenite and then of meta-radiolarite increases,

400 depicting an overall deepening upward trend or an increasing production of radiolarian tests

401 potentially assigned to enhanced upwelling.

402   Thickly bedded marble–chert couplets, such as exposed in the upper Felseğen section, the

403 Akçakaya section, and the lower Karaböğürtlen section, represent occasional turbidite deposition

404 alternating with prolonged periods of hemi-pelagic radiolarite sedimentation and agree with a more

405 distal depositional environment. Bedded hemi-pelagic carbonate successions exposed on the

406 Bodrum Peninsula and in the Taurides lack intercalations of meta-selenite deposits. The reason for

407 this is not entirely understood but might suggest a more open and better circulated environment

408 that did not allow for evaporitic brines to assemble.

409   The Karaböğürtlen section (Figs 5 and 15) consists of thinly-bedded meta-radiolarite–meta-

410 selenite couplets. Meta-wackestone layers fringing specific chert ribbons are common in the upper

411 part of the section but absent in the lower part. The section is potentially indicative of a deepening-

412 upward trend and may represent the most distal and most basinal setting of the transect studied.

413

414 **Interpretation of the selenite–radiolarite couplets**

415 The cyclical alternation of large selenite crystals with beds of radiolarian cherts is uncommon in the

416 geological record (Warren, 1999) and requires discussion. The main problem lies in the fact that

417 radiolarian facies commonly indicates an open shelf or even a basinal depositional environment

418 whereas meter-scale selenite crystal formation is often typical of smaller marginal evaporitic settings

419 (e.g. Bąbel, 1987; Ortí, 2011). When comparing the studied sections with the Messinian evaporites in

420 the Mediterranean realm, selenite nucleation and growth is restricted to silled, marginal basins with

421 bathymetries of not more than about 200 meters (Lugli *et al.*, 2010). No examples of meter-long

422 selenite crystals forming at these depths are known from the Cenozoic. Moreover, in bathymetric

423 ranges below the neritic domain (> 200 m), the formation of sulphate evaporites is likely inhibited by

424 high rates of bacterially-promoted sulphate reduction via degradation of organic matter (De Lange &

425 Krijgsman, 2010; Garcia-Veigas *et al.,* 2018).

426 In the most distal Rosetta Marble facies associations (upper Karaböğürtlen section; Fig. 15),

427 remarkably well-preserved radiolarian pseudormorphs in meta-chert and in radiolarian-rich meta-

428 wackestone might be indicative of a higher abundancy of radiolaria and of higher productivity. Other

429 factors such as overall lower sedimentation rates or differential pathways of silica diagenesis should

430 not be excluded at this state. Occasionally, radiolaria thrive in neritic water masses, mainly in the

431 context of upwelling systems (Nigrini & Caulet, 1992, and references therein) but the excellent

432 preservation of sedimentary structures in these sections suggests a bathymetric range beneath the

433 reach of storm waves (Immenhauser *et al.*, 2008), i.e., water depths in excess of 100–200 meters or a

434 shallower protected setting. The lack of fabric destructive bioturbation is perhaps best explained by

435 elevated porewater salinity.

436 Deposition and preservation of shallow-water, siliceous radiolaria facies require two

437 boundary conditions: (i) a radiolarian bloom in the surficial water masses, and (ii) the absence of

438 significant amount of detrital and carbonate influx to the site of deposition of the radiolarian facies.

439 It must be emphasized that the rocks studied are not radiolarian limestones but genuine radiolarian

440 cherts.

441 Two tentative depositional scenarios offer themselves that might explain the alternation of

442 chert-evaporite couplets (Fig. 15): (i) One scenario (the chert-turbiditic sandstone mode) reflecting

443 more humid conditions in the hinterland with active riverine transport of siliciclastic material through

444 turbidity currents in the more marginal setting. In more open shelf zones, upwelling of basinal water

445 might have triggered radiolarian blooms resulting in the deposition of siliceous deposits. The dilution

446 of coastal seawater by riverine influx combined with upwelling of normal marine seawater inhibited

447   evaporite formation. (ii) The second scenario (the evaporite mode) involves more arid conditions

448   leading and reduced riverine influx. This leads to the formation of near-costal evaporated water

449   masses sinking downslope (density cascading) where they accumulate in marginal basins. The

450   observation that Rosetta selenite crystals are large in size but low in number, points to a lower

451   salinity and the formation of a limited number of selenite nuclei (e.g. Lugli *et al.*, 2010). A typical

452   salinity range in modern selenite depositional environments is 110-300 g/l (e.g. Ortí, 2011;

453   Natalicchio *et al.,* 2014), corresponding to typical Sr contents of 1000-2600ppm (Ortí *et al.*, 1984).

454   The cyclical alternation of carbonate–chert couplets may (or may not) be ascribed to

455   astronomical-driven climatic fluctuations. By analogy with Messinian mudstone–gypsum precessional

456   cycles of the Mediterranean Basin (e.g. Dela Pierre *et al.*, 2011; Manzi *et al.*, 2013), a 20-kyr duration

457   of each evaporite-radiolarite cycle seems at least possible. In the absence of a reliable age model for

458   these rocks, this debate, however, must remain entirely speculative at present.

459

460   **Rosetta selenites interpreted in their environmental context and comparison with analogue**

461   **deposits**

462   *Factors controlling gypsum morphologies*

463   Laboratory experiments documented that gypsum morphologies are influenced by factors such as

464   the degree of evaporation, the presence or absence of other evaporite minerals, the brine

465   temperature, the amount of organic matter, and the seawater pH (e.g. Cody & Cody, 1988; Aquilano

466   *et al.*, 2016). Cody & Cody (1988) for example, argued the presence of significance amounts of

467   organic matter may lead to rosette-shaped growth forms. Given that few (perhaps none?) natural

468   evaporite depositional environments are devoid of organic matter, this notion seems difficult to

469   place in context in the studied deposits. Moreover, crystals that precipitate from warmer seawater

470   tend to be larger and more idiomorphic in nature (Cody & Cody, 1988). All of these considerations

471   are potentially valuable but given that the interpretation of field evidence in these metamorphic

472   rocks is less than trivial, it remains unclear to what degree these experiments can be applied to the

473   case example described here. In the view of the authors, it is thus perhaps more helpful to make use

474   of a contrast-comparison with the much better studied Messinian (Late Miocene) and Badenian

475   (middle Miocene of the central Paratethys; Hohenegger *et al.*, 2014; the top Burdigalian to the mid-

476   Serravalian, i.e., 18.3 to 16.3 Ma) evaporite deposits (Figs 16 to 18).

477

478   *Upward radiating selenite fans*

479   One of the chief characteristics of the meta-selenites discussed here is the significant length of

480   individual crystals reaching up to 1.5 meters. In order to allow for these large crystals to form, a

481   precipitation environment that provides stable physico-chemical conditions over long periods (likely

482   months and years) and a sufficient fluid oversaturation is required. In general, large crystals are the

483   result of slow growth rates and salinity conditions close to equilibrium (e.g. Rosell *et al.*, 1998).

484   Upward-growing selenite gypsum fans form dome-like structures and are common both in modern

485   and in ancient evaporitic environments (Bąbel, 2007; Lugli *et al.*, 2010; Ortí, 2011). Crystal growth is

486   initiated from a nucleation point at the sediment-water interface and crystals continue to grow in a

487   radial array as long as open space and an SO_4-saturated brine is present. In the case of the meter-

488   sized Rosetta meta-selenite fans, nucleation of crystalline gypsum took place on a seafloor formed by

489   fine-grained siliceous sediments (Fig. 16A). Due to increasing weight of the selenite fans, the

490   evaporites sunk into siliceous sediments at the seafloor creating load structures (Fig. 16A). This is

491   considered clear evidence for a syndepositional, as opposed to diagenetic, origin of these features.

492   Perhaps in analogy with the meta-selenites observed in the Anatolian Rosetta Marble, giant selenite

493   crystals (Fig. 17C and D) and palisades made up of stacked swallow-tail twinned crystal (Fig. 17E and

494   F) are a common texture of both Badenian (e.g. Bąbel, 1987) and Messinian (e.g. Lugli *et al.*, 2010;

495   Ortí, 2011) evaporite deposits. The abundant radiating fans of crystals observed in the Anatolian

496   meta-selenite fabrics have similar analogues in the Miocene deposits represented by domal- or radial

497   fan-like structures (Figs 18A and C). Tilted upward oriented selenite fans observed in the Rosetta

498   Marble share similarities with such from the Badenian evaporites explained as the results of

499   unidirectional currents (e.g. Bąbel, 2005). Sabre-like crystals are typical features of the Rosetta

500   Marble and form bundles up to 1.5 m in length. Sabre-like curved crystals are frequently found in

501   Miocene evaporite deposits and occur in bundles or as individual crystals with variable dimensions

502   embedded in a fine-grained matrix (Fig. 19A to D).

503

504   *Bedding-parallel selenite fans*

505   Bedding-parallel selenite fans show a range of morphotypes (Fig. 16). Formation models that provide

506   an explanation of all three categories (central point, flower-like and concentric) include the following:

507   (i) cutting effects at the outcrop scale and (ii) restricted growth (Fig. 16D). In the first case, upward

508   oriented, domal crystal arrays are amalgamated. Individual crystals within each fan can be straight or

509   curved depending on the environmental conditions during growth. Truncation of these fans by

510   erosion (turbidites or less saline waters causing a dissolution of the uppermost layers) may lead to

511   central point (i) (straight rods) and flower-like (ii) (curved rods) horizontal crystal fans oriented

512   parallel to bedding planes. In the latter case, bedding parallel growth is considered a primary feature

513   resulting from a shallow pycnocline and a limited number of crystallization nuclei (e.g. Lugli *et al.*,

514   2010). Small rods in the center of Rosetta textures were likely restricted by the shallow pycnocline

515   and ceased to grow when reaching the upper boundary of the brine layer. A similar mechanism was

516   proposed for the Messinian "branching selenite facies" (Lugli *et al.*, 2010), a peculiar type of

517   evaporite showing growth habits that are more laterally than vertically oriented. Concentric

518   horizontal Rosettas may have formed on the seafloor when the pycnocline was extremely shallow. In

519   addition, subsequent compaction by overlying sediments causing an extra flattening of these

520   features cannot be excluded.

521

522   *Downward-oriented selenite fans*

523   With reference to downward-oriented selenite fans, only few analogues exist in the geological record

524   (Ayllon-Quevedo *et al.*, 2007) and in the Recent (Fig. 18A and C). Clearly, this growth fabric is the

525   most challenging encountered in the Rosetta Marble facies, but perhaps also the most spectacular

526   one. Similar to upward-oriented selenite fans, crystal growth is initiated from a central nucleation

527   point at the seafloor and subsequently, selenite rods grow downwards and displace the host

528   sediment. This processes as such is not an uncommon feature and the displaced host sediment can

529   either be incorporated in the crystal lattice as solid inclusions or pushed away from the crystallization

530   front. In a study from the Laguna Madre (Texas), McBride *et al.* (1992) describe two fabrics of

531   gypsum growing in terrigenous sands in the phreatic zone. The former results from the slow (non-

532   displacive) precipitation of gypsum between quartz sand grains forming a cement phase. The other

533   fabric is the fast growth mode; here gypsum that is largely free from sand particles and displaces the

534   host sandy sediment and forms limpid crystal clusters up to 50 cm large. If the Laguna Madre gypsum

535   deposits represent to some degree analogue precipitates, then the downward-oriented radial arrays

536   typify periods of very rapid, displacive gypsum growth from highly-supersaturated pore fluids in very

537   soft siliceous sediment and a pycnocline that was essentially at the seafloor. Nevertheless, these

538   replacive or displacive fabrics are not well understood in terms of their formation and problems were

539   discussed for mainly calcitic syntaxial overgrowth cements. It seems at least possible that that the

540   original sediment was made up of gypsum-rich ooze subsequently replaced by the diagenetic

541   selenites. Modern case examples documenting perhaps similar processes include the 'Daisy-head

542   gypsum' from Texas and the 'Daiys-bed gypsum' from Cumbria, UK (Warren *et al.*, 1990). There,

543   phreatic fluids slowly infiltrate an anhydrite bed and radiating gypsum crystals grow pervasively,

544   often with a dolomite crystal as nucleation center. Brecciation is a typical phenomenon in evaporitic

545   rocks witnessing solution-induced collapse (e.g. Swennen *et al.*, 1990). In the pseudomorphosed

546 meta-selenite unit in Turkey, brecciation of fine laminated gypsum layers was recognized in at least

547 one outcrop (Fig. 18 E and F).

548

Interpretation of meta-selenite geochemical data in the context of subduction and exhumation

pathways

Bulk carbon isotope data

552 Bulk $\delta^{13}C_{meta-selenite}$ data (mean: +1.8‰) plot within the range of reconstructed middle Cretaceous

553 seawater DIC values (Fig. 12; Veizer *et al.*, 1997). Obviously, this comparison must be taken with care

554 as the Veizer *et al.* (1997) data are chiefly based on biogenic calcite as opposed to the rock samples

555 discussed here.

556   The transformation of selenite to aragonite during burial diagenesis and following

557 metamorphism in the context of subduction clearly affected the isotope signatures of the meta-

558 selenites. Bacterial sulphate reduction and thermochemical sulphate reduction are the most

559 common processes known to guide the transformation reaction from sulphate to carbonate (Machel,

560 2001). Both processes are expected to lead to ^{13}C-depleted carbon isotope values (Rouchy *et al.*,

561 1998). Bacterial sulphate reduction is a process that commonly obliterates the former gypsum crystal

562 morphologies (Machel, 2001). In the case of Anatolia's Rosetta Marble, even subtle morphological

563 features of the gypsum crystals (swallow-tails, skeletal-fibrous crystals, twin planes etc.), are

564 preserved. Hence, bacterial sulphate reduction is ruled out here. Conversely, thermochemical

565 sulphate reduction is known to result in gypsum pseudomorphs that preserve morphological features

566 of their precursor minerals (Fenandés-Díaz *et al.*, 2009). Thermochemical sulphate reduction along a

567 subduction geotherm takes place at temperatures of 100–180°C (Machel, 2001) but within the

568 pressure field of aragonite (Fig. 2). This interpretation is in line with the observation that Sr

569 concentrations of the selenite pseudomorphs (up to 3500 ppm) are elevated. Given that the calcite

570 crystal lattice does not favor the incorporation of Sr, in contrast to that of aragonite (Katz et al.,

571 1972), the direct transformation of selenite to aragonite is favored here. The obvious problem in this

572 chain of arguments lays with the interpretation of the what seem marine seawater DIC ratios of the

573 Rosetta Marble which requires a discussion of the carbon sources during selenite-to-carbonate

574 transformation.

575   In the context of transformation processes during subduction, several possible carbon

576 sources must be considered. Seawater stratification combined with a restricted exchange of oxygen-

577 depleted brines with marginal basins—as well as suboxic intraformational brines—favors the

578   accumulation of organic-rich deposits (e.g. Roveri *et al.*, 2016). Whereas the Messinian deep-water

579   evaporites exhibit a high petroleum potential (Roveri *et al.*, 2016), the TOC of the Rosetta Marble is

580   low (<0.18%) but organic material rapidly decomposes at temperatures about ca. 160°C (Machel,

581   2001) and it is mainly kerogen and bitumen that remains. During the subduction (Fig. 2), the well-

582   defined pressure–temperature field is reached where most organic matter has transformed to gas

583   and bitumen has been transformed to graphite (Staplin, 1969). Methane as a possible reactant is

584   reactive, mobile, and is largely available (Machel, 2001). Methane is the final product of several

585   disintegration processes, indicating that larger molecules could be the primary source of CH_4. To

586   interpret the rather ^{13}C-enriched values of the Rosetta Marbles, several carbon sources have to be

587   taken into account. Most CH_4 sources display strongly ^{13}C-depleted values (Peckmann & Thiel 2004):

588   These include biogenic, bacterial and microbial methane (between -50‰ and -110‰; Whiticar *et al.*,

589   1986; Whiticar, 1999), thermogenic and non-bacterial methane (-30‰ to -50‰; Sackett, 1978),

590   geothermal, hydrothermal and crystalline methane (-20‰; Botz *et al.*, 2002 and references therein),

591   and petroleum (-25‰ to -35‰; Roberts and Aharon, 1994). These CH_4 isotope signatures may result

592   in carbonate rocks with distinctive and highly variable δ^{13}C values such as the gas hydrates associated

593   carbonates (-60‰; Bohrmann *et al.*, 1998; Greinert *et al.*, 2001), and the mud volcanoes and

594   methane seep carbonates (-60‰ to +36‰; Clari *et al.*, 2004; 2009; Pekmann and Thiel, 2004;

595   Natalicchio *et al.*, 2012; Tassi *et al.*, 2012; Oppo *et al.*, 2013;). In addition, a mantle-derived carbon

596   source exhibits δ^{13}C values in the range of -3‰ to -8‰ (Pineau & Javoy, 1983; Des Marais & Moore,

597   1984; Mattey *et al.*, 1984). Gas mixtures of different carbon sources due to vertical or lateral gas and

598   fluid migration and diffusion are common and complicates the interpretation of the isotope data

599   obtained here. In the following, the carbon isotope fractionation processes related to thermogenic

600   and bacterial methane production (methanogenesis) and to gas hydrates and cold seep carbonates

601   formation are considered in more detail.

602   The $\delta^{13}C_{CH_4}$ of thermogenic gases becomes progressively enriched in ^{13}C with increasing

603   maturity, eventually approaching the ^{13}C/^{12}C of the original organic matter or kerogen (and rarely

604   even heavier) (Whiticar, 1999). However, the resulting values remain negative. In situ produced CH_4

605   by methanogenesis (CH_3-A + H_2O → CH_4 + CO_2 + A-H) is a common reaction in modern wetlands

606   (Whiticar, 1999). The CO_2 and CH_4 byproducts generated through methanogenesis (bacterial

607   methane formation by carbonate reduction) show very distinct carbon isotopic compositions with

608   ^{13}C-rich CO_2 and ^{13}C-poor CH_4 products (Whiticar, 1999; Pierre *et al.*, 2002; Natalicchio *et al.*, 2012).

609   This might imply that CO_2 instead of CH_4 was involved in the sulphate reduction reaction of Anatolian

610   precursor gypsum. This is because, in-layer produced C could be isotopically similar to rock-buffered

611   δ^{13}C values. Molecules with lower isotopic mass diffuse and react more rapidly and thus are utilized

612   more frequently than the isotopically heavier species (Whiticar, 1999). In a rock dominated system,

613   the preferential removal of the isotopically lighter molecules from the carbon pool during

614   methanogenesis results in a progressive shift in the residual substrate towards heavier, ^{13}C-enriched

615   values (Whiticar, 1999) and fractionation factors decreased with increasing temperature during

616   subduction.

617   In marine sediments, a distinct diagenetic zonation for CH_4 is observed: a sulphate reduction

618   (methane consumption) zone in the uppermost meters, followed by a CH_4 oxidation zone, and a CH_4

619   formation/production zone at the bottom (Claypool & Kaplan, 1974; Whiticar *et al.*, 1986). Usually

620   anaerobic oxidation of methane (Boetius *et al.*, 2000) at the base of the sulphate zone is responsible

621   for active, albeit incomplete, CH_4 removal. For complete sulphate reduction, the CH_4 influx from

622   deeper levels must have been higher than the consumption rates. Analogous to methanogenesis, the

623   bacterial uptake of CH_4 is associated with a kinetic isotope effect that enriches the residual CH_4 in the

624   heavier isotope. A similar diagenetic zonation is a possible scenario that might explain the [13]C

625   variances in upper and lower parts of the Rosetta Marble sections studied here.

626   Cold seep carbonates are generally typified by low $\delta^{13}C$ values since they inherit the strong

627   ^{13}C-depletion relative to the methane gas (Peckmann & Thiel, 2004). However, $\delta^{13}C$ values > +5‰

628   have been also reported for individual carbonates from ancient seep deposits (Gaillard *et al.*, 1992;

629   Peckmann *et al.*, 1999, 2002, 2003; Natalicchio *et al.*, 2012); these values likely result from the

630   formation of ^{13}C-enriched carbonate minerals in the zone of methanogenesis (Peckmann & Thiel,

631   2004). With regard to the ^{13}C-enriched values of the Rosetta marble meta-selenites, a carbon source

632   from methanogenesis should not be excluded *a priori*.

633   With reference to gas hydrates, Pierre *et al.* (2002) report on chemostratigraphic patterns

634   from Late Miocene deposits that might be comparable with those found in the case of the Fesleğen

635   and Karaböğürtlen sections. The carbon isotopes show a distinct shift to ^{13}C-enriched values in the

636   lower part (up to 9.25‰), whereas the $\delta^{18}O$ values display the opposite trend. Generally, these

637   concepts might explain the patterns and absolute values of meta-carbonates measured in the

638   context of this section. Care must be taken, however, as these rocks have suffered significantly more

639   pervasive overprint during burial and metamorphosis compared to the case examples documented in

640   Pierre *et al.* (2002). Carbonates that precipitate during gas hydrate formation are ^{13}C-enriched,

641   whereas decomposition of gas hydrates lead to low $\delta^{13}C$ values in carbonates. Gas hydrates are

642   therefore a possible source for the heavy carbon in the selenite-to-aragonite reaction of the Rosetta

643   Marble. It must be emphasized that tangible evidence for the presence of former gas hydrates in

644   these sections is lacking. This does not rule out, however, that deeper seated gas hydrates released

645   ^{13}C-enriched carbon into the system subsequently to be built into the meta-selenites under study.

646   Concluding, these carbon isotope data seem to support a seawater- and rock-dominated

647 geochemical system resulting in meta-selenites that preserved a seawater- and rock-dominated

648 geochemical system resulting in meta-selenites that preserved their depositional isotope signature.

649 The problem lies with the transition from gypsum to aragonite during subduction that is usually

650 related to strongly ^{13}C-depleted CH_4. Hence, even when mineralogy-driven (aragonite) fractionation

651 is taken into account (Waite & Swart, 2015), one or several sources of ^{13}C-enriched carbon should be

652 considered. Given the limited outcrop conditions and the generally dispersed and incomplete rock

653 record of these metamorphic units, all of these considerations must at present remain on the level of

654 working hypotheses. Potentially, component-specific carbon isotope analysis has the potential to

655 shed light on these complex processes. This, however, must be the topic of further research.

656

657 *Bulk oxygen isotope data*

658 Mean bulk $\delta^{18}O_{meta-selenite}$ isotope ratios (-1.6‰) fall within the boundaries of well-preserved marine

659 carbonate materials of middle Cretaceous age. Generally, evaporation of seawater leads to ^{18}O

660 enriched values (up to +6‰), but depleted $\delta^{18}O$ values in evaporite mineral fluid inclusions have

661 been reported too (mixing with meteoric fluids; Knauth & Beeunas, 1986). Concentration of a

662 hypersaline brine show a shift in the $\delta^{18}O$ values of about +4.0‰ (Longinelli, 1979). Crystallization of

663 gypsum further shifts the $\delta^{18}O$ to +5.5‰ (Longinelli, 1979). Dehydration of gypsum at temperatures

664 of >50°C during transformation to anhydrite could be potentially significant during the subduction of

665 the evaporite-chert successions, but no evidences of anhydrite morphologies could be found.

666 Isotopically, water in the crystal lattice of gypsum is enriched in ^{18}O by about 4‰ relative to the

667 water from which it precipitates (Knauth & Beeunas, 1986). The exceptional preservation of the

668 morphological attributes of the meta-selenite crystals is considered convincing evidence for that

669 direct transformation of gypsum to aragonite without an anhydrite stage. In the case of the

670 successions discussed here, the fluid is predominantly seawater engulfed in the subduction zone and

671 pore-fluid contained within the rock units. The question is, however, to which degree the aquifer

672 fluid and its geochemical properties are isolated from the small volumes of diagenetic fluid at the site

673 of micro-scale dissolution-precipitation processes (Pingitore, 1982) that govern the gypsum to

674 anhydrite neomorphism?

675 Regarding temperature, the sulphate-to-carbonate-reaction is exothermic, i.e., bacterial

676 sulphate reduction yields energy of F°25°C = -40.6 kcal per mole of reacting sulphate (Decker *et al.*,

677 1970). The produced energy increased the bulk rock and fluid temperature and might thus induce a

678 fractionation towards ^{18}O-depleted values (Pierre & Rouchy, 1988). Elevated temperatures might

679 induce the energy required to neomorphose gypsum to aragonite rather than calcite during sulphate

680 reduction reaction even outside of the thermodynamic stable field of aragonite. Volume-for-volume

681 mineral replacement of sulphate (74.31 cm^3/mole) by aragonite (34.16 cm^3/mole) must have taken

682 place under partly open system conditions as otherwise the generation of secondary porosity, *in situ*

683 brecciation and collapse phenomena must be expected (Berner, 1971; Pierre & Rouchy, 1988). This

684 is, with very rare exception not the case in the section studied here.

685 Circumstantial evidence for the oxygen isotope signature of the rocks discussed here comes

686 from Carrara marbles that has seen deep burial and metamorphic overprint and temperatures of

687 200-350°C. Carrara marbles bulk oxygen isotope value plot in the field of 'normal' marine values

688 (Ferry *et al.*, 2002; Ritter *et al.*, 2015). The most likely interpretation is that of low porosity rock units

689 with fluid-to-solid ratios being essentially that of a rock buffered system (Ritter *et al.*, 2015; Pingitore,

690 1982; Berger *et al.*, 2016). Temperature-dependent oxygen isotope fractionation decays as 1/T-

691 squared rather than 1/T at increasingly higher temperatures and approaches nil at around 300°C.

692 Hence, expecting very depleted oxygen isotope values is not in concert with the fundamentals of

693 thermodynamics. Moreover, at these *P–T* conditions, diagenetic fluids are an admixture of CO_2 and

694 H_2O and aqueous diffusion is a dominant factor. All of these factors represent a warning that

695 conventional models applied to evaporite and carbonate diagenesis cannot be used here.

696

697 *^{87}Sr/^{86}Sr isotope ratios and Sr elemental concentrations*

698 Calcite pseudomorphs after gypsum preserve the initial Sr elemental concentration as well as the

699 initial ^{87}Sr/^{86}Sr isotope ratios (e.g. Palaeozoic anhydrite pseudomorphs from Belgium up to 2500

700 ppm; Dejonghe *et al.*, 1998). More radiogenic ^{87}Sr/^{86}Sr ratios may be caused by two reasons: (i)

701 significant *in situ* ^{87}Rb decay following pseudomorphism; or (ii) addition of radiogenic Sr (continental

702 runoff) (Dejonghe *et al.*, 1998). The Sr elemental abundances are consistent with Cretaceous sea

703 water values. Similarly to what was above argued for other geochemical properties, this is best

704 explained by a rock-dominated system. Averaged ^{87}Sr/^{86}Sr (bulk) ratios obtained from samples in the

705 Fesleğen section agree with Late Cretaceous sea water values (McArthur *et al.*, 2001). The potentially

706 stratigraphically older Akçakaya section yields averaged ^{87}Sr/^{86}Sr values, that are in better agreement

707 with Mid-Late Cretaceous seawater ratios. The averaged ^{87}Sr/^{86}Sr ratio of Karaböğürtlen is

708 intermediate in nature and invariant throughout the section.

709 Summing up, it is tempting to observe that reconstructed regional stratigraphic ages agree

710 with relative ages based on ^{87}Sr/^{86}Sr ratios and the McArthur *et al.* (2001) look-up table. Given that

711 these are metamorphic rock that have seen subduction and uplift accompanied with mineralogical

712 change from gypsum to aragonite and finally calcite, skepticism remains. Moreover, semi-restricted

713   basins, that might have been the site of gypsum precipitation as studied here, may deviate in their

714   seawater $^{87}Sr/^{86}Sr$ signature from the global ocean system (e.g. Roveri *et al.*, 2016). In the Messinian

715   marginal basins, for instance, the progressive isolation from the Atlantic Ocean led to a progressive

716   stepwise decrease in $^{87}Sr/^{86}Sr$ ratios, while the global ocean values remained constant (e.g. *Roveri et*

717   *al.*, 2016). Essentially, two end-member solutions for the Cretaceous Rosetta Marble deposits offer

718   themselves: (i) either these rocks— despite very significant mineralogical alteration—preserved their

719   near-pristine $^{87}Sr/^{86}Sr$ ratios to the present day in a closed system behavior; or (ii) a poorly

720   understood diagenetic and metamorphic pathway resulted in diagenetic $^{87}Sr/^{86}Sr$ ratios that, due to

721   the admixture of more or less radiogenic Sr sources, by coincidence, mimic Cretaceous seawater

722   values. At present, the first interpretation seems more reasonable but implies processes that are not

723   well investigated.

724

725   Arguments for a Mid-Late Cretaceous salinity crisis in the Middle Tethys and comparison with

726   Aptian evaporites in the Proto-Atlantic

727   Data shown here are considered evidence for the existence of what are now lost (subducted) basins

728   in the middle Tethys experiencing a salinity crisis perhaps during the Albian. The wide occurrence (ca.

729   600 km in extension) of these meta-selenites all along the Ören-Afyon zone plead for an over

730   regional, basin-wide event that affected significant portions of a middle Tethyan branch. The

731   stratigraphic thickness of the Rosetta Marble unit extends 1500-2000 meters, an observation that

732   points towards a long-lasting salinity crisis. The studied meta-selenites were deposited in a hemi-

733   pelagic sequence, established by abundant tests of radiolarians in the most distal part and turbiditic

734   intervals in the relatively proximal part of the basin. According to paleo-geographic reconstructions

735   (Dercourt *et al.*, 2000) the Tethyan basin was not entirely closed (rather bordered by continents and

736   sills). Warm climatic conditions are reported for the Aptian-Albian times including a gradual warming

737   into the Cenomanian (Frakes, 1999; Clarke & Jenkyns, 1999; Huber *et al.*, 1995; Pucéat *et al.*, 2003,

738   2007). In the upper Aptian, marginal salt deposits of 1 to 2 km stratigraphic thickness precipitated

739   during the earliest opening stages of the Atlantic (Burkes, 1975; Chaboureau *et al.*, 2012) and may,

740   time wise, correlate with Anatolias selenite-pseudomorph units reported here. The Atlantic evaporite

741   units are interpreted with intermittent spillovers into sub-sea-level grabens over a period of 1 to 5

742   Myr (Burke, 1975; Davison, 1999). Spillovers from different oceans over structural sills produced

743   massive evaporite units including horizontal and vertical cycles at least for the evaporites south of

744   the Equator. For the northern Aptian Atlantic evaporites, a hydrothermal origin is proposed by some

745   authors (Hardie, 1990; Chaboureau *et al.*, 2012). For the southern Atlantic salt, a desiccation model

746   (Torsvic *et al.*, 2009; Chaboureau *et al.*, 2012) as well as deep water brines are proposed (Burke,

747   1975). Among these, the Atlantic evaporites are perhaps best comparable to the Rosetta Marble

748   meta-selenite case example and therefore, contribute to very significant seawater evaporation that

749   has a bearing on global-ocean element mass balances of carbon and sulphur (Wortman &

750   Chernyavsky, 2007).

751

Conclusions

753   This paper reports on Cretaceous metamorphosed selenite pseudomorphs from western Anatolia

754   (causally termed 'Rosetta Marble') that stand out by their exceptionally well preserved

755   morphological features and 'marine' geochemical signatures. The extraordinary preservation of

756   delicate textures, typical for selenite, suggests a thermochemical rather than biological sulphate

757   reduction.

758   These rocks have seen high-pressure/low-temperature, i.e. subduction-related metamorphism and

759   peak $P–T$ conditions are estimated as 1.0–1.2 GPa and 300–400°C. Depending on the locality studied,

760   meta-selenites alternate with meta-radiolarites. In terms of their lateral extension (600 km) and

761   stratigraphic thickness (1.5-2 km), the rock-forming meta-selenite deposits of Anatolia provide

762   evidence for a lost Mid to Late Cretaceous salinity crisis in the middle Tethys and must be considered

763   in global ocean element mass balance calculations for this time interval. The Rosetta Marble of

764   Anatolia is, to the knowledge of the authors, the best preserved and largest (in lateral dimension,

765   thickness, and rock-forming character) rock body formed predominantly of selenite pseudomorphs

766   known to science so far.

767   Carbon and oxygen isotopic values of bulk selenite pseudomorphs fall in the range of

768   reconstructed Cretaceous sea water values. Carbon and oxygen isotope values show systematic

769   variances in meta-selenites and host matrix, indicating a phase-depended timing of mineral

770   replacement. The Sr concentration of the calcitized meta-selenites is in agreement with pristine

771   gypsum values and $^{86}Sr/^{87}Sr$ ratios that can be correlated to Cretaceous seawater values. These

772   observations are contrasted by the meta-selenites complex diagenetic and metamorphic pathways

773   (gypsum to aragonite to calcite) and perhaps best understood in the context of a fluid-lean, i.e. rock-

774   dominated system controlled by aqueous diffusion and thin CO_2-H_2O fluid films at crystal boundaries

775   that are essentially isolated from the bulk subduction aquifer.

776   Along a reconstructed proximal-to-distal transect, the most distal (hemi-pelagic) association

777   of meta-selenite-radiolarite couplets has, to the knowledge of the authors, no analogue in Recent or

778   Cenozoic marine basins. An alternation of a radiolarian bloom stage, caused by upwelling of basinal

779   waters and an evaporite deposition stage induced by density cascading brines that formed during

780   arid conditions in the coastal area is proposed. The formation of massive gypsum deposit in a hemi-

781   pelagic environment may provide support to the deep-water–deep-basin model suggested for the

782   deposition of the Mediterranean evaporites during the Messinian Salinity Crisis.

783   From a conceptual point of view, it is suggested that metaselenites are perhaps

784   underexplored archives in palaeoenvironmental research and merit considerably more attention.

785

786   **Acknowledgements**

791
792

793   **References**

794

795   **Aquilano, D., Otálora, F., Pastero, L.,** and **García-Ruiz, J. M.** (2016). Three study cases of growth

796   morphology in minerals: Halite, calcite and gypsum. *Prog. Cryst. Growth Charact. Mater.*, **62**, 227–

797   251.

798   **Ayllon-Quevedo, F., Souza-Egipsy, V., Sanz-Montero, M. E.,** and **Rodríguez-Aranda, J. P.** (2007).

799   Fluid inclusion analysis of twinned selenite gypsum beds from the Miocene of the Madrid basin

800   (Spain). Implication on dolomite bioformation. *Sedim. Geol.,* **201**, 212–230.

801   **Bąbel, M.** (1987) Giant gypsum intergrowths from the Middle Miocene evaporates of southern

802   Poland. *Acta Geol. Pol.*, **37**, 1–20.

803   **Bąbel, M.** (2005) Event stratigraphy of the Badenian selenite evaporites (Middle Miocene) of the

804   northern Carpathian Foredeep. *Acta Geol. Pol.*, **55**, 9–29.

805   **Bąbel, M.** (2007) Depositional environments of a salina-type evaporite basin recorded in the

806   Badenian gypsum facies in the northern Carpathian Foredeep. *Geological Society, London, Special

807   Publications*, **285**, 107–142.

808   **Berger, A., Ebert, A., Ramseyer, K., Gnos, E.** and **Decrouez, D.** (2016) Dolomite microstructures

809   between 390° and 700°C: Indications for deformation mechanisms and grain size evolution. *J. Struct.

810   Geol.*, **89**, 144–152.

811   **Berner, R.A.** (1971) Principles of chemical sedimentology.

812   **Bernoulli, D., de Graciansky, P.C.** and **Monod, O.** (1974) The extension of the Lycian Nappes (SW

813   Turkey) into the southeastern Aegean Islands. *Eclogae Geol. Helv*, **67**, 39–90.

814   **Boetius, A., Ravenschlag, K., Schubert, C.J., Rickert, D., Widdel, F., Gieseke, A., Amann, R.,

815   Jørgensen, B.B., Witte, U.** and **Pfannkuche, O.** (2000) A marine microbial consortium apparently

816   mediating anaerobic oxidation of methane. *Nature*, **407**, 623–626.

817   **Botz, R., Wehner, H., Schmitt, M., Worthington, T.J., Schmidt, M.** and **Stoffers, P.** (2002)
818   Thermogenic hydrocarbons from the offshore Calypso hydrothermal field, Bay of Plenty, New
819   Zealand. *Chem. Geol.*, **186**, 235–248.

820   **Brinkmann, R.** (1967) Die Südflanke des Menderes-Massivs bei Milas, Bodrum und Ören, Sci. Rep.
821   Fac. Sci., Ege Univ., Izmir, Turkey.

822   **Brunn, J.H., de Graciansky, P.C., Gutnic, M., Juteau, T., Lefevre, R., Marcoux, J., Monod, O.** and
823   **Poisson, A.** (1970) Structures majeures et corrélations stratigraphiques dans les Taurides
824   occidentales. *Bulletin de la Societe geologique de France*, **7**, 515–556.

825   **Buick, R.** and **Dunlop, J.S.R.** (1990) Evaporitic sediments of early Archaean age from the Warrawoona
826   Group, North Pole, Western Australia. *Sedimentology*, **37**, 247–277.

827   **Burke, K.** (1975) Atlantic evaporites formed by evaporation of water spilled from Pacific, Tethyan,
828   and Southern oceans. *Geology*, **3**, 613–616.

829   **Candan, O., Çetinkaplan, M., Oberhänsli, R., Rimmelé, G.** and **Akal, C.** (2005) Alpine high-P/low-T
830   metamorphism of the Afyon Zone and implications for the metamorphic evolution of Western
831   Anatolia, Turkey. *Lithos*, **84**, 102–124.

832   **Celâl, A.M.** and **Yilmaz, Y.** (1981) Tethyan evolution of Turkey: a plate tectonic approach.
833   *Tectonophysics*, **75**, 181-241.

834   **Chaboureau, A.C., Donnadieu, Y., Sepulchre, P., Robin, C., Guillocheau, F.** and **Rohais, S.** (2012) The
835   Aptian evaporites of the South Atlantic: a climatic paradox? *Climate of the Past*, **8**, 1047–1058.

836   **Christ, N., Immenhauser, A., Amour, F., Mutti, M., Tomas, S., Agar, S. M., Alway, R.** and **Kabiri, L.**
837   (2012). Characterization and interpretation of discontinuity surfaces in a Jurassic ramp setting (High
838   Atlas, Morocco). *Sedimentology*, **59**, 249–290.

839   **Clari, P., Cavagna, S., Martire, L.** and **Hunziker, J.** (2004) A Miocene mud volcano and its plumbing
840   system: a Chaotic complex revisited. *J. Sed. Res.*, **74**, 662–676.

841   **Clari, P., Pierre, F.D., Martire, L.** and **Cavagna, S.** (2009) The Cenozoic CH_4-derived carbonates of
842   Monferrato (NW Italy): a solid evidence of fluid circulation in the sedimentary column. *Marine*
843   *Geology*, **265**, 167–184.

844   **Clarke, L.J.** and **Jenkyns, H.C.** (1999) New oxygen isotope evidence for long-term Cretaceous climatic
845   change in the Southern Hemisphere. *Geology*, **27**, 699–702.

846   **Claypool, G.E.** and **Kaplan, I.R.** (1974) The origin and distribution of methane in marine sediments. In
847   *Natural gases in marine sediments*, pp. 99–139, Springer, Boston, MA.

848   **Cody, R.D.** and **Cody, A.M.** (1988) Gypsum nucleation and crystal morphology in analog saline
849   terrestrial environments. *J. Sed. Res.*, **58**.

850   **Cohen, K.M., Finney, S.C., Gibbard, P.L.** and **Fan, J.X.** (2013) The ICS international
851   chronostratigraphic chart. *Episodes,* **36**, 199–204

852   **Collins AS** and **Robertson AH** (1997) Lycian melange, southwestern Turkey: an emplaced Late
853   Cretaceous accretionary complex. *Geology*, **25**, 255–258.

854   **Davison, I.** (1999) Tectonics and hydrocarbon distribution along the Brazilian South Atlantic margin.
855   *Geol. Soc., London, Special Publications*, **153**, 133–151.

856   **Debenedetti, A.** (1982). The problem of the origin of the salt deposits in the Mediterranean and of
857   their relations to the other salt occurrences in the Neogene formations of the contiguous regions.
858   *Marine Geology*, **49**, 91–114.

859   **Decker, K., Jungermann, K.** and **Thauer, R.K.** (1970) Energy production in anaerobic organisms.
860   *Angewandte Chemie International Edition*, **9**, 138–158.

861   **Deer, W.A., Howie, R.A.** and **Zussman, J.** (1992) An introduction to the rock-forming minerals (Vol.
862   696). Hong Kong: Longman Scientific & Technical.

863 **De Graciansky, P.** (1972). Recherches géologiques dans le Taurus lycien occidental (Turquie du SW)
864 (Doctoral dissertation, Thèse Univ. Paris-Sud (Orly), 896, 1–762.

865 **Dejonghe, L., Demaiffe, D.** and **Weis, D.** (1998) Strontium isotope geochemistry of anhydrites and
866 calcite pseudomorphs after anhydrite from Palaeozoic formations in Belgium. Chemical geology, **144**,
867 63–71.

868 **Dela Pierre, F., Bernardi, E., Cavagna, S., Clari, P., Gennari, R., Irace, A., Lozar, F., Lugli, S., Manzi, V.,**
869 **Natalicchio, M., Roveri, M. and Violanti, D.** (2011) The record of the Messinian salinity crisis in the
870 Tertiary Piedmont Basin (NW Italy): the Alba section revisited. *Palaeogeogr. Palaeoclimatol.*
871 *Palaeoecol.*, **310**, 238-255.

872 **De Lange, G.J.** and **Krijgsman, W.** (2010) Messinian salinity crisis: a novel unifying shallow
873 gypsum/deep dolomite formation mechanism. *Mar. Geol.*, **275**, 273–277.

874 **Della Porta, G.** (2015) Carbonate build-ups in lacustrine, hydrothermal and fluvial settings:
875 comparing depositional geometry, fabric types and geochemical signature. *Geol. Soc., London,*
876 *Special Publications*, **418**, 17–68.

877 **Dercourt, J., Gaettani, M., Vrielynck, B., Barrier, E., Biju-Duval, B.** and **Brunet, M.F.** (2000). Atlas
878 peri-Tethys, paleogeographical maps, Commission for the Geologic Map of the World
879 (CCGM/CGMW, 24 maps and explanatory notes).

880 **Des Marais, D.J.** and **Moore, J.G.** (1984) Carbon and its isotopes in mid-oceanic basaltic glasses. *Earth*
881 *and Planetary Science Letters*, **69**, 43–57.

882 **Fernández-Díaz, L., Pina, C.M., Astilleros, J.M.** and **Sánchez-Pastor, N.** (2009) The carbonatation of
883 gypsum: Pathways and pseudomorph formation. *Am. Mineral.*, **94**, 1223–1234.

884 **Ferry, J.M., Wing, B.A., Penniston-Dorland, S.C.** and **Riumble, D.I.** (2002) The direction of fluid flow
885 during contact metamorphism of siliceous carbonate rocks: new data for the Monzoni and Redazzo
886 aureoles, northern Italy, and a global review. *Contrib. Mineral Petrol*, **142**, 679–699.

887 **Fleitmann, D., Matter, A., Pint, J.J.** and **Al-Shanti, M.A.** (2004) The speleothem record of climate
888 change in Saudi Arabia. *Saudi Geological Survey, Jeddah, Kingdom of Saudi Arabia*.

889 **Frakes, L.A.** (1999) Estimating the global thermal state from Cretaceous sea surface and continental
890 temperature data. *Geol. Soc. America Spec. Publ.*, 49–58.

891 **Gaillard, C., Rio, M., Rolin, Y.** and **Roux, M.** (1992) Fossil chemosynthetic communities related to
892 vents or seeps in sedimentary basins: the pseudobioherms of southeastern France compared to
893 other world examples. *Palaios*, 451–465.

894 **García-Veigas, J., Cendón, D.I., Gibert, L., Lowenstein, T.K.,** and **Artiaga, D.** (2018). Geochemical
895 indicators in Western Mediterranean Messinian evaporites: Implications for the salinity crisis. *Mar.*
896 *Geol.*, **403**, 197–214.

897 **Geske, A., Zorlu, J., Richter, D.K., Buhl, D., Niedermayr, A.** and **Immenhauser, A.** (2012) Impact of
898 diagenesis and low grade metamorphosis on isotope (δ 26 Mg, δ 13 C, δ 18 O and 87 Sr/86 Sr) and
899 elemental (Ca, Mg, Mn, Fe and Sr) signatures of Triassic sabkha dolomites. *Chem. Geol.*, **332**, 45–64.

900 **Gillet, P.** and **Goffé, B.** (1988) On the significance of aragonite occurrences in the Western Alps.
901 *Contrib. Mineral. Petrol.*, **99**, 70–81.

902 **Göncüoğlu, M.C.** (2011) Geology of the Kütahya–Bolkardağ Belt. *Bulletin of The Mineral Research and*
903 *Exploration*, **142**, 223–277.

904 **Göncüoğlu, M.C., Özcan, A., Turhan, N.** and **Işık, A.** (1992) Stratigraphy of Kütahya region, ISGB-92
905 *Field Guide Book, MTA, Ankara*, pp 3–11.

906 **Greinert, J., Bohrmann, G.** and **Suess, E.** (2001) Gas hydrate-associated carbonates and methane-
907 venting at Hydrate Ridge: classification, distribution, and origin of authigenic lithologies. Natural gas
908 hydrates: Occurrence, distribution, and detection, 99–113.

909 **Gutnic, M., Monod, O., Poisson, A.** and **Dumont, J.F.** (1979) Géologie des Taurides occidentales
910 (Turquie), *Mém. Soc. Géol. France*, **137**, 1–112.

911 **Güngör, T.** and **Erdoğan, B.** (2001) Emplacement age and direction of the Lycian nappes in the Söke-
912 Selçuk region, western Turkey. *Int. J. Earth Sci.*, **89**, 874–882.

913 **Hardie, L.A.** (1990) The roles of rifting and hydrothermal CaCl₂ brines in the origin of potash
914 evaporites; an hypothesis. *Am. J. Sci.*, **290**, 43–106.

915 **Hohenegger, J., Ćorić, S.** and **Wagreich, M.** (2014) Timing of the middle miocene Badenian stage of
916 the central Paratethys. *Geol. Carpath.*, **65**, 55–66.

917 **Huber, B.T., Hodell, D.A.** and **Hamilton, C.P.** (1995) Middle–Late Cretaceous climate of the southern
918 high latitudes: stable isotopic evidence for minimal equator-to-pole thermal gradients. *Geol. Soc. Am.*
919 *Bull.*, **107**, 1164–1191.

920 **Hsü, K.J., Ryan, W.B.F.** and **Cita, M.B.** (1973) Late Miocene desiccation of the Mediterranean.
921 *Nature*, **242**, 240–244.

922 **Immenhauser, A., Holmden, C.** and **Patterson, W.P.** (2008) Interpreting the carbon-isotope record of
923 ancient shallow epeiric seas: lessons from the recent. *Dynamics of epeiric seas*, **48**, 135–174.

924 **Immenhauser, A., Schöne, B.R., Hoffmann, R.** and **Niedermayr, A.** (2016) Mollusc and brachiopod
925 skeletal hard parts: Intricate archives of their marine environment. *Sedimentology*, **63**, 1–59.

926 **Katz, A., Sass, E., Starinsky, A.** and **Holland, H.D.** (1972) Strontium behavior in the aragonite-calcite
927 transformation: An experimental study at 40–98 C. *Geochim. Cosmochim. Acta*, **36**, 481–496.

928 **Knauth, L.P.** and **Beeunas, M.A.** (1986) Isotope geochemistry of fluid inclusions in Permian halite
929 with implications for the isotopic history of ocean water and the origin of saline formation waters.
930 *Geochim. Cosmochim. Acta*, **50**, 419–433.

931 **Longinelli, A.** (1979) Isotope geochemistry of some Messinian evaporates: paleoenvironmental
932 implications. *Palaeogeogr. Palaeoclimatol. Palaeoecol.*, **29**, 95–123.

933 **Lugli, S., Manzi, V., Roveri, M.** and **Schreiber, B.C.** (2010) The Primary Lower Gypsum in the
934 Mediterranean: a new facies interpretation for the first stage of the Messinian salinity crisis.
935 *Palaeogeogr. Palaeoclimatol. Palaeoecol.*, **297**, 83–99.

936 **Lu, F.H., Meyers, W.J.** and **Schoonen, M.A.** (2001) S and O (SO4) isotopes, simultaneous modeling,
937 and environmental significance of the Nijar Messinian gypsum, Spain. *Geochim. Cosmochim. Acta*, **65**,
938 3081–3092.

939 **Lu, F.H., Meyers, W.J.** and **Hanson, G.N.** (2002) Trace elements and environmental significance of
940 Messinian gypsum deposits, the Nijar Basin, southeastern Spain. *Chem. Geol.*, **192**, 149–161.

941 **Machel, H.G.** (2001) Bacterial and thermochemical sulfate reduction in diagenetic settings—old and
942 new insights. *Sed. Geol.*, **140**, 143–175.

943 **Mattey, D.P., Carr, R.H., Wright, I.P.** and **Pillinger, C.T.** (1984) Carbon isotopes in submarine basalts.
944 *Earth Planet. Sci. Lett.*, **70**, 196–206.

945 **McArthur, J.M., Howarth, R.J.** and **Bailey, T.R.** (2001) Strontium isotope stratigraphy: LOWESS
946 version 3: best fit to the marine Sr-isotope curve for 0–509 Ma and accompanying look-up table for
947 deriving numerical age. *The Journal of Geology*, **109**, 155–170.

948 **McBride, E.F., Honda, H., Abdel-Wahab, A.A., Dworkin, S.** and **McGilvery, T.A.** (1992) Fabric and
949 origin of gypsum sand crystals, Laguna Madre, Texas.

950 **Miall, A.D.** (2013) Principles of sedimentary basin analysis. Springer Science & Business Media.

951 **Natalicchio, M., Birgel, D., Dela Pierre, F., Martire, L., Clari, P.A., Spötl, C.** and **Peckmann, J.** (2012)
952 Polyphasic carbonate precipitation in the shallow subsurface: insights from microbially-formed
953 authigenic carbonate beds in upper Miocene sediments of the Tertiary Piedmont Basin (NW Italy).
954 *Palaeogeogr. Palaeoclimatol. Palaeoecol.*, **329**, 158–172.

955 **Natalicchio, M., Pierre, F.D., Lugli, S., Lowenstein, T.K., Feiner, S.J., Ferrando, S., Manzi, V., Roveri,**
956 **M.** and **Clari, P.** (2014). Did Late Miocene (Messinian) gypsum precipitate from evaporated marine
957 brines? Insights from the Piedmont Basin (Italy). *Geology*, **42**, 179–182.

958 **Nigrini, C.** and **Caulet, J.P.** (1992) Late Neogene radiolarian assemblages characteristic of Indo-Pacific
959 areas of upwelling. *Micropaleontology*, 139–164.

960 **Oberhänsli, R., Partzsch, J., Candan, O.** and **Cetinkaplan, M.** (2001) First occurrence of Fe-Mg-
961 carpholite documenting a high-pressure metamorphism in metasediments of the Lycian Nappes, SW
962 Turkey. *Int. J. Earth Sci.*, **89**, 867–873.

963 **Oberhänsli, R., Candan, O., Bousquet, R., Rimmelé, G., Okay, A.** and **Goff, J.** (2010) Alpine high
964 pressure evolution of the eastern Bitlis complex, SE Turkey. *Geol. Soc. London Spec. Publ.*, **340**, 461–
965 483.

966 **Okay, A., Satir, M., Maluski, H., Siyako, M., Monie, P., Metzger, R.** and **Akyüz, S.** (1996) Paleo-and
967 Neo-Tethyan events in northwestern Turkey: Geologic and geochronologic constraints. *World Reg.*,
968 420–441.

969 **Oppo, D., Capozzi, R.** and **Picotti, V.** (2013) A new model of the petroleum system in the Northern
970 Apennines, Italy. *Mar. Petrol. Geol.*, **48**, 57–76.

971 **Ortí, F.** (2011) Selenite facies in marine evaporites: A review. Quaternary carbonate and evaporite
972 sedimentary facies and their ancient analogues: A Tribute to Douglas James Shearman, 431–463.

973 **Ortí, F., Pueyo, J.J., Geisler, D.** and **Dulau, N.** (1984) Evaporitic sedimentation in the coastal
974 salinas of Santa Pola (Alicante, Spain): Diputación Provincial de Barcelona, Instituto de
975 Investigaciones Geológicas, Revista, **38–39**, 169–220.

976 **Özcan, A., Göncüoğlu, M.C., Turhan, N., Uysal, Ş., Şentürk, K.** and **Işik, A.** (1988) Late Paleozoic
977 evolution of the Kütahya-Bolkardağ belt. *METU J. Pure Appl. Sci.*, **21**, 211–220

978 **Özcan, A., Turhan, N.** and **Göncüöğlu, M.C.** (1989) Kütahya-Çifteler-Bayat- İ˙hsanye yöresinin Temel
979 Jeologisi: Maden Tetkik ve Arama Genel Müdürlüğü Report no: 8974(8188), 142 s, Ankara
980 (unpublished).

981 **Özer S, Sözbilir H, Özkar İ, Toker V** and **Sari B** (2001) Stratigraphy of Upper Cretaceous-Palaeogene
982 sequences in the southern and eastern Menderes Massif (western Turkey). *Int. J. Earth Sci.*, **89**, 852–
983 866.

984 **Özkaya, İ.** (1990) Origin of the allochthons in the Lycien Belt, Southwest Turkey. *Tectonophysics*, **177**,
985 367–379.

986 **Peckmann, J.,Thiel, V., Michaelis, W., Clari, P., Gaillard, C., Martire, L.** and **Reitner, J.** (1999) Cold
987 seep deposits of Beauvoisin (Oxfordian; southeastern France) and Marmorito (Miocene; northern
988 Italy): microbially induced authigenic carbonates. *Int. J. Earth Sci.*, **88**, 60–75.

989 **Peckmann, J., Goedert, J.L., Thiel, V., Michaelis, W.** and **Reitner, J.** (2002) A comprehensive
990 approach to the study of methane-seep deposits from the Lincoln Creek Formation, western
991 Washington State, USA. *Sedimentology*, **49**, 855–873.

992 **Peckmann, J., Goedert, J.L., Heinrichs, T., Hoefs, J.** and **Reitner, J.** (2003) The Late Eocene'Whiskey
993 Creek'methane-seep deposit (western Washington State). *Facies*, **48**, 241.

994 **Peckmann, J.** and **Thiel, V.** (2004) Carbon cycling at ancient methane–seeps. *Chem. Geol.*, **205**, 443–
995 467.

996 **Pierre, C.** and **Rouchy, J.M.** (1988) Carbonate replacements after sulfate evaporites in the middle
997 Miocene of Egypt. *J. Sed. Res.*, **58**.

998 **Pierre, C., Rouchy, J.M.** and **Blanc-Valleron, M.M.** (2002) Gas hydrate dissociation in the Lorca Basin
999 (SE Spain) during the Mediterranean Messinian salinity crisis. *Sed. Geol.*, **147**, 247–252.

1000   **Pineau, F.** and **Javoy, M.** (1983) Carbon isotopes and concentrations in mid-oceanic ridge basalts.
1001   *Earth Planet. Sci. Lett.*, **62**, 239–257.

1002   **Pingitore, Jr N.E.** (1976) Vadose and phreatic diagenesis: processes, products and their recognition in
1003   corals. *J. Sed. Res.*, **46**.

1004   **Pingitore, Jr N.E.** (1982) The role of diffusion during carbonate diagenesis. *J. Sed. Res.*, **52**.

1005   **Poisson, A.** (1977) Recherches géologiques dans les Taurides occidentales (Turquie). Universite de
1006   Paris-Sud (Centre D'orsay).

1007   **Pourteau, A., Candan, O.** and **Oberhänsli, R.** (2010) High-pressure metasediments in central Turkey:
1008   constraints on the Neotethyan closure history. *Tectonics*, **29**.

1009   **Pourteau, A., Sudo, M., Candan, O., Lanari, P., Vidal, O.** and **Oberhänsli, R.** (2013) Neotethys closure
1010   history of Anatolia: insights from 40Ar–39Ar geochronology and P–T estimation in high-pressure
1011   metasedimentary rocks. *J. Metamorph. Geol.*, **31**, 585–606.

1012   **Pourteau, A., Bousquet, R., Vidal, O., Plunder, A., Duesterhoeft, E., Candan, O.** and **Oberhänsli, R.**
1013   (2014) Multistage growth of Fe–Mg–carpholite and Fe–Mg–chloritoid, from field evidence to
1014   thermodynamic modelling. *Contrib. Mineral. Petrol.*, **168**, 1–25.

1015   **Pourteau, A., Oberhänsli, R., Candan, O., Barrier, E.** and **Vrielynck, B.** (2016) Neotethyan closure
1016   history of western Anatolia: a geodynamic discussion. *Int. J. Earth Sci.*, **105**, 203–224.

1017   **Pucéat, E., Lécuyer, C., Sheppard, S.M., Dromart, G., Reboulet, S.** and **Grandjean, P.** (2003) Thermal
1018   evolution of Cretaceous Tethyan marine waters inferred from oxygen isotope composition of fish
1019   tooth enamels. *Paleoceanography*, **18**.

1020   **Pucéat, E., Lécuyer, C., Donnadieu, Y., Naveau, P., Cappetta, H., Ramstein, G., Huber, B.T.** and
1021   **Kriwet, J.** (2007) Fish tooth δ18O revising Late Cretaceous meridional upper ocean water
1022   temperature gradients. *Geology*, **35**, 107–110.

1023   **Rimmelé, G., Jolivet, L., Oberhänsli, R.** and **Goffé, B.** (2003) Deformation history of the high-pressure
1024   Lycian Nappes and implications for tectonic evolution of SW Turkey. *Tectonics*, **22**.

1025   **Rimmelé, G., Parra, T., Goffé, B., Oberhänsli, R., Jolivet, L.** and **Candan, O.** (2005) Exhumation paths
1026   of high-pressure–low-temperature metamorphic rocks from the Lycian Nappes and the Menderes
1027   Massif (SW Turkey): a multi-equilibrium approach. *J. Petrol.*, **46**, 641–669.

1028   **Rimmelé, G., Oberhänsli, R., Candan, O., Goffé, B.** and **Jolivet, L.** (2006) The wide distribution of HP-
1029   LT rocks in the Lycian Belt (Western Turkey): implications for accretionary wedge geometry. *Geol.
1030   Soc. London Spec. Publ.*, **260**, 447–466.

1031   **Ritter, A.C., Kluge, T., Berndt, J., Richter, D.K., John, C.M., Bodin, S.** and **Immenhauser, A.** (2015)
1032   Application of redox sensitive proxies and carbonate clumped isotopes to Mesozoic and Palaeozoic
1033   radiaxial fibrous calcite cements. *Chem. Geol.*, **417**, 306–321.

1034   **Roberts, H.H.** and **Aharon, P.** (1994) Hydrocarbon-derived carbonate buildups of the northern Gulf of
1035   Mexico continental slope: a review of submersible investigations. *Geo-Marine Lett.*, **14**, 135–148.

1036   **Robertson, A.H.** and **Ustaömer, T.** (2009) Upper Palaeozoic subduction/accretion processes in the
1037   closure of Palaeotethys: evidence from the Chios Melange (E Greece), the Karaburun Melange (W
1038   Turkey) and the Teke Dere Unit (SW Turkey). *Sed. Geol.*, **220**, 29–59.

1039   **Rosell, L., Ortí, F., Kasprzyk, A., Playa, E.** and **Peryt, T.M.** (1998) Strontium geochemistry of Miocene
1040   primary gypsum: Messinian of southeastern Spain and Sicily and Badenian of Poland. *J. Sed. Res.*, **68**.

1041   **Rouchy, J.M., Taberner, C., Blanc-Valleron, M-M., Sprovieri, R., Russell, M., Pierre, C., Di Stefano,
1042   E., Pueyo, J.J., Caruso, A., Dinarès-Turell, J., Gomis-Coll, E., Wolff, G.A., Cespuglio, G., Ditchfield, P.,
1043   Pestrea, S., Combourieu-Nebout, N., Santisteban, C.** and **Grimalt, J.O.** (1998) Sedimentary and
1044   diagenetic markers of the restriction in a marine basin: the Lorca Basin (SE Spain) during the
1045   Messinian. *Sed. Geol.*, **121**, 23–55.

1046 **Roveri, M., Manzi, V., Bergamasco, A., Falcieri, F.M., Gennari, R., Lugli, S.** and **Schreiber, B.C.** (2014)
1047 Dense shelf water cascading and Messinian canyons: a new scenario for the Mediterranean salinity
1048 crisis. *Am. J. Sci.*, **314**, 751–784.
1049 **Roveri, M., Gennari, R., Lugli, S., Manzi, V., Minelli, N., Reghizzi, M., Riva, A., Rossi, M.E.** and
1050 **Sackett, W.M.** (1978) Carbon and hydrogen isotope effects during the thermocatalytic production of
1051 hydrocarbons in laboratory simulation experiments. *Geochim. Cosmochim. Acta.*, **42**, 571–580.
1052 **Scheffler, F., Oberhänsli, R., Pourteau, A., Candan, O.** and **Di Lucia, M.** (2014) The Rosetta Marbles
1053 from Fesleğen, Ören Unit, SW Anatolia. *Int. J. Earth Sci.*, **103**, 485.
1054 **Scheffler, F., Oberhänsli, R., Pourteau, A., Immenhauser, A.** and **Candan, O.** (2016) Sedimentologic
1055 to metamorphic processes recorded in the high-pressure/low-temperature Mesozoic Rosetta Marble
1056 of Anatolia. *Int. J. Earth Sci.*, **105**, 225–246.
1057 **Schmalz, R.F.** (1969) Deep-water evaporite deposition: a genetic model. *AAPG Bulletin*, **53**, 798–823.
1058 **Schneider, J., Bakker, R.J., Bechstädt, T.** and **Littke, R.** (2008) Fluid evolution during burial diagenesis
1059 and subsequent orogenetic uplift: The La Vid Group (Cantabrian zone, northern Spain). *J. Sed. Res.*,
1060 **78**, 282–300.
1061 **Staplin, F.L.** (1969) Sedimentary organic matter, organic metamorphism, and oil and gas occurrence.
1062 *Bull. Can. Petrol. Geol.*, **17**, 47–66.
1063 **Swart, P.K.** (2015) The geochemistry of carbonate diagenesis: The past, present and future.
1064 *Sedimentology*, **62**, 1233–1304.
1065 **Swennen, R., Viaene, W.** and **Cornelissen, C.** (1990) Petrography and geochemistry of the Belle
1066 Roche breccia (lower Visean, Belgium): evidence for brecciation by evaporite dissolution.
1067 *Sedimentology*, **37**, 859–878.
1068 **Şengör, A.M.C.** (1990) Plate-tectonics and orogenic research after 25 years—a tethyan perspective.
1069 *Earth Sci, Rev.*, **27**, 1–201.
1070 **Tassi, F., Bonini, M., Montegrossi, G., Capecchiacci, F., Capaccioni, B.** and **Vaselli, O.** (2012) Origin of
1071 light hydrocarbons in gases from mud volcanoes and CH 4-rich emissions. *Chem. Geol.*, **294**, 113–126.
1072 **van Hinsbergen, D.J., Dekkers, M.J., Bozkurt, E.** and **Koopman, M.** (2010) Exhumation with a twist:
1073 Paleomagnetic constraints on the evolution of the Menderes metamorphic core complex, western
1074 Turkey. *Tectonics*, **29**.
1075 **Veizer, J., Bruckschen, P., Pawellek, F., Diener, A., Podlaha, O.G., Carden, G.A., Jasper, T., Korte, C.,**
1076 **Strauss, H.** and **Ala, D.** (1997) Oxygen isotope evolution of Phanerozoic seawater. *Palaeogeogr.*
1077 *Palaeoclimatol. Palaeoecol.*, **132**, 159–172.
1078 **Veizer, J., Ala, D., Azmy, K., Bruckschen, P., Buhl, D., Bruhn, F., Carden, G.A.F., Diener, A., Ebneth,**
1079 **S., Godderis, Y.** and **Jasper, T.** (1999) 87Sr/86Sr, δ13C and δ18O evolution of Phanerozoic seawater.
1080 *Chem. Geol.*, **161**, 59–88.
1081 **Waite, A.J.** and **Swart, P.K.** (2015) The inversion of aragonite to calcite during the sampling of
1082 skeletal archives: Implications for proxy interpretation. *Rapid Communications in Mass Spectrometry*,
1083 **29**, 955–964.
1084 **Warren, J.K., Havholm, K.G., Rosen, M.R.** and **Parsley, M.J.** (1990) Evolution of gypsum karst in the
1085 Kirschberg Evaporite Member near Fredericksburg, Texas. *J. Sed. Res.*, **60**.
1086 **Warren, J.K.** (1999) Evaporites: their evolution and economics. Wiley-Blackwell.
1087 **Warren, J.K.** (2016) Evaporites: A Geological Compendium. Springer.
1088 **Whiticar, M.J., Faber, E.** and **Schoell, M.** (1986). Biogenic methane formation in marine and
1089 freshwater environments: CO2 reduction vs. acetate fermentation—isotope evidence. *Geochim.*
1090 *Cosmochim. Acta*, **50**, 693–709.

1091   **Whiticar, M.J.** (1999) Carbon and hydrogen isotope systematics of bacterial formation and oxidation

1092   of methane. *Chem. Geol.*, **161**, 291–314.

1093   **Zachos, J., Pagani, M., Sloan, L., Thomas, E.** and **Billups, K**. (2001) Trends, rhythms, and aberrations

1094   in global climate 65 Ma to present. *Science*, **292**, 686-693.

1095

1096

1097

1
2
3 1098 **FIGURE CAPTIONS**
4 1099
5
6 1100 **Fig. 1.** Tectonic map of Turkey in an UTM36N coordinate system (based on Okay 2008, Pourteau *et*
7 1101 *al.*, 2010, Oberhänsli *et al.*, 2010, Çetinkaplan *et al.*, 2014, Scheffler *et al.*, 2016). Green stars
8 1102 represent Cretaceous Rosetta Marble localities, which are restricted to the Ören–Afyon Zone. The
9
10 1103 study area is outlined by a whitish box.
11
12 1104 **Fig. 2.** Simplified pressure-temperature (*P–T)* diagram (after Scheffler et al., 2016) showing the three-
13 1105 stage evolution of the Rosetta Marble formation during subduction and exhumation. Conditions for
14 1106 thermochemical sulphate reduction (TSR) are located in the aragonite and gypsum stability field. A
15 1107 combination of high-Si phengite-quartz-water thermobarometric modeling from white mica within
16
17 1108 the Rosetta Marble of Fesleğen (Dubacq *et al.*, 2010; Scheffler *et al.*, 2016), *P–T* calculations of
18 1109 adjacent units based on multi-equilibrium calculationns (Rimmelé *et al.*, 2005) and calculated *P–T*
19 1110 conditions of the western and eastern Afyon Zone (Pourteau *et al.*, 2014) determine the maximum
20
21 1111 *P–T* conditions (high pressure (HP) metamorphism). The retrograde path is initiated by the crossing
22 1112 of the aragonite–calcite transition line (Hacker *et al.*, 2005) at >200°C to account for the overall lack
23 1113 of preserved aragonite. Gypsum–bassanite–anhydrite reaction curves are from Yamamoto &
24 1114 Kennedy (1969). See supplementary Fig. B for background data.
25
26 1115 **Fig. 3.** Three different facies types according to increasing distal position in the paleo-basin: (A) Type–
27 1116 locality Fesleğen. Selenite pseudomorph–containing marble, referred to as "Rosetta Marble", is
28
29 1117 interbedded with meta-calc-arenitic (quartzite) units and aligned chert nodules. The upper layer
30 1118 boundary of the meta-arenitic beds is marked by an erosive surface. (B) Type–locality Akçakaya.
31 1119 Rosetta Marble thickly alternates with nodular and ribbon bedded chert and form a typical pelagic-
32 1120 appearing sequence in m-scale. (C) Type–locality Karaböğürtlen. Thin-bedded (a few cm's) Rosetta
33
34 1121 Marble layers interbedded with radiolarian-rich chert and meta-wackestone. Scale: field book, 20 cm
35 1122 long; hammer length: 56.5 cm, finger width: 1.7 cm.
36
37 1123 **Fig. 4.** Fesleğen stratigraphic section. The lower part of the section is characterized by layered
38 1124 arenitic intervals with erosive surfaces. Upsection, meta-chert proportion increases. The upper part
39 1125 of the section consists of a regular selenite-pseudomorph bearing marble–chert alternation. On most
40
41 1126 exposed bedding planes dm- to m-wide radial textures can be observed. Perpendicular to the
42 1127 bedding, fan textures are restricted to certain levels.
43
44 1128 **Fig. 5.** Karaböğürtlen section and corresponding isotope data set. (A) Sampled section. The
45 1129 uppermost 11 meters represent the red pelagic part of the section. The lower part of the section is
46 1130 characterized by yellowish thickly bedded selenite-pseudomorph containing marble–chert
47
48 1131 alternations. (B) Detailed stratigraphic section of the uppermost 11 meters showing regular selenite
49 1132 pseudomorph–containing marble–chert couplets. (C) Close up of the uppermost 11 meters of the
50 1133 studied section. (D) Close up of the yellowish part of the outcrop. (E) Chemostratigraphy of isotope
51 1134 data. The uppermost 11 meters clearly differ in their δ^{13}C, δ^{18}O and ^{87}Sr/^{86}Sr isotope values from the
52 1135 lower part of the section. Maximal errors for oxygen-, carbon- and Sr-isotopes are smaller than the
53
54 1136 chosen symbol-size.
55
56 1137 **Fig. 6.** Growth orientations of selenite pseudomorphs. Arrows point to stratigraphic upwards. (A)
57 1138 Dome-shaped fan growing on top of a previous fan. (B) Subparallel to leaning crystals. (C)
58
59
60

1139   Downwards growing crystal fan with nucleation point at the bottom of an overlaying chert layer. (D)
1140   Up- and downward oriented fans with chert nodule as central nucleation point. (E) Radiating rods
1141   radiating from an impurity-rich central surface. Growth is confined by upper and lower chert layers.
1142   (F) Radiating rods initiating from a central point. Hammer length is 56.5 cm. Fesleğen surroundings,
1143   Ören Unit.

1144   **Fig. 7.** Large scale horizontal/in-plane meta-selenite textures at bedding planes. (A) Radial
1145   appearance of selenite-pseudomorph fans. (B) Complex interactions of textures due to space
1146   competitions. Hammer length is 56.5 cm. Fesleğen surroundings, Ören Unit.

1147   **Fig. 8.** Crystal habits and morphotypes of selenite-pseudomorphs. (A) Rod-like crystal habits in grey
1148   marble matrix. Rods consist of fibrous calcites. Note the pushed forward brown material on top of
1149   the rods. (B) Swallowtail stacked crystals. (C) Fishbone-like radiating crystals in a quartzitic matrix. (D)
1150   Christmas-tree shaped selenite pseudomorphs approaching dendritic habits. (E) Skeletal texture
1151   (bunches of sabre-like crystals). (F) Crystal fronts. Hammer length is 56.5 cm, hammer shaft is 3 cm
1152   wide; coin diameter is ~2.6 cm; pen length is 16 cm.

1153   **Fig. 9.** Selenite-pseudomorphs and meta-chert in micro-scale. (A) Elongated crystal habits outlined by
1154   fine grained marl. Fesleğen, transmitted light. (B) Elongated crystal shapes. The marly material here
1155   mainly consists of microcrystalline quartz and dolomite rhombs. Karaböğürtlen (lower section),
1156   crossed polarizers. (C) Elongated crystals that grow from different directions. Free space is filled with
1157   smaller crystals. Karaböğürtlen (upper section), transmitted light. (D) Elongated crystal habits in the
1158   upper part of the picture and pseudo-hexagonal basal sections (c-axis towards viewer) in the central
1159   part. Karaböğürtlen (upper section), transmitted light. (E) Transition between selenite-pseudomorphs
1160   and meta-chert layers is characterized by an accumulation of partly zoned dolomite rhombs of
1161   different sizes. Fesleğen, crossed polarizers. (F) Sharp transition between a selenite-pseudomorph
1162   and a meta-chert layer. Chert layers comprise less dolomites towards the layer centers.
1163   Karaböğürtlen, transmitted light.

1164   **Fig. 10.** (A) Calcite fibres (pseudomorph after aragonite) in a siliceous-carbonaceous matrix. Fesleğen,
1165   crossed polarizers. (B) Calcified radiolarian relics in a meta-wackestone. Karaböğürtlen, transmitted
1166   light. (C) Chert containing silicified radiolarian relics and zoned dolomite rhombs. Karaböğürtlen,
1167   transmitted light. (D) Transition between a meta-wackestone and a chert layer. Both contain equally
1168   sized radiolarian relics. Karaböğürtlen, transmitted light.

1169   **Fig. 11.** Cathodoluminescence images. (A, B) Despite recrystallization zonation of gypsum habits are
1170   preserved. (C, D) Variable growth directions of the meta-selenites. (E) Primary and altered areas are
1171   only distinguishable. (F) Selenite crystal habits replaced by a single calcite crystal (no aragonite fibers
1172   are preserved here). Samples are from Karaböğürtlen.

1173   **Fig. 12.** $\delta^{13}C$–$\delta^{18}O$ cross plot. Sample sites are shape coded, stratigraphic level within sections is color
1174   coded. Almost all samples plot in the 69% confident field of mean mid-Cretaceous sea water. Most of
1175   the samples plot within the mean Cretaceous sea water reconstruction of Veizer (1999). Fesleğen
1176   and Karaböğürtlen sections show clusters according to the stratigraphic position of the samples. Dark
1177   red and light red circles are sampled in the upper part of the Karaböğürtlen section, orange circles in
1178   the lower part. Medium green triangles belong to samples coming from the upper part of the

1179   Fesleğen section, light green triangles to the lower part. Dark green triangles refer to samples taken
1180   close to the Fesleğen section, but not within.

1181   **Fig. 13.** $\delta^{13}C$ data of all three sections (corresponding to different facies) in comparison. The sections
1182   are not temporally comparable to each other. The stratigraphic younger parts of the sections differ in
1183   their $\delta^{13}C$ values significantly. The stratigraphic older parts of the sections approximate each other.
1184   Color coding within sections refers to the stratigraphic position of sampling and is consistent with Fig.
1185   12.

1186   **Fig. 14.** Carbon isotope mapping of a Rosetta Marble rock slab. Note the clustering according to the
1187   sampled material.

1188   **Fig. 15.** Depositional environmental model. (A) Gypsum growth mode. Regular spillovers of cascading
1189   brines serve as ion-supplies to the deeper and more distal parts. Gypsum growth takes place in
1190   restricted ponds and size of selenites correlate to the distance to the shore line. (B)
1191   Turbidite/Radiolarite deposition mode. Humid climate prevents wide evaporation. Upwelling water
1192   masses on shelf area serve for nutrient-rich water surface conditions that promote radiolarian
1193   bloom. Turbidites and radiolarites form at that stage. (C) Simplified stratigraphic sections
1194   corresponding from proximal to distal localities in the paleo basin.

1195   **Fig. 16.** Observed growth geometries are documented and classified in the first column. Based on
1196   that, the primary growing conditions were reconstructed in the second column. (A) Upwards
1197   oriented fans grow at the sea floor (t_0-t_1) and can be restricted by the pycnocline level (t_1). An
1198   alternation of fan-growing layers with Si-rich layers is causing the final appearance of the rock (t_3) (B)
1199   Downward oriented fans grow displacive into the soft substratum (t_0), which can be either Si-rich or
1200   Si-depleted. (C) A combination of A and B conditions is able to produce up- and downward oriented
1201   fans that are spherical in shape. (D) The most common horizontal radial crystals are either explained
1202   by cutting effects (1. Scenario), by restricted growth due to a shallow pycnocline level (2. Scenario),
1203   or, a combination of both scenarios.

1204   **Fig. 17.** Textural comparison of Neogene selenitic gypsum deposits from the Mediterranean and the
1205   Paratethys basins, left column, with Cretaceous selenite pseudomorphs from Anatolia, right column.
1206   (A) Climate-driven alternations of gypsum and shale layers. Messinian, Sicily, Italy. (B) Regular
1207   selenite-pseudomorph-marble – meta-chert couplets. (C) Giant selenite intergrowth. Badenian, near
1208   Kraków, Poland. (D) Selenite pseudomorphs resembling giant intergrowth. (E) Stacked swallow-tail
1209   crystals (columnar symmetrical twins). Messinian, Piedmont, Italy. (F) Gypsum pseudomorphs
1210   resembling swallowtail twins. Hammer shaft width is 3 cm.

1211   **Fig. 18.** Textural comparison of Neogene selenitic gypsum deposits, left column, with Cretaceous
1212   selenite pseudomorphs from Anatolia, right column. (A) Radiating gypsum crystals around tree
1213   trunks. Badenian, near Kraków, Poland. (B) Radiating selenite-pseudomorphs on a bedding plane. (C)
1214   Radiating selenite crystals perpendicular (up- and downward) to the bedding plane. Messinian, Sicily,
1215   Italy. (D) Radiating selenite pseudomorph crystals perpendicular (up- and downward) to the bedding
1216   plane. Picture is tilted, see original in Fig. 5. (E) Layerd gypsum with in-situ brecciation. Badenian,
1217   near Kraków, Poland. (F) Layerd marble (meta-gypsum) with in-situ brecciation.

1218 **Fig. 19.** Textural comparison of Neogene selenitic gypsum deposits with Cretaceous selenite
1219 pseudomorphs from Anatolia. (A) Large sabre-like selenite crystal in a gypsum matrix. Bedenian,
1220 Kraków, Poland. (B) Large sabre-like selenite pseudomorh crystal in a marble matrix. (C) Curved sabre
1221 selenite crystals in a gypsum matrix. Bedenian, Kraków, Poland. (D) Curved sabre-like selenite
1222 psuedomroph crystal in a marble matrix. Note the calcite fibres that are pseudomorphic after
1223 aragonite. (E) Growing surfaces within a twinned selenite crystal. Arrow indicates growing direction.
1224 Messinian, Piedmont, Italy. (F) Growing surfaces of selenite pseudomorph crystals. (G) Re-entrant
1225 angle (dark gray portion) and twinning plane of a swallow-tail selenite crystal. Bedenian, Kraków,
1226 Poland. (H) Dark grey line (arrow) within swallowtail selenite pseudomorph crystals as relict of an
1227 impurity-rich twin plane.

1228

1229 **TABLE HEADINGS**

1230

1231 <u>Table 1</u>
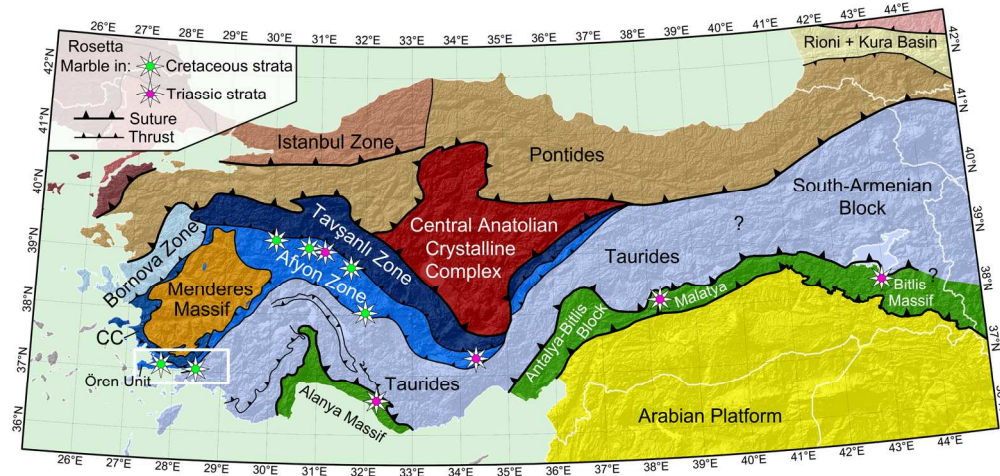
1232 Oxygen and Carbon isotope data. An outlier from Akçakaya was excluded: $\delta^{13}C = -0.64‰$ and $\delta^{18}O =$
1233 $-6.65‰$. An outlier from "All samples Feslegen" was excluded, probably a secondary vein was
1234 sampled: $\delta^{13}C = -0.75‰$ and $\delta^{18}O = -3.01‰$.

1235

1236 <u>Table 2</u>

1237 Strontium isotope data.

1238

Tectonic map of Turkey in an UTM36N coordinate system (based on Okay 2008, Pourteau et al., 2010, Oberhänsli et al., 2010, Çetinkaplan et al., 2014, Scheffler et al., 2016). Green stars represent Cretaceous Rosetta Marble localities, which are restricted to the Ören–Afyon Zone. The study area is outlined by a whitish box.

170x81mm (300 x 300 DPI)
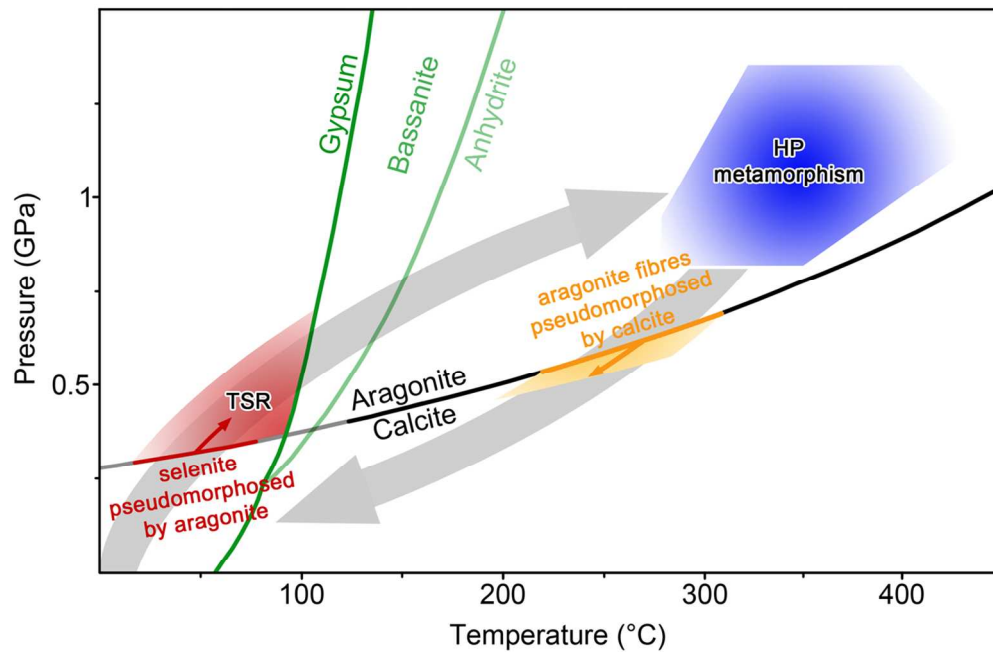
Simplified pressure-temperature (P–T) diagram (after Scheffler et al., 2016) showing the three-stage evolution of the Rosetta Marble formation during subduction and exhumation. Conditions for thermochemical sulphate reduction (TSR) are located in the aragonite and gypsum stability field. A combination of high-Si phengite-quartz-water thermobarometric modeling from white mica within the Rosetta Marble of Fesleğen (Dubacq et al., 2010; Scheffler et al., 2016), P–T calculations of adjacent units based on multi-equilibrium calculationns (Rimmelé et al., 2005) and calculated P–T conditions of the western and eastern Afyon Zone (Pourteau et al., 2014) determine the maximum P–T conditions (high pressure (HP) metamorphism). The retrograde path is initiated by the crossing of the aragonite–calcite transition line (Hacker et al., 2005) at >200°C to account for the overall lack of preserved aragonite. Gypsum–bassanite–anhydrite reaction curves are from Yamamoto & Kennedy (1969). See supplementary Fig. B for background data.

119x78mm (300 x 300 DPI)
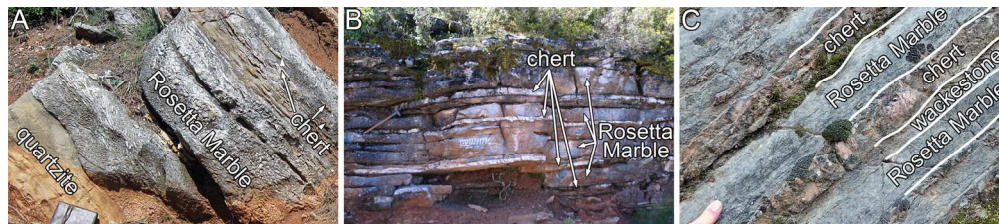
Three different facies types according to increasing distal position in the paleo-basin: (A) Type–locality Fesleğen. Selenite pseudomorph–containing marble, referred to as "Rosetta Marble", is interbedded with meta-calc-arenitic (quartzite) units and aligned chert nodules. The upper layer boundary of the meta-arenitic beds is marked by an erosive surface. (B) Type–locality Akçakaya. Rosetta Marble thickly alternates with nodular and ribbon bedded chert and form a typical pelagic-appearing sequence in m-scale. (C) Type–locality Karaböğürtlen. Thin-bedded (a few cm's) Rosetta Marble layers interbedded with radiolarian-rich chert and meta-wackestone. Scale: field book, 20 cm long; hammer length: 56.5 cm, finger width: 1.7 cm.

170x37mm (300 x 300 DPI)
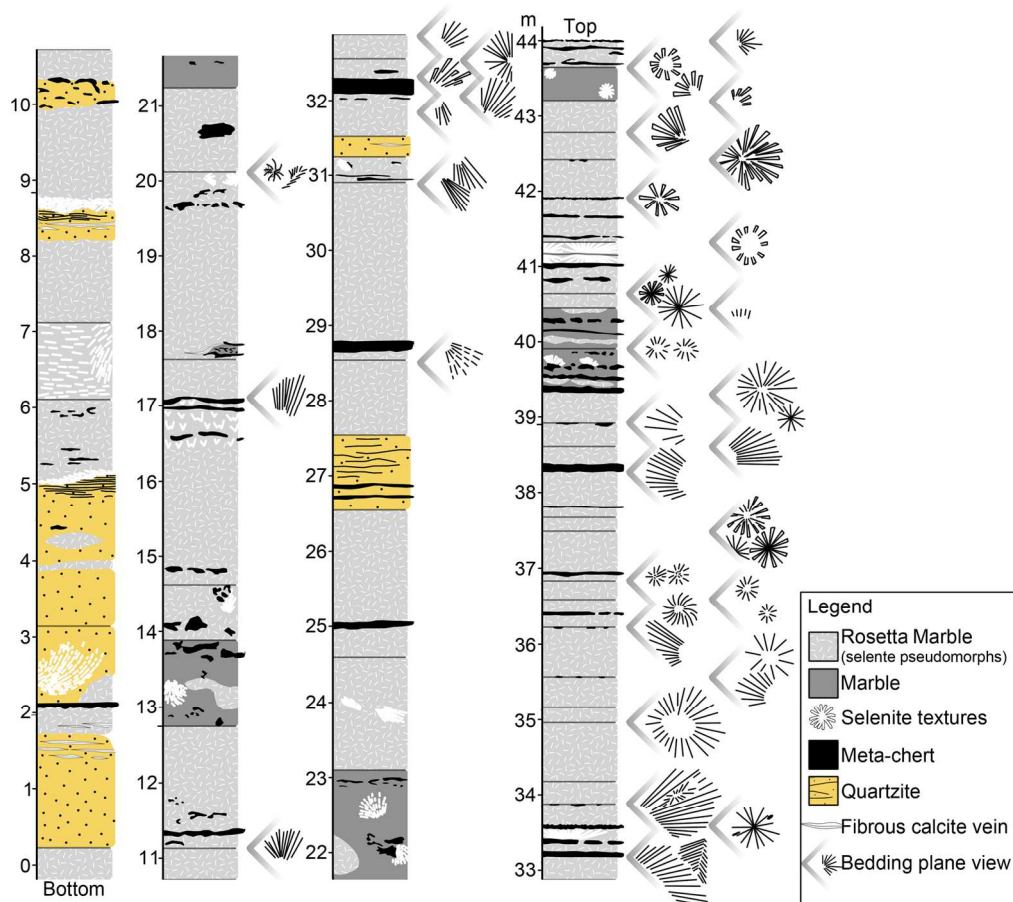
Fesleğen stratigraphic section. The lower part of the section is characterized by layered arenitic intervals with erosive surfaces. Upsection, meta-chert proportion increases. The upper part of the section consists of a regular selenite-pseudomorph bearing marble–chert alternation. On most exposed bedding planes dm- to m-wide radial textures can be observed. Perpendicular to the bedding, fan textures are restricted to certain levels.

170x153mm (300 x 300 DPI)
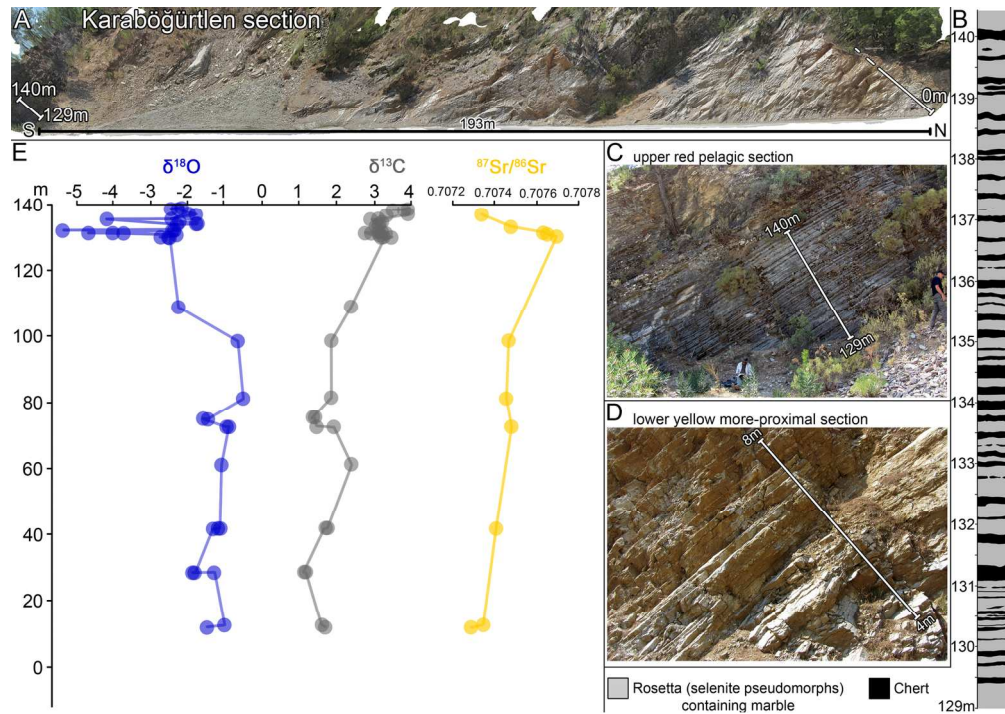
Karaböğürtlen section and corresponding isotope data set. (A) Sampled section. The uppermost 11 meters represent the red pelagic part of the section. The lower part of the section is characterized by yellowish thickly bedded selenite-pseudomorph containing marble–chert alternations. (B) Detailed stratigraphic section of the uppermost 11 meters showing regular selenite pseudomorph–containing marble–chert couplets. (C) Close up of the uppermost 11 meters of the studied section. (D) Close up of the yellowish part of the outcrop. (E) Chemostratigraphy of isotope data. The uppermost 11 meters clearly differ in their δ13C, δ18O and 87Sr/86Sr isotope values from the lower part of the section. Maximal errors for oxygen-, carbon- and Sr-isotopes are smaller than the chosen symbol-size.

170x119mm (300 x 300 DPI)
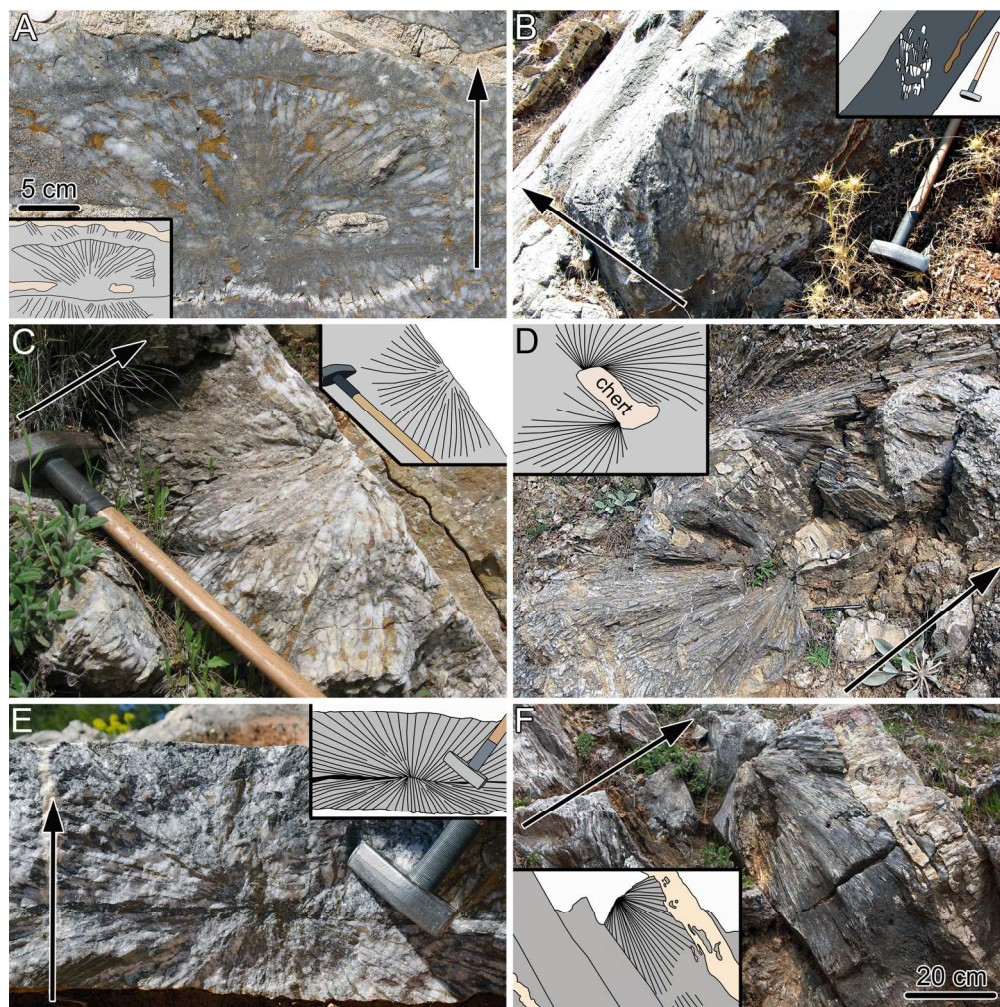
Growth orientations of selenite pseudomorphs. Arrows point to stratigraphic upwards. (A) Dome-shaped fan growing on top of a previous fan. (B) Subparallel to leaning crystals. (C) Downwards growing crystal fan with nucleation point at the bottom of an overlaying chert layer. (D) Up- and downward oriented fans with chert nodule as central nucleation point. (E) Radiating rods radiating from an impurity-rich central surface. Growth is confined by upper and lower chert layers. (F) Radiating rods initiating from a central point. Hammer length is 56.5 cm. Fesleğen surroundings, Ören Unit.

170x169mm (300 x 300 DPI)
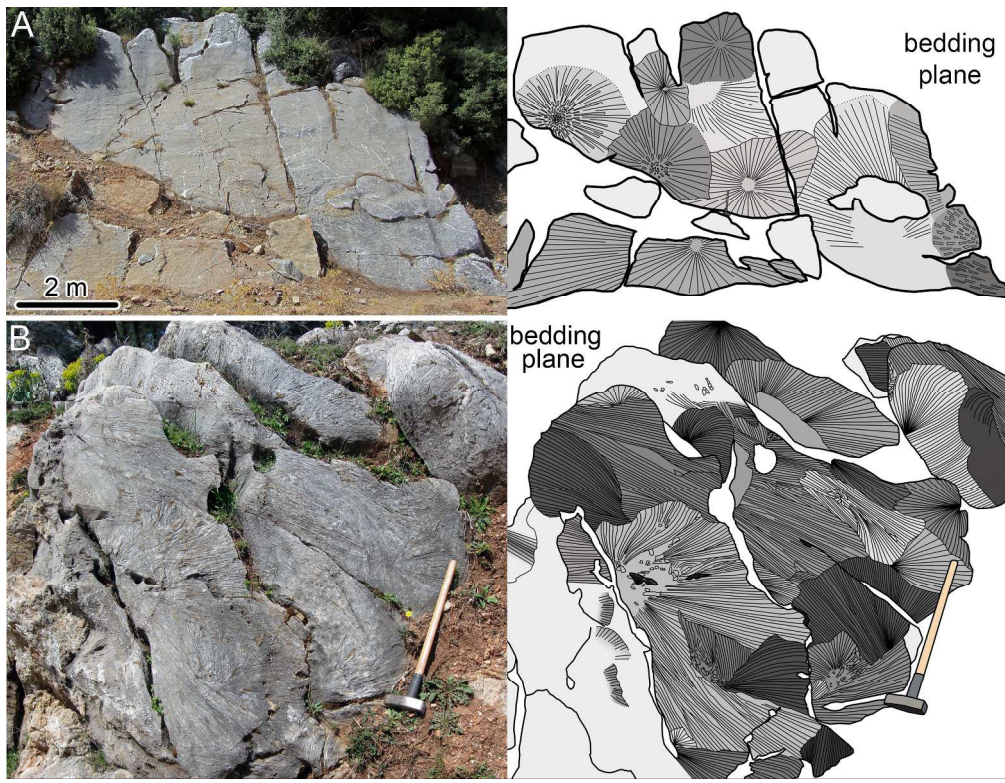
Large scale horizontal/in-plane meta-selenite textures at bedding planes. (A) Radial appearance of selenite-pseudomorph fans. (B) Complex interactions of textures due to space competitions. Hammer length is 56.5 cm. Fesleğen surroundings, Ören Unit.

245x188mm (300 x 300 DPI)

Crystal habits and morphotypes of selenite-pseudomorphs. (A) Rod-like crystal habits in grey marble matrix. Rods consist of fibrous calcites. Note the pushed forward brown material on top of the rods. (B) Swallowtail stacked crystals. (C) Fishbone-like radiating crystals in a quartzitic matrix. (D) Christmas-tree shaped selenite pseudomorphs approaching dendritic habits. (E) Skeletal texture (bunches of sabre-like crystals). (F) Crystal fronts. Hammer length is 56.5 cm, hammer shaft is 3 cm wide; coin diameter is ~2.6 cm; pen length is 16 cm.

170x158mm (300 x 300 DPI)
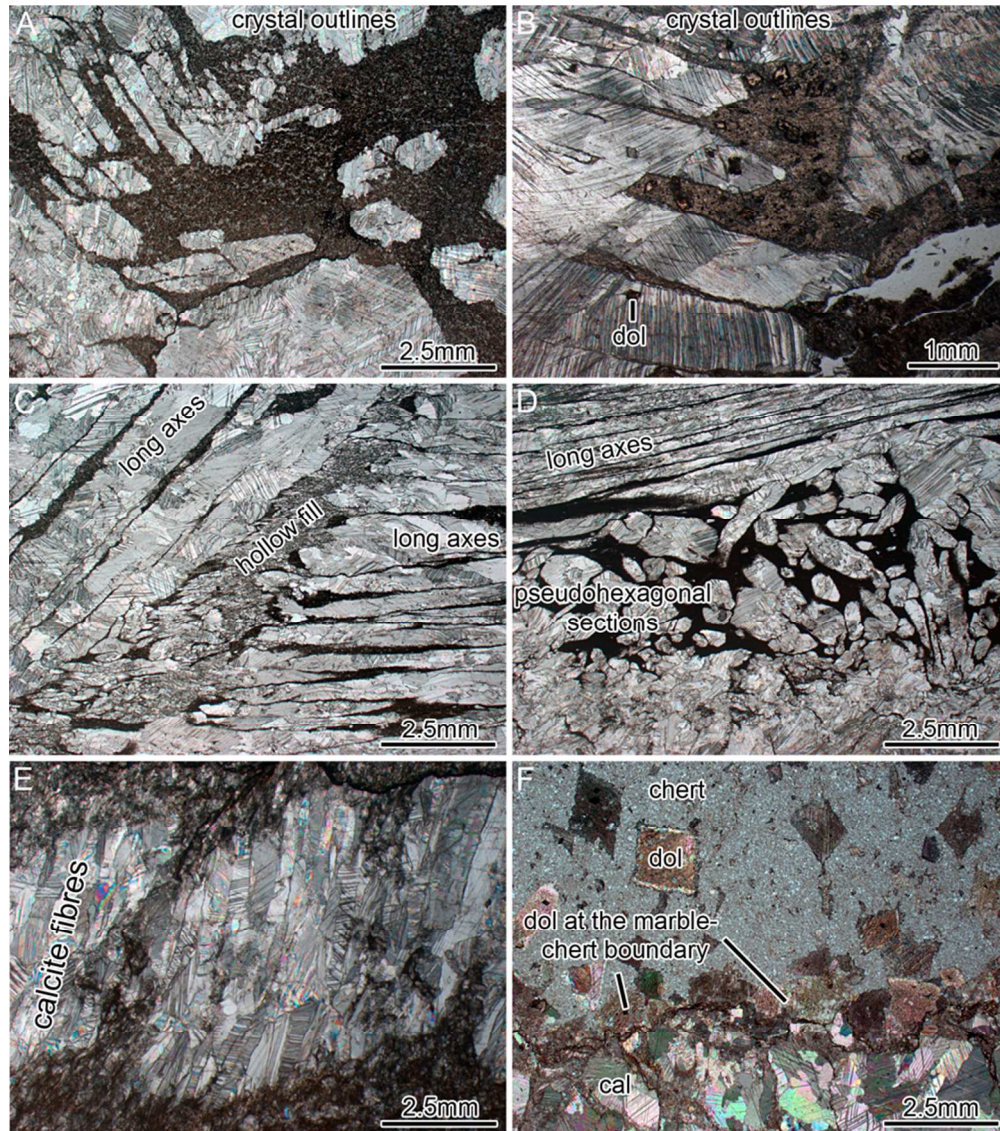
1
2
3
4
5
6
7
8
9
10
11
12
13
14
15
16
17
18
19
20
21
22
23
24
25
26
27
28
29
30
31
32
33
34
35
36
37
38
39
40
41
42
43
44
45
46
47
48
49
50
51
52
53
54
55
56
57
58
59
60

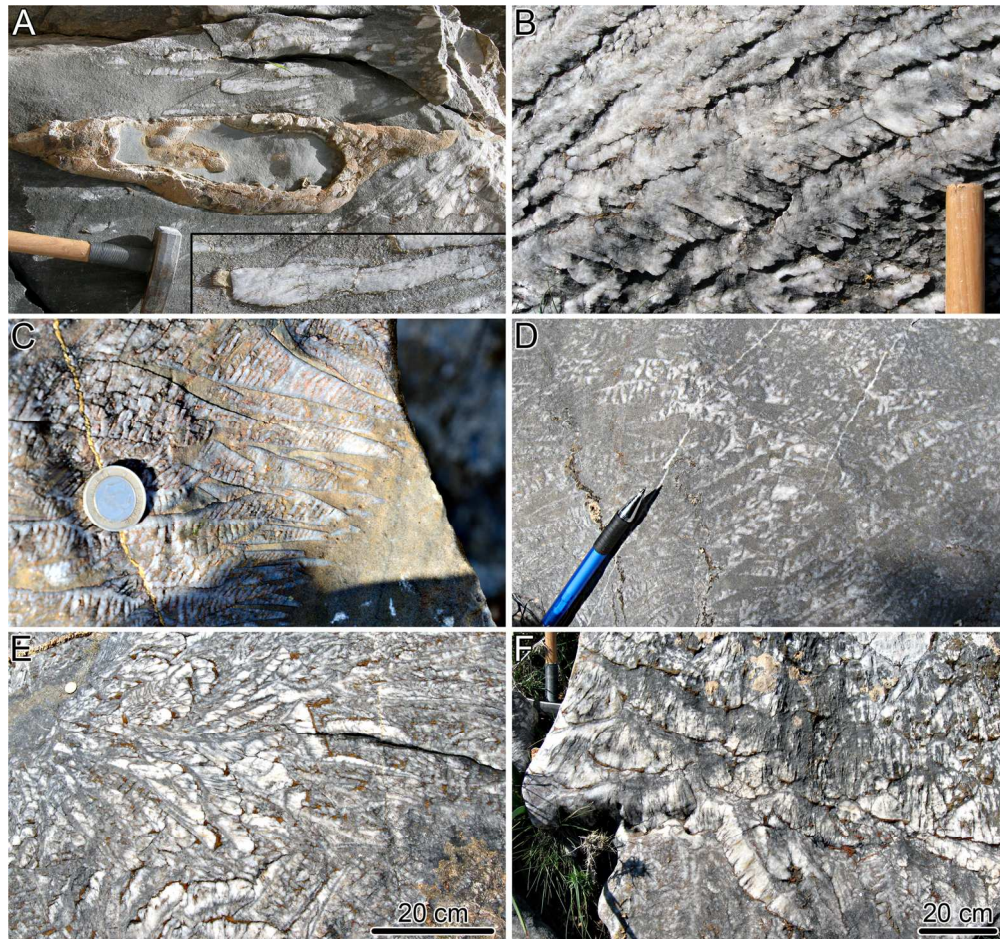Selenite-pseudomorphs and meta-chert in micro-scale. (A) Elongated crystal habits outlined by fine grained marl. Fesleğen, transmitted light. (B) Elongated crystal shapes. The marly material here mainly consists of microcrystalline quartz and dolomite rhombs. Karaböğürtlen (lower section), crossed polarizers. (C) Elongated crystals that grow from different directions. Free space is filled with smaller crystals. Karaböğürtlen (upper section), transmitted light. (D) Elongated crystal habits in the upper part of the picture and pseudo-hexagonal basal sections (c-axis towards viewer) in the central part. Karaböğürtlen (upper section), transmitted light. (E) Transition between selenite-pseudomorphs and meta-chert layers is characterized by an accumulation of partly zoned dolomite rhombs of different sizes. Fesleğen, crossed polarizers. (F) Sharp transition between a selenite-pseudomorph and a meta-chert layer. Chert layers comprise less dolomites towards the layer centers. Karaböğürtlen, transmitted light.

170x191mm (150 x 150 DPI)
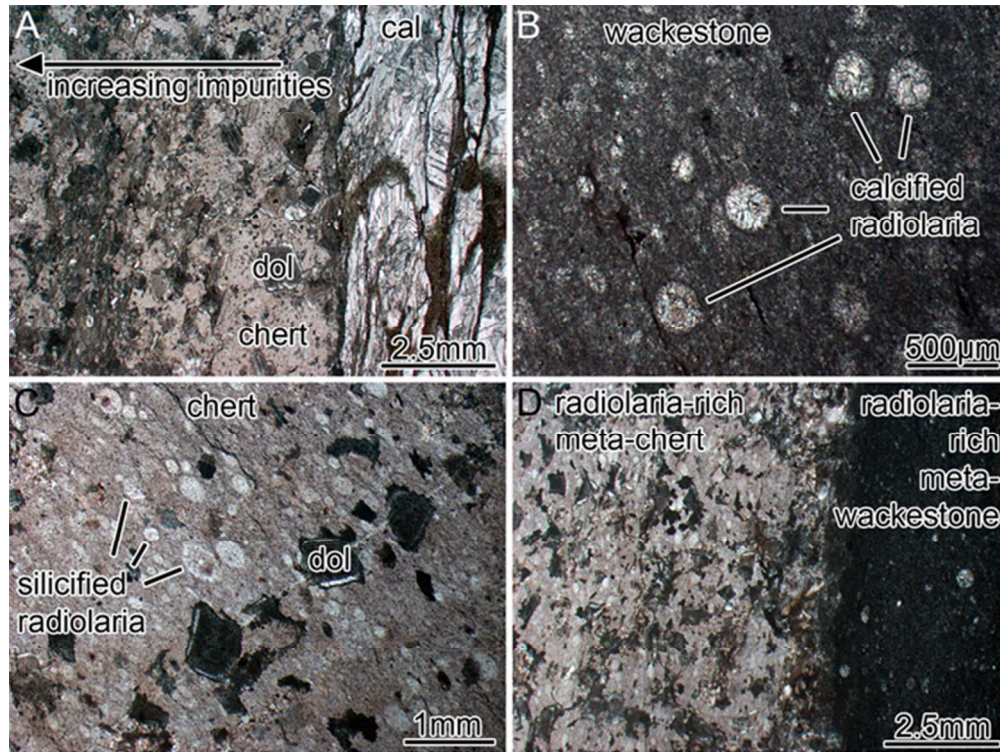
(A) Calcite fibres (pseudomorph after aragonite) in a siliceous-carbonaceous matrix. Fesleğen, crossed polarizers. (B) Calcified radiolarian relics in a meta-wackestone. Karaböğürtlen, transmitted light. (C) Chert containing silicified radiolarian relics and zoned dolomite rhombs. Karaböğürtlen, transmitted light. (D) Transition between a meta-wackestone and a chert layer. Both contain equally sized radiolarian relics. Karaböğürtlen, transmitted light.

120x89mm (150 x 150 DPI)
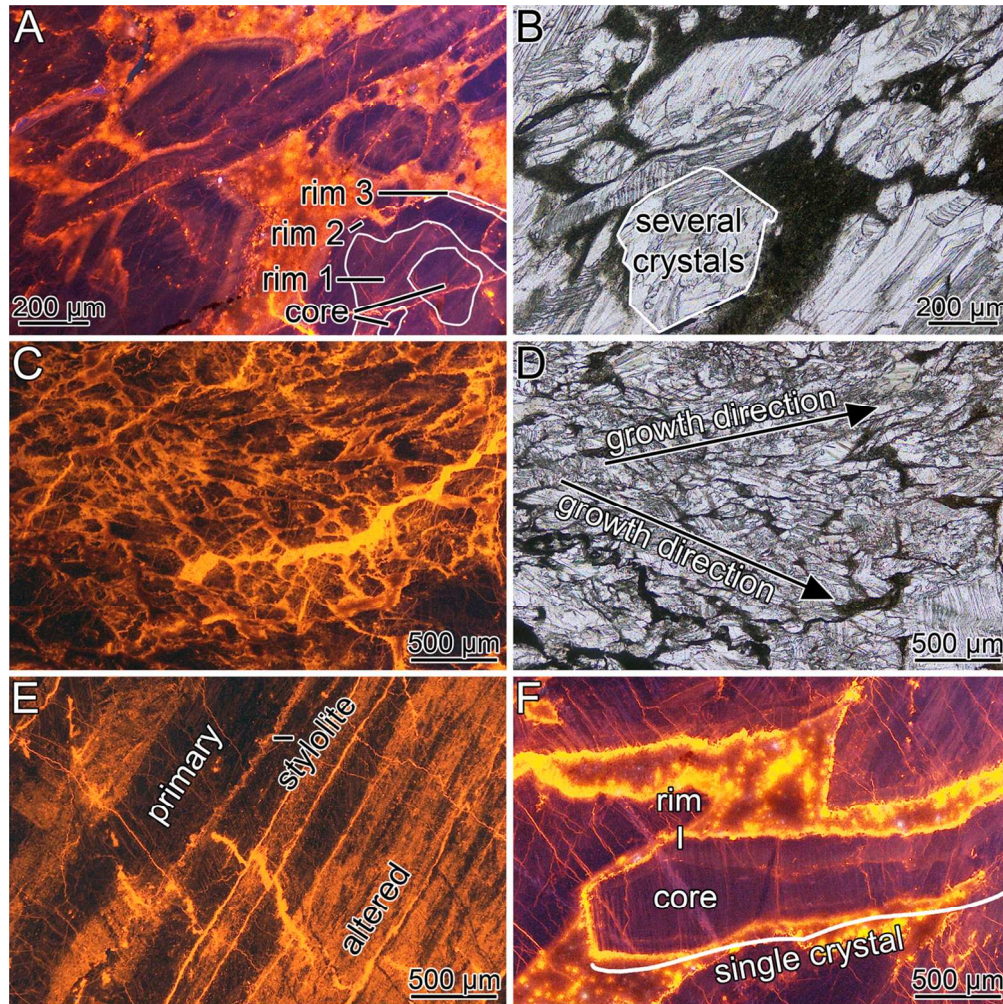
Cathodoluminescence images. (A, B) Despite recrystallization zonation of gypsum habits are preserved. (C, D) Variable growth directions of the meta-selenites. (E) Primary and altered areas are only distinguishable. (F) Selenite crystal habits replaced by a single calcite crystal (no aragonite fibers are preserved here). Samples are from Karaböğürtlen.

119x119mm (300 x 300 DPI)
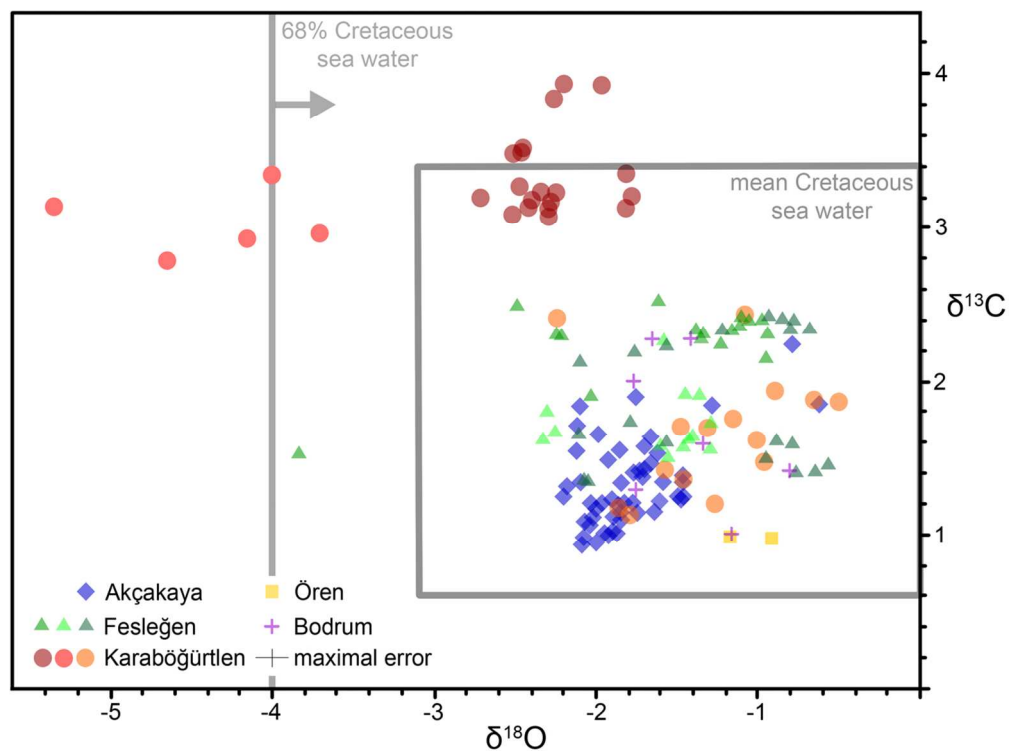
δ13C–δ18O cross plot. Sample sites are shape coded, stratigraphic level within sections is color coded. Almost all samples plot in the 69% confident field of mean mid-Cretaceous sea water. Most of the samples plot within the mean Cretaceous sea water reconstruction of Veizer (1999). Fesleğen and Karaböğürtlen sections show clusters according to the stratigraphic position of the samples. Dark red and light red circles are sampled in the upper part of the Karaböğürtlen section, orange circles in the lower part. Medium green triangles belong to samples coming from the upper part of the Fesleğen section, light green triangles to the lower part. Dark green triangles refer to samples taken close to the Fesleğen section, but not within.

119x89mm (300 x 300 DPI)
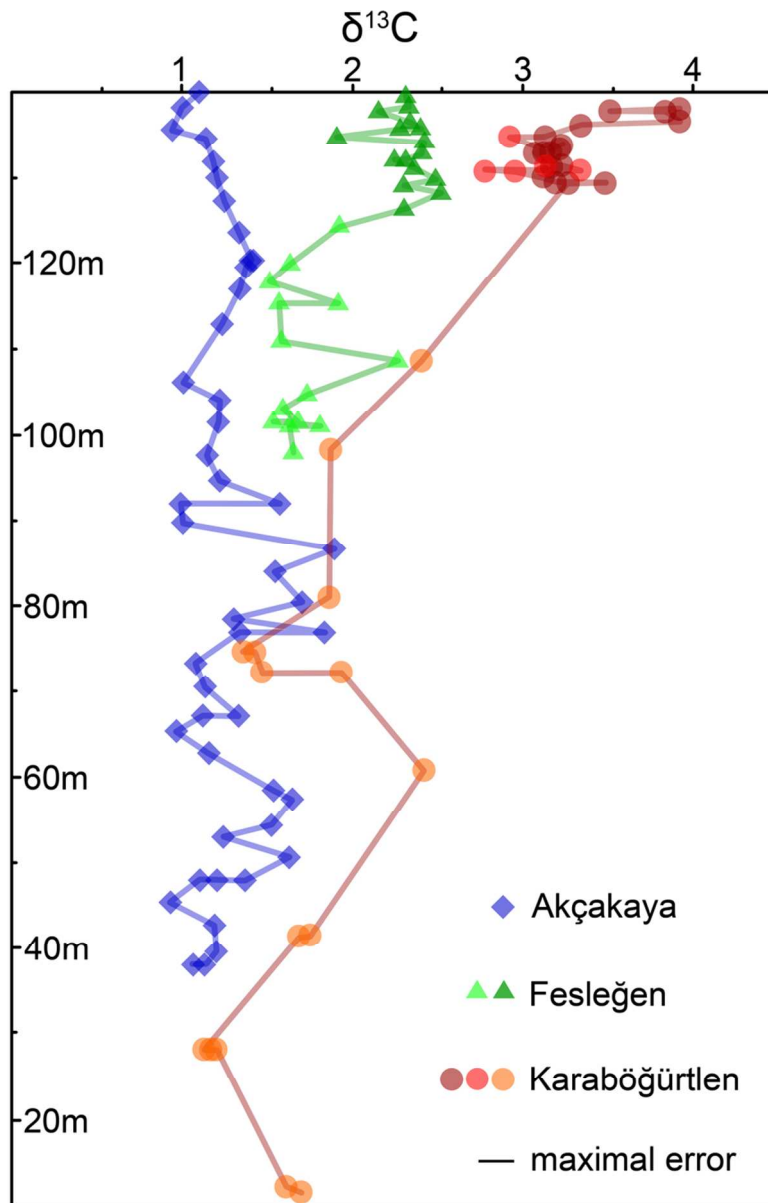
δ13C data of all three sections (corresponding to different facies) in comparison. The sections are not temporally comparable to each other. The stratigraphic younger parts of the sections differ in their δ13C values significantly. The stratigraphic older parts of the sections approximate each other. Color coding within sections refers to the stratigraphic position of sampling and is consistent with Fig. 12.

80x124mm (300 x 300 DPI)
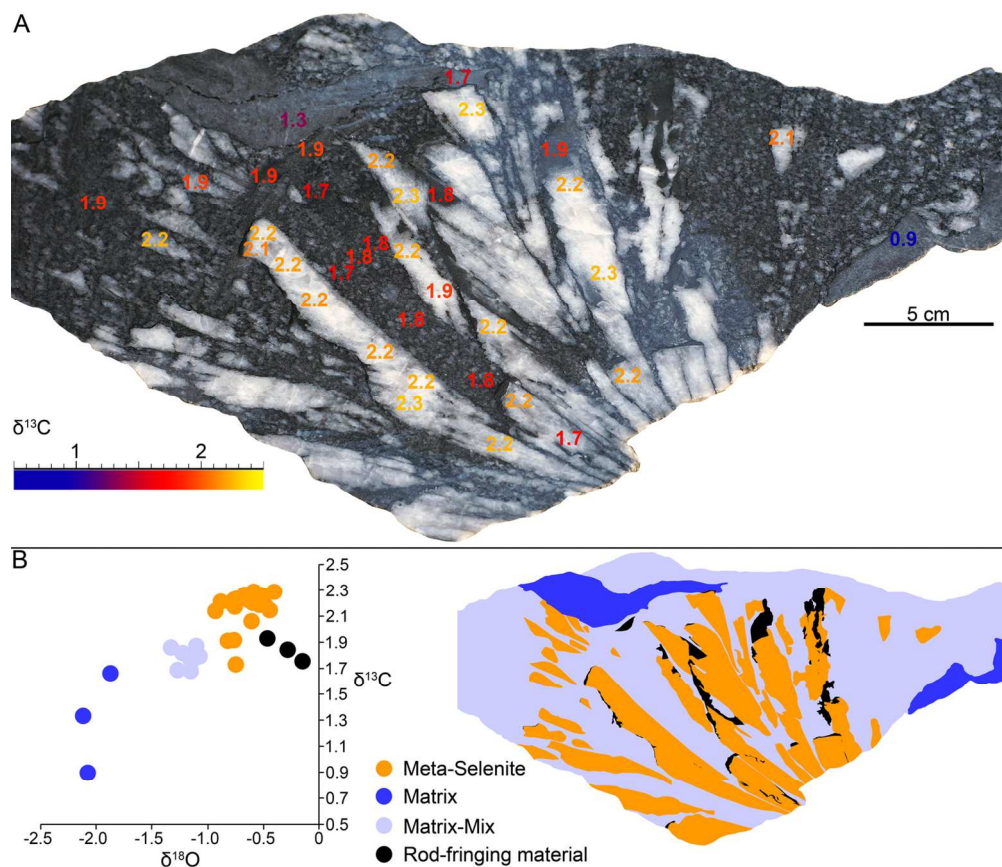
Carbon isotope mapping of a Rosetta Marble rock slab. Note the clustering according to the sampled material.

146x126mm (300 x 300 DPI)
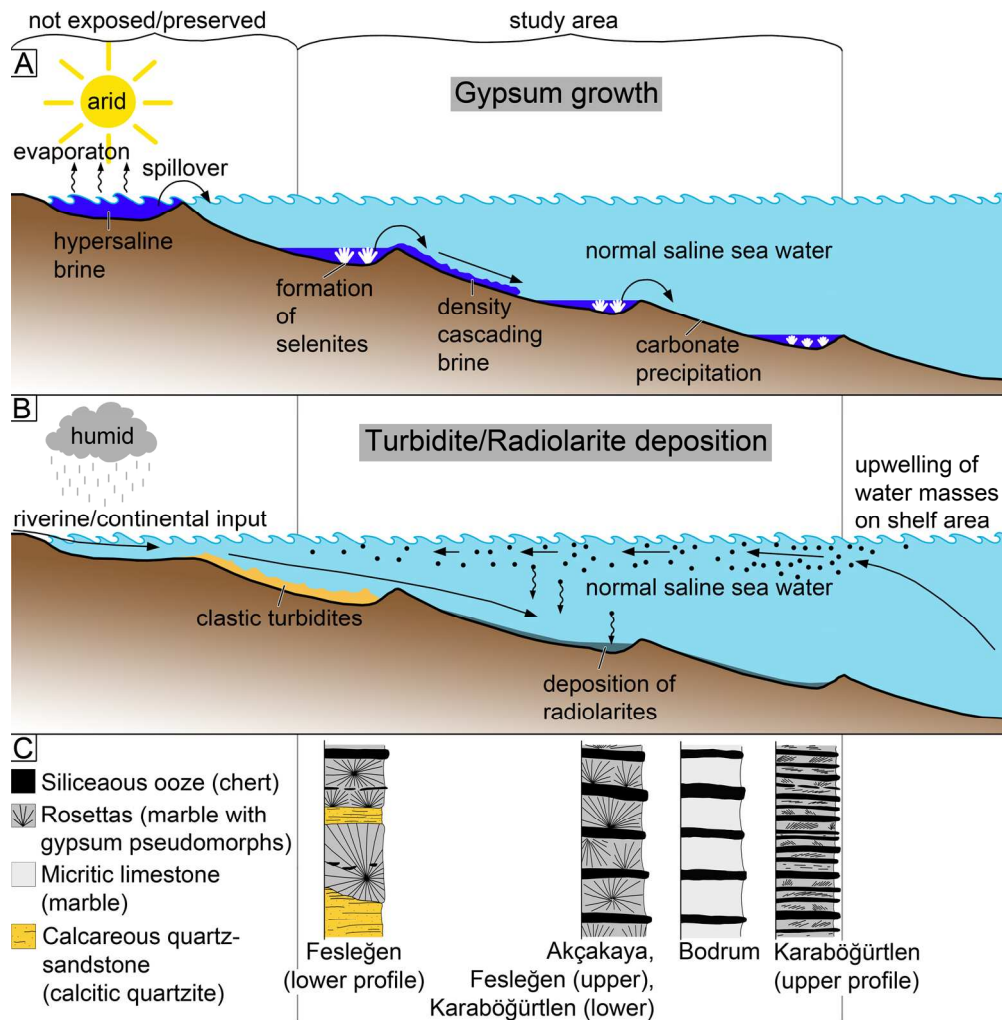
Depositional environmental model. (A) Gypsum growth mode. Regular spillovers of cascading brines serve as ion-supplies to the deeper and more distal parts. Gypsum growth takes place in restricted ponds and size of selenites correlate to the distance to the shore line. (B) Turbidite/Radiolarite deposition mode. Humid climate prevents wide evaporation. Upwelling water masses on shelf area serve for nutrient-rich water surface conditions that promote radiolarian bloom. Turbidites and radiolarites form at that stage. (C) Simplified stratigraphic sections corresponding from proximal to distal localities in the paleo basin.

170x171mm (300 x 300 DPI)
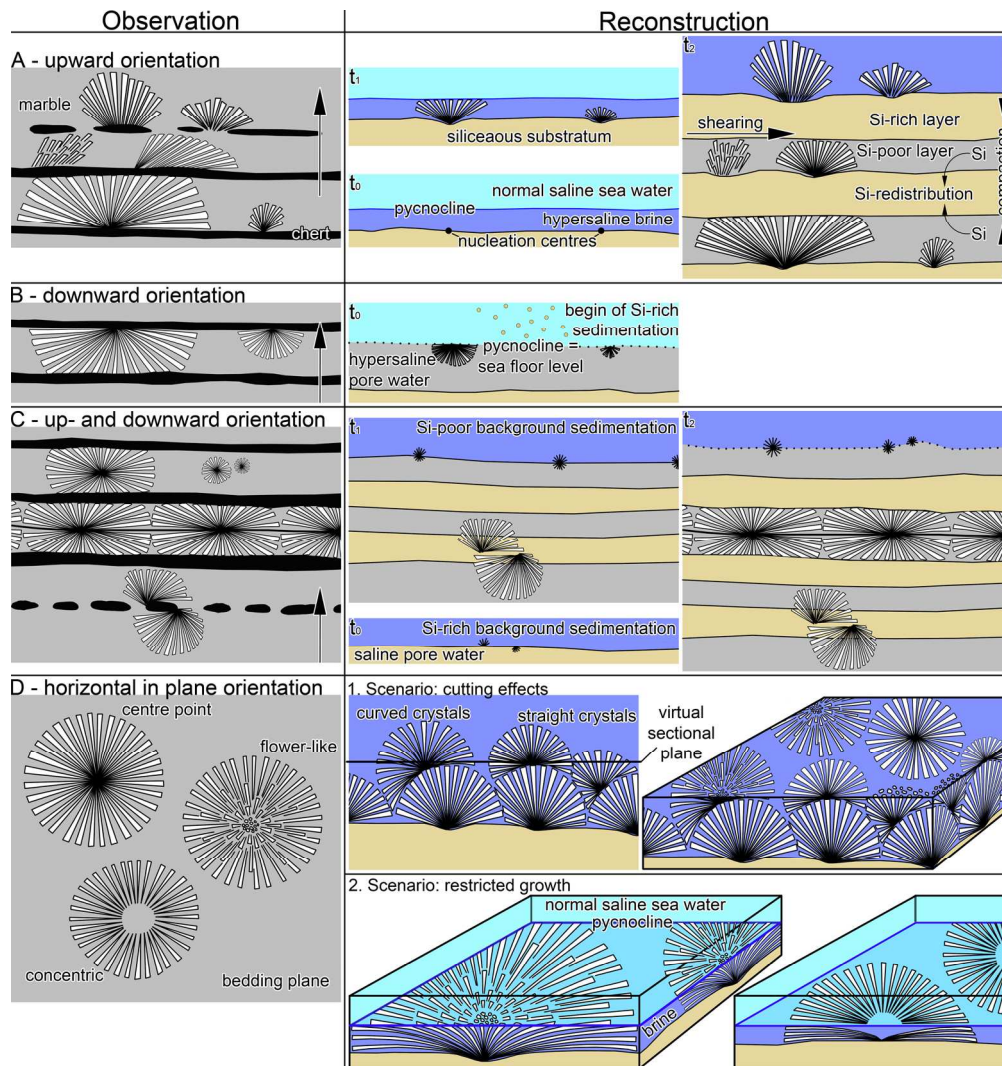
Observed growth geometries are documented and classified in the first column. Based on that, the primary growing conditions were reconstructed in the second column. (A) Upwards oriented fans grow at the sea floor (t0-t1) and can be restricted by the pycnocline level (t1). An alternation of fan-growing layers with Si-rich layers is causing the final appearance of the rock (t3) (B) Downward oriented fans grow displacive into the soft substratum (t0), which can be either Si-rich or Si-depleted. (C) A combination of A and B conditions is able to produce up- and downward oriented fans that are spherical in shape. (D) The most common horizontal radial crystals are either explained by cutting effects (1. Scenario), by restricted growth due to a shallow pycnocline level (2. Scenario), or, a combination of both scenarios.

170x179mm (300 x 300 DPI)
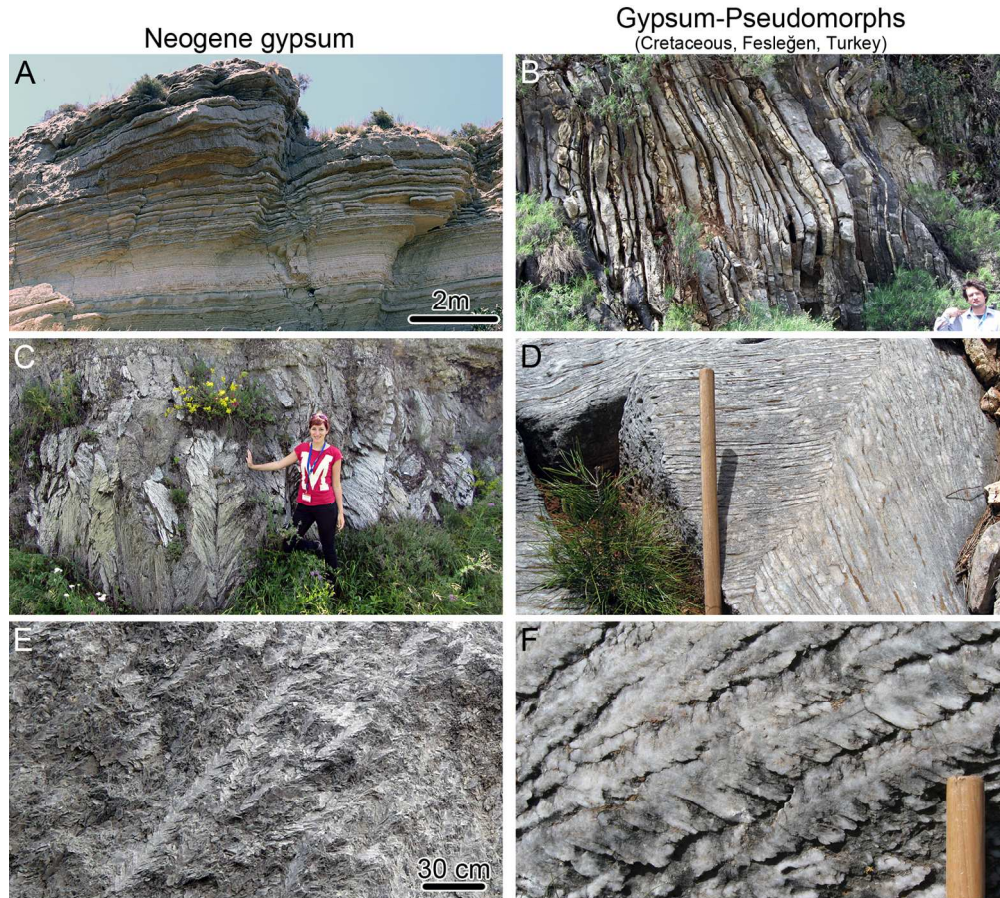
Textural comparison of Neogene selenitic gypsum deposits from the Mediterranean and the Paratethys basins, left column, with Cretaceous selenite pseudomorphs from Anatolia, right column. (A) Climate-driven alternations of gypsum and shale layers. Messinian, Sicily, Italy. (B) Regular selenite-pseudomorph-marble – meta-chert couplets. (C) Giant selenite intergrowth. Badenian, near Kraków, Poland. (D) Selenite pseudomorphs resembling giant intergrowth. (E) Stacked swallow-tail crystals (columnar symmetrical twins). Messinian, Piedmont, Italy. (F) Gypsum pseudomorphs resembling swallowtail twins. Hammer shaft width is 3 cm.

170x152mm (300 x 300 DPI)
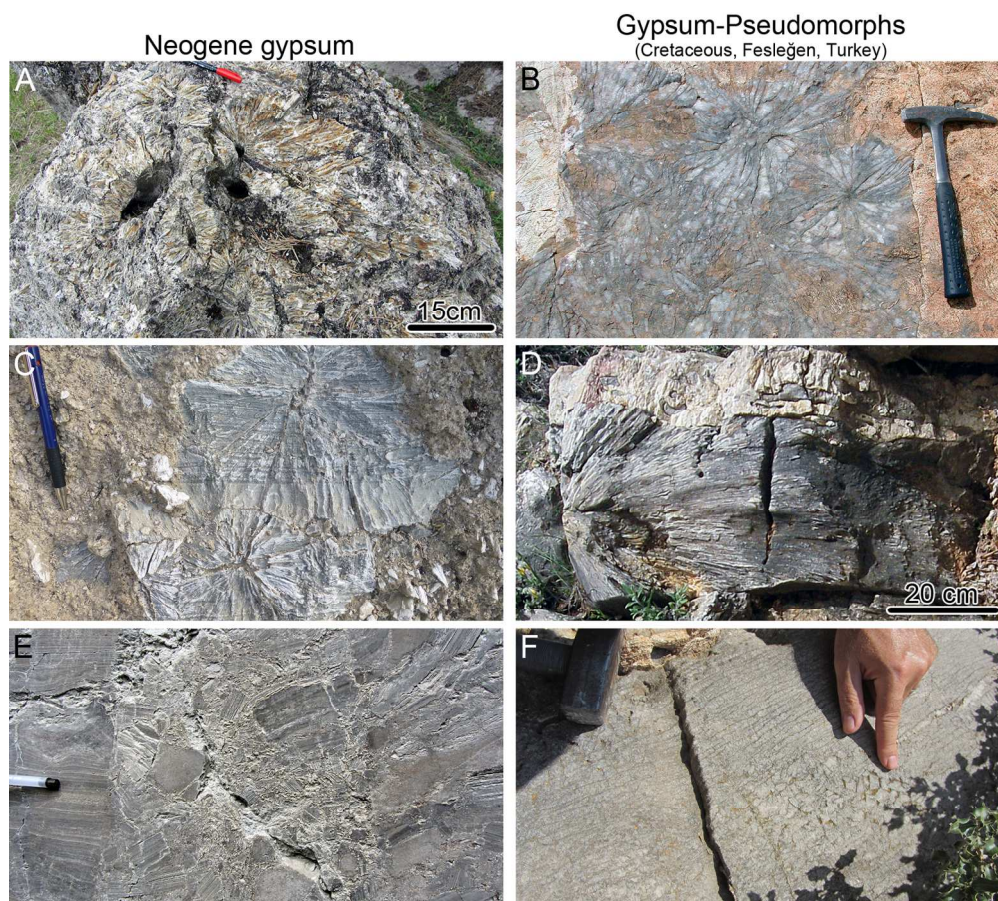
Textural comparison of Neogene selenitic gypsum deposits, left column, with Cretaceous selenite pseudomorphs from Anatolia, right column. (A) Radiating gypsum crystals around tree trunks. Badenian, near Kraków, Poland. (B) Radiating selenite-pseudomorphs on a bedding plane. (C) Radiating selenite crystals perpendicular (up- and downward) to the bedding plane. Messinian, Sicily, Italy. (D) Radiating selenite pseudomorph crystals perpendicular (up- and downward) to the bedding plane. Picture is tilted, see original in Fig. 5. (E) Layerd gypsum with in-situ brecciation. Badenian, near Kraków, Poland. (F) Layerd marble (meta-gypsum) with in-situ brecciation.

170x152mm (300 x 300 DPI)
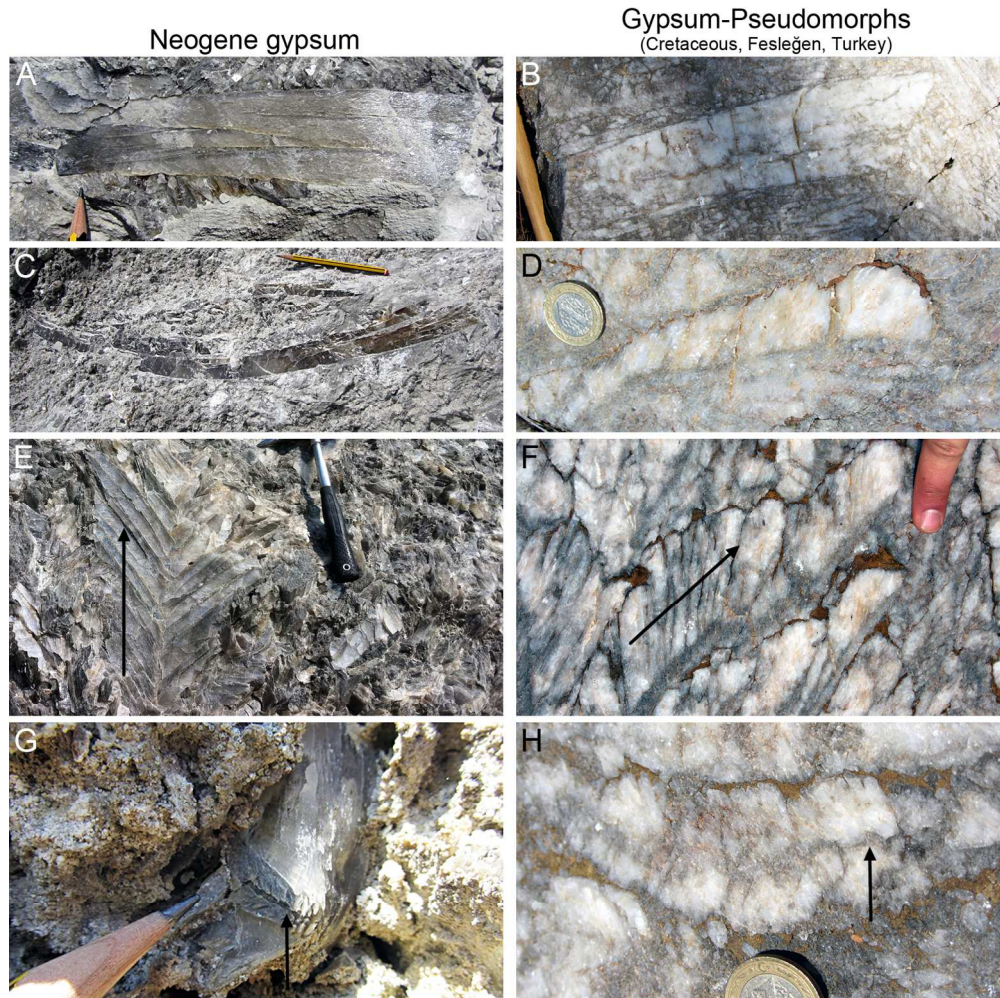
Textural comparison of Neogene selenitic gypsum deposits with Cretaceous selenite pseudomorphs from Anatolia. (A) Large sabre-like selenite crystal in a gypsum matrix. Bedenian, Kraków, Poland. (B) Large sabre-like selenite pseudomorh crystal in a marble matrix. (C) Curved sabre selenite crystals in a gypsum matrix. Bedenian, Kraków, Poland. (D) Curved sabre-like selenite psuedomroph crystal in a marble matrix. Note the calcite fibres that are pseudomorphic after aragonite. (E) Growing surfaces within a twinned selenite crystal. Arrow indicates growing direction. Messinian, Piedmont, Italy. (F) Growing surfaces of selenite pseudomorph crystals. (G) Re-entrant angle (dark gray portion) and twinning plane of a swallow-tail selenite crystal. Bedenian, Kraków, Poland. (H) Dark grey line (arrow) within swallowtail selenite pseudomorph crystals as relict of an impurity-rich twin plane.

170x168mm (300 x 300 DPI)

1
2
3
4
5
6
7
8
9
10
11
12
13
14
15
16
17
18
19
20
21
22
23
24
25
26
27
28
29
30
31
32
33
34
35
36
37
38
39
40
41
42
43
44
45
46
47
48
49
50
51
52
53
54
55
56
57
58
59
60

Table 1. Oxygen and Carbon isotope data. An outlier from Akçakaya was excluded: $\delta^{13}C = -0.64$‰ and $\delta^{18}O = -6.65$‰. An outlier from "All samples Feslegen" was excluded, probably a secondary vein was sampled: $\delta^{13}C = -0.75$‰ and $\delta^{18}O = -3.01$‰.

Sample sites	Spezification	Number of samples	$\delta^{18}O$				$\delta^{13}C$			
			min	max	mean	± s	min	max	mean	± s
Fesleğen	All samples	50	−3.84‰	−0.56‰	−1.46‰	0.1	+1.35‰	+2.52‰	+1.97‰	0.05
	Upper profile	16	−2.48‰	−0.93‰	−1.44‰	0.1	+1.91‰	+2.52‰	+2.32‰	0.04
	Lower profile	14	−3.84‰	−1.28‰	−1.79‰	0.9	+1.51‰	+2.27‰	+1.72‰	0.05
Karaböğürtlen	Upper profile	23	−5.35‰	−1.78‰	−2.72‰	0.07	+2.78‰	+3.93‰	+3.29‰	0.05
	Lower profile	15	−2.24‰	−0.50‰	−1.28‰	0.08	+1.13‰	+2.42‰	+1.67‰	0.05
Akçakaya		52	−2.20‰	−0.63‰	−1.79‰	0.09	+0.93‰	+2.24‰	+1.32‰	0.06
Bodrum		7	-1.77‰	-0.81‰	−1.41‰	0.06	0.99‰	2.27‰	+1.69‰	0.04
Ören		2	-0.925‰	-1.177‰	−1.051‰	0.1	0.973‰	0.980‰	+0.976‰	0.03

1
2
3
4
5
6
7
8
9
10
11
12
13
14
15
16
17
18
19
20
21
22
23
24
25
26
27
28
29
30
31
32
33
34
35
36
37
38
39
40
41
42
43
44
45
46
47
48
49
50
51
52
53
54
55
56
57
58
59
60

Table 1. Strontium isotope data.

Sample site	Detailed sample site	Number of samples	$^{87}Sr/^{86}Sr$			
			min	max	mean	± 2 σ_{mean}
Fesleğen	Upper profile	8	0.707479	0.707593	0.707522	0.000008
	Lower profile	5	0.707511	0.707664	0.707551	0.000008
Karaböğürtlen	Upper profile	5	0.7073379	0.7076933	0.7075578	0.000008
	Lower profile	6	0.7072873	0.7074792	0.7074066	0.000008
Akçakaya	Profile	12	0.707276	0.707664	0.707368	0.000008

1
2
3
4
5
6
7
8
9
10
11
12
13
14
15
16
17
18
19
20
21
22
23
24
25
26
27
28
29
30
31
32
33
34
35
36
37
38
39
40
41
42
43
44
45
46
47
48
49
50
51
52
53
54
55
56
57
58
59
60

Supplementary Material

Supplementary Figure A – 170mm
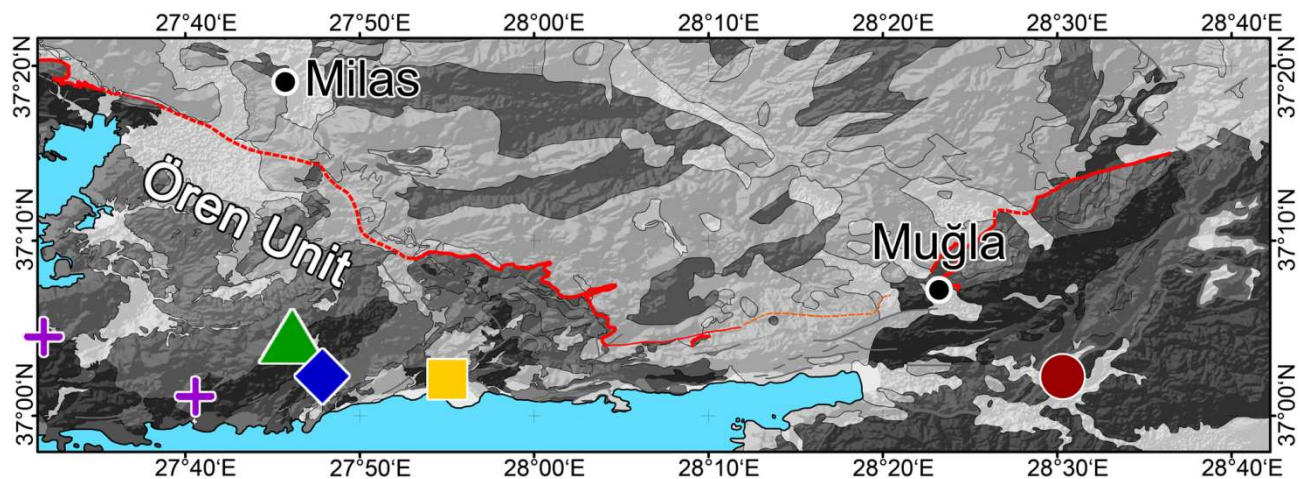
Fig. A. Sample location overview (see main text for coordinates). The map is based on Rimmelé *et al.* (2005), the official geological map of Turkey (MTA 2002) and Scheffler *et al.* (2016). Green triangle: Fesleğen, Blue rhomb: Akçakaya, Red circle: Karaböğürtlen, Yellow square: Ören, Violet crosses: Bodrum.

Supplementary Figure B – 170mm
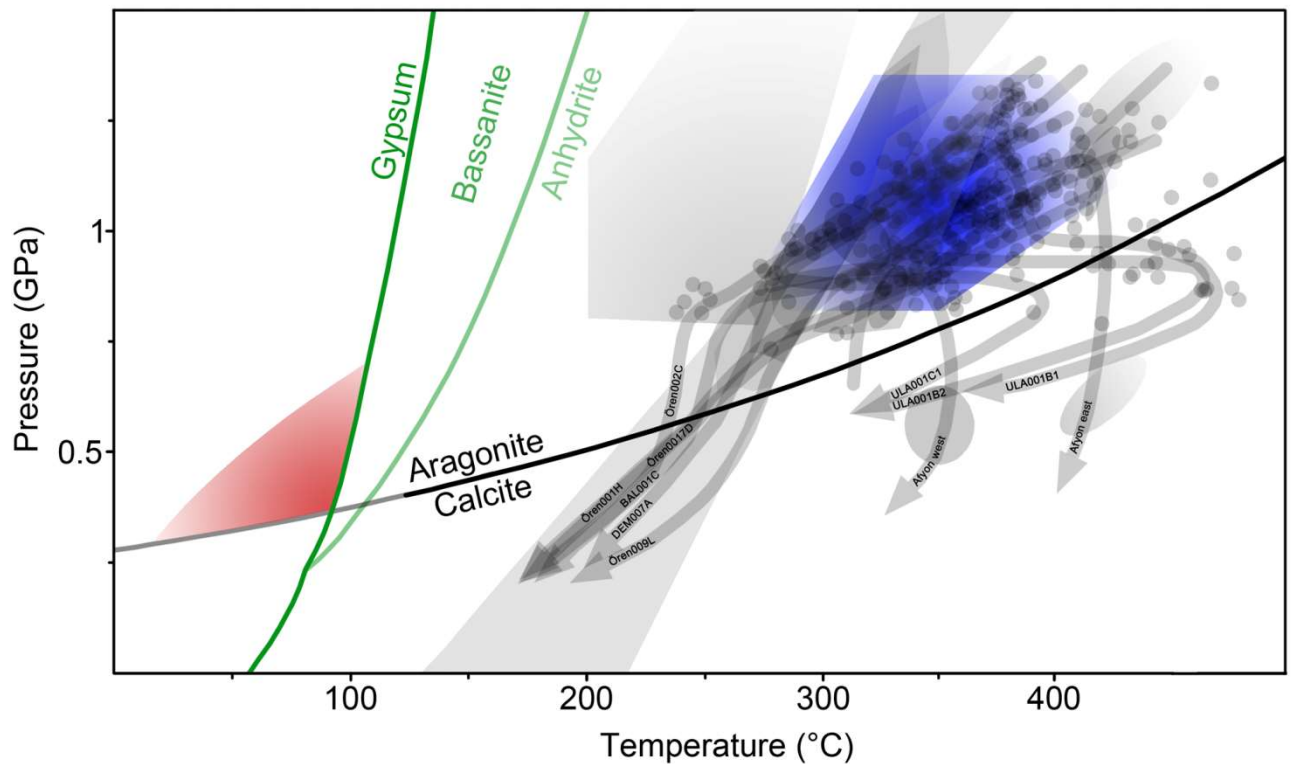
Fig. B. PT-diagram including all data points published by Rimmelé *et al.* (2005) from the samples DEM007A + BAL001C (both are located north of the Akçakaya fault and represent the closest samples to the Fesleğen and Akçakaya samples), Ören0017D + Ören002C + Ören001H (all three locations are south of the Akçakaya fault) and ULA001B1 + ULA001B2 + ULA001C1 (all three locations are the closest samples to Karaböğürtlen). The arrows for these samples are suggested by Rimmelé *et al.* (2005). Furthermore, data from Pourteau *et al.* (2014) were included and suggested PT-path-arrows delineated. Quartz-water-phengite-thermobarometry calculations from Scheffler *et al.* (2016) are shown in transparent-grey, whereas the darkest grey area represents the field of highest probability. The data for this calculation are directly taken from Fesleğen-samples. Since the DEM007A + BAL001C samples, the western Afyon zone PT-path and the quartz-water-phengite-data are the most nearest to the location of interest, the blue area that is representing the peak PT-conditions, is mostly oriented on these data.

Dubacq, B., Vidal, O. and **De Andrade, V.** (2010) Dehydration of dioctahedral aluminous phyllosilicates: thermodynamic modelling and implications for thermobarometric estimates. Contrib. Mineral. Petrol., **159**, 159–174

Supplementary Figure C – 230mm high
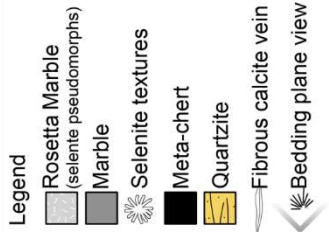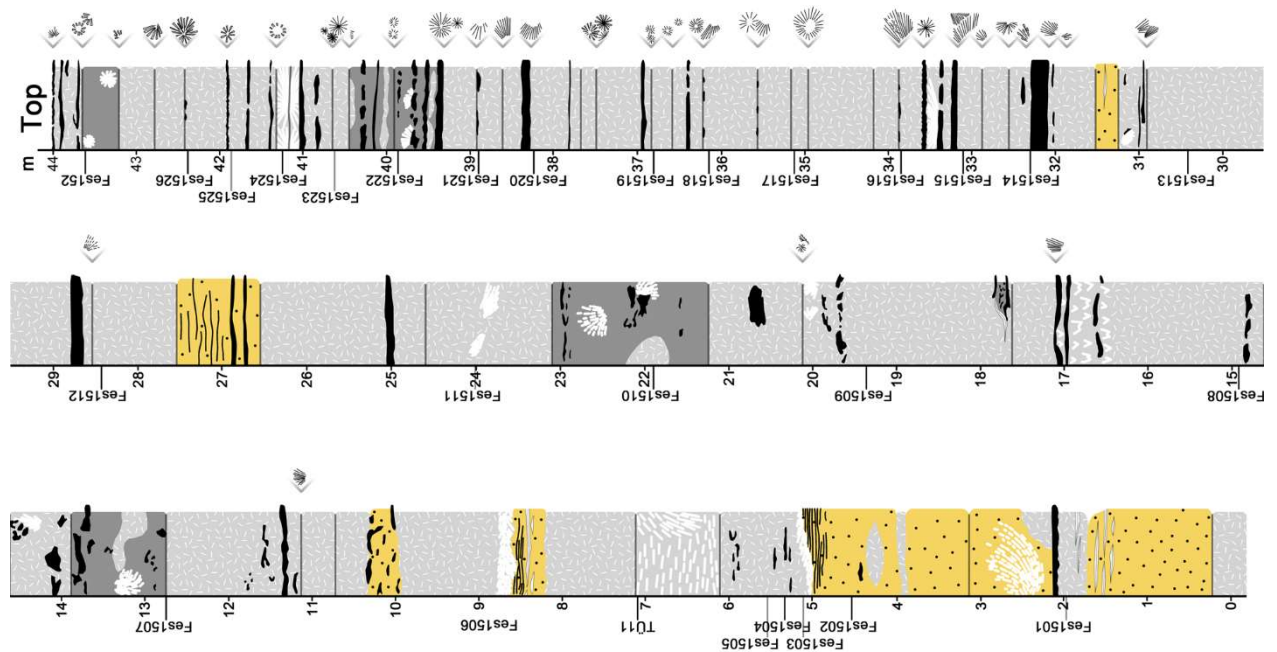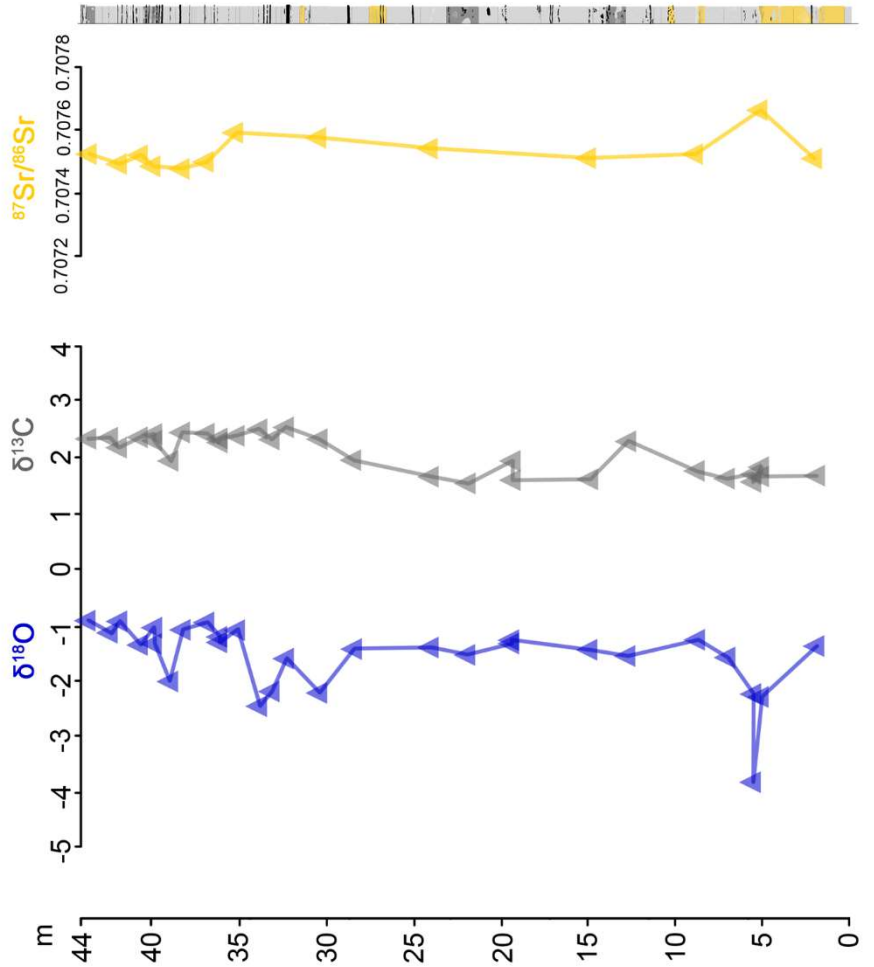
Fig. C. δ^{18}O, δ^{13}C and [87]Sr/[86]Sr data of the Fesleğen profile. The y-axis represents the distance in the profile and correlates with the shown log on the right side of the figure. Note that the isotope data of the first 15 meters correlate with the thin and regular selenite pseudomorph bearing marble – meta-chert layers of the profile. Downsection the marble beds become thicker, the meta-chert layers decrease and quartzitic layers occur more frequently. For a more detailed sedimentological description of the lower part of this log, see Scheffler *et al.* (2016). Maximal errors for oxygen-, carbon- and Sr-isotopes are smaller than the chosen symbol-size.

Supplementary Figure D – 170mm
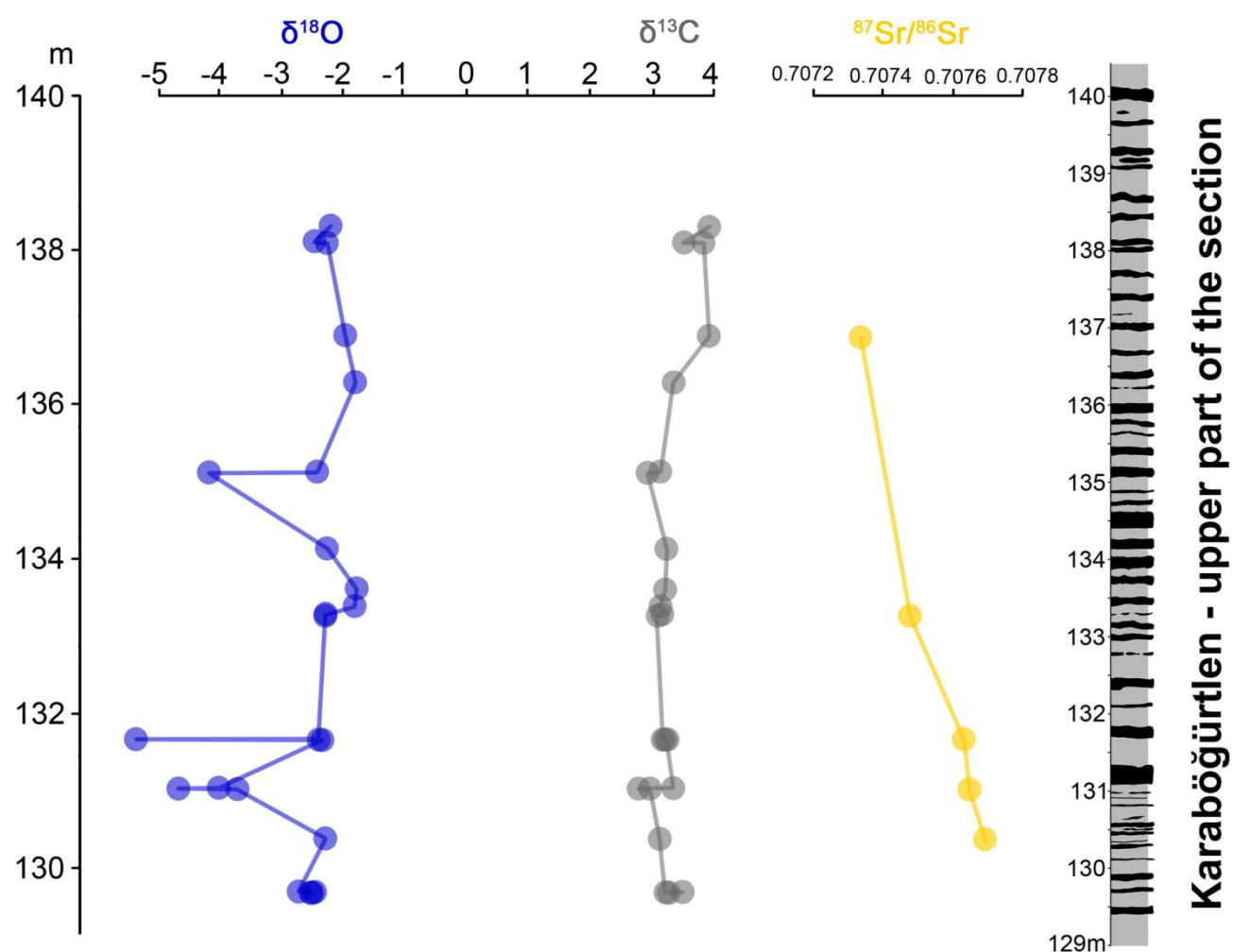
Fig. D. δ^{18}O, δ^{13}C and [87]Sr/[86]Sr data of the upper part of the Karaböğürtlen section. The y-axis represents the distance in the profile and correlates with the shown log on the right side of the figure. Grey layers are selenite pseudomorph bearing marble, black layers are meta-hert intervals with occasionally meta-wackestone rims. Maximal errors for oxygen-, carbon- and Sr-isotopes are smaller than the chosen symbol-size.

Supplementary Figure E – 230mm high
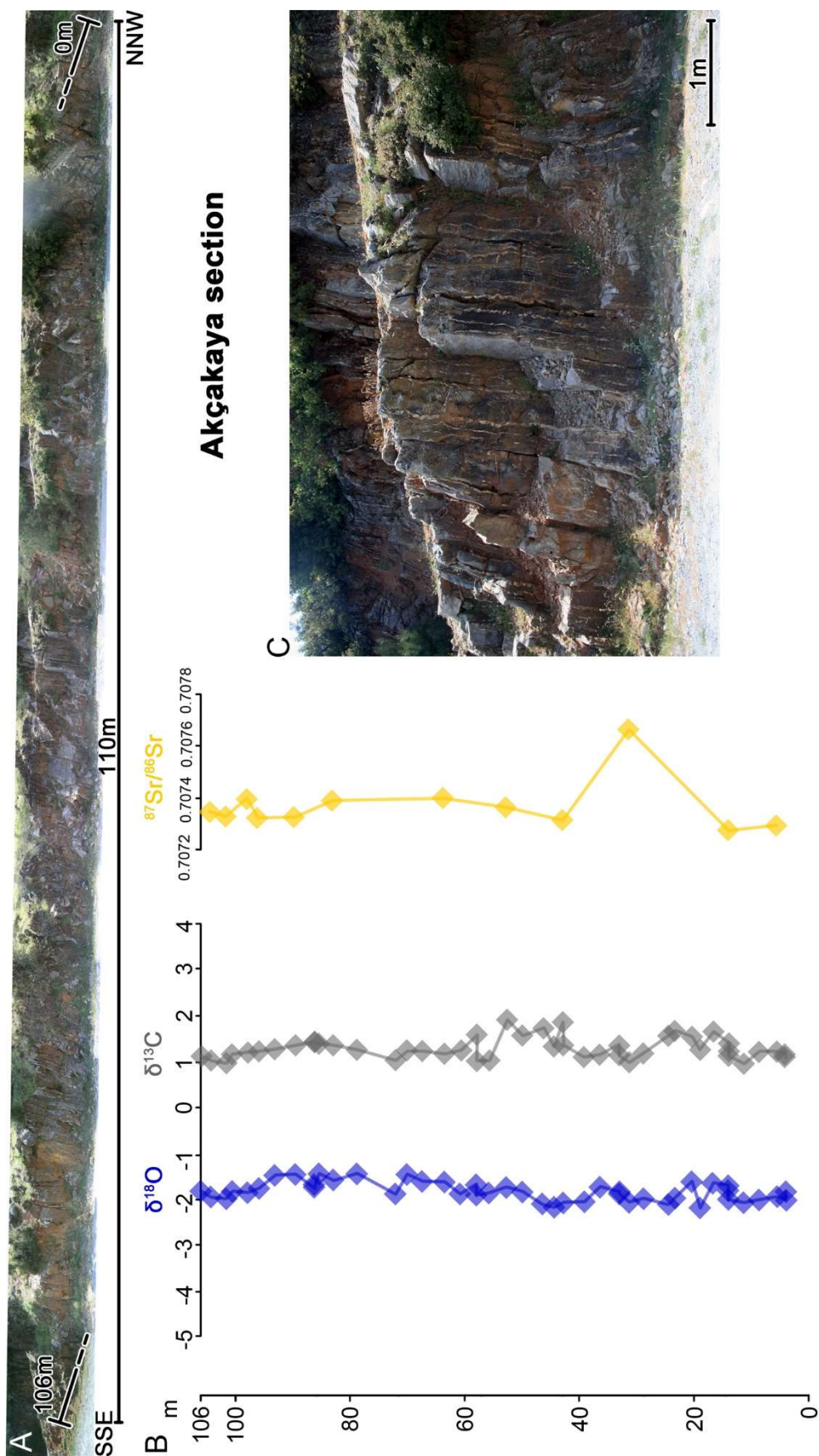
Akçakaya section

Fig. E.δ^{18}O, δ^{13}C and ^{87}Sr/^{86}Sr data of the Akçakaya profile. The y-axis represents the distance in the profile and correlates with the shown photograph of the sampled section. (A). The isotopes of this very regular profile are very homogeneous. The oxygen- and carbon-curves slightly follow the same up- and downs. (C) Character of the marble-chert-alternations of this profile in a close-up view. Maximal errors for oxygen-, carbon- and Sr-isotopes are smaller than the chosen symbol-size.

Supplementary Figure F – 230mm high

Fig. F. Rosetta Marble rock slab. Radiating white calcite rods are pseudomorphs after selenite. Circles mark the exact sampling spots of micro-drilling for ^{13}C and [18]O analysis.

Supplementary Figure G – 170mm
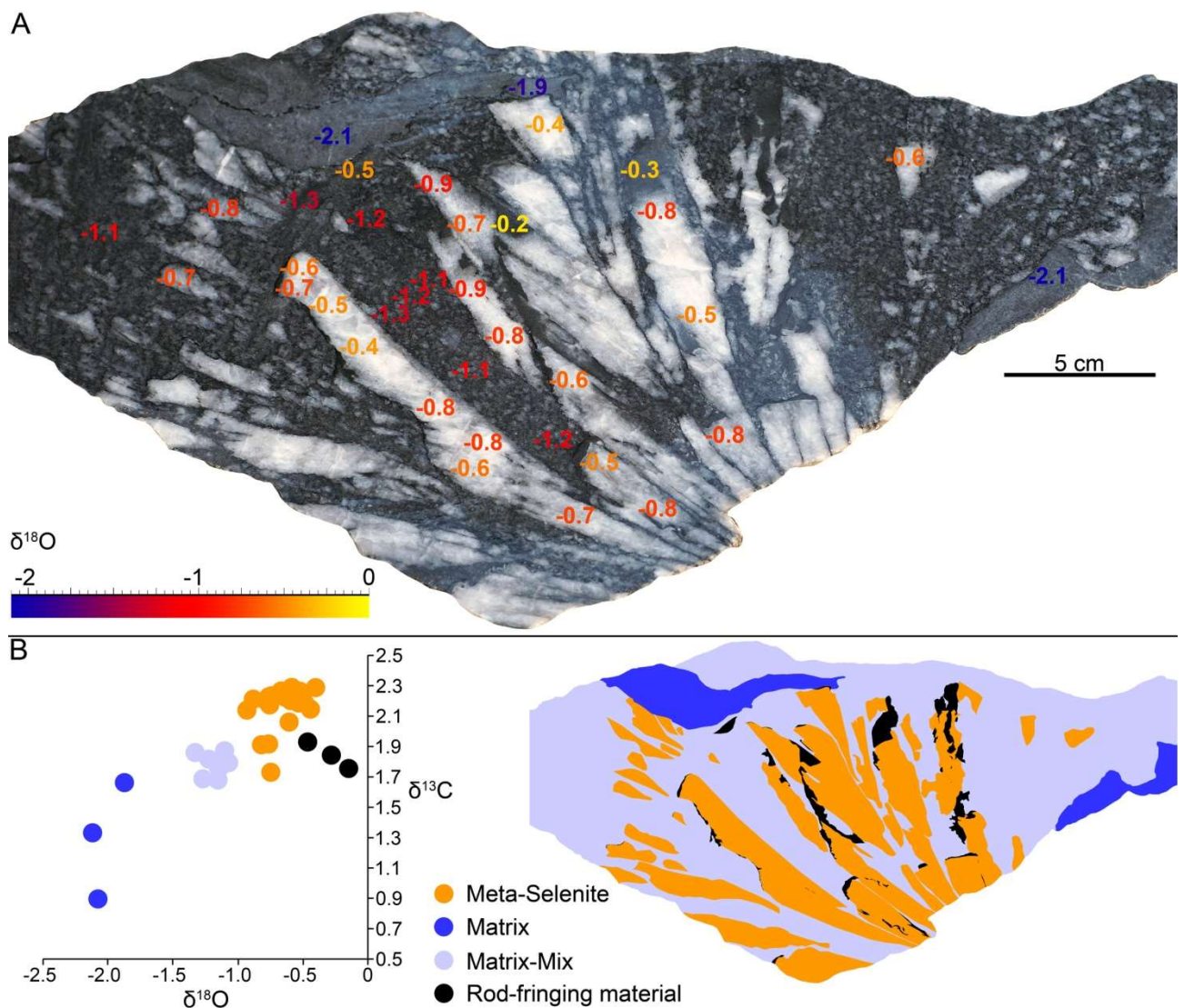
Fig. G. Oxygen isotope mapping of a Rosetta Marble rock slab. Note the clustering according to the sampled material.

Supplementary Figure H – 170mm
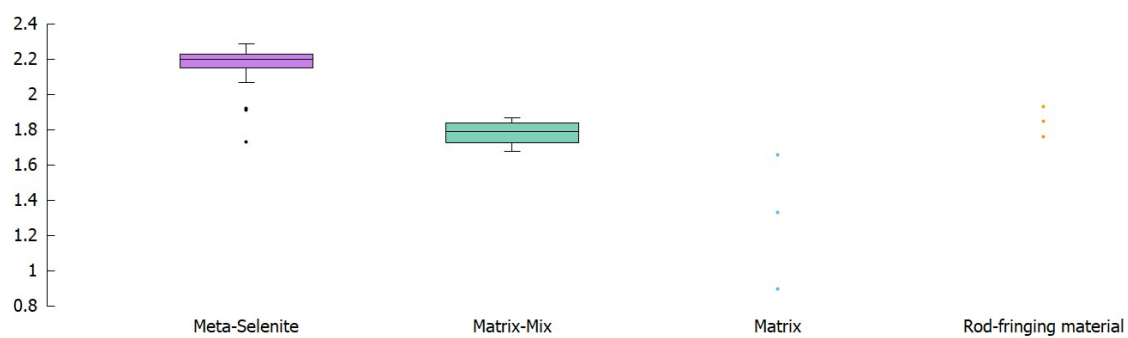
Fig. H. Boxplot of the ^{13}C Isotopes of the analysed rock slab. Distinguishable populations.

Supplementary Figure I – 170mm
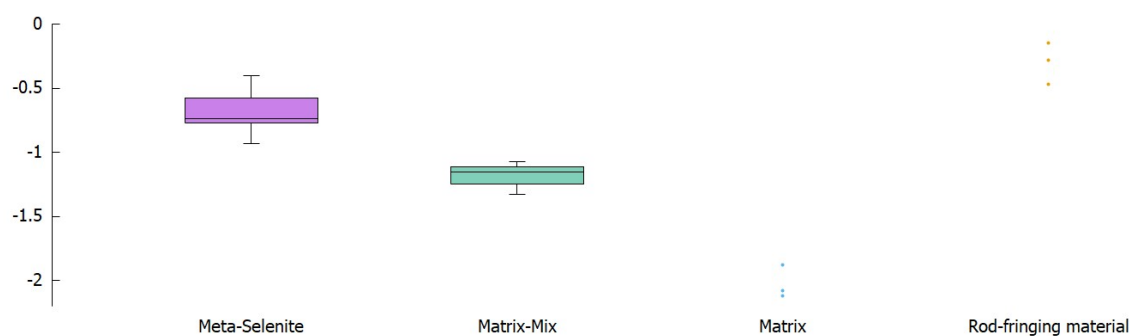
Fig. I. Boxplot of the ^{18}O Isotopes of the analysed rock slab. Distinguishable populations.

1
2
3   <u>Supplementary Data Table A:</u> Carbon and Oxygen isotopes
4
5
6   The Table shows all Carbon and Oxygen data that were included in graphs and calculations of the
7   paper. Not shown are data that have not fulfilled the quality criteria (too high max. amplitude, not
8   enough $CaCO_3$ content for the measurement) and were therefore excluded. From samples that were
9
10   measured twice, a mean value was calculated.
11

| | | | | corrected values | | | | | |
sample name	Nr.	sample weight [mg]	max. Amplitude [V]	$d^{13}C_{PDB}$ [‰]	± s	$d^{18}O_{PDB\text{-}carbonate}$ [‰]	± s	date	Position in the profile [cm]	Corresponding Sr ratios
Karaböğürtlen Profile									14000	
Kar1531	GB 55210	0.60	9715	3,93	0,03	-2,20	0,07	03.03.2016	13829	
Kar1412-B	GB 54698	0.40	4111	3,52	0,03	-2,45	0,03	14.01.2016	13809	
Kar1512-A	GB 54697	0.41	4971	3,84	0,05	-2,26	0,06	14.01.2016	13807	
Kar1515	GB 54359	0.43	6975	3,93	0,03	-1,97	0,05	16.12.2015	13688	0,707337856
Kar1536	GB 55212	0.61	9859	3,35	0,04	-1,81	0,05	03.03.2016	13627	
Kar1508-A	GB 54382	1.26	4245	3,13	0,05	-2,42	0,05	16.12.2015	13512	
Kar1508-B	GB 54693	1.80	3419	2,93	0,05	-4,16	0,07	14.01.2016	13510	
Kar1534	GB 55216	0.55	7877	3,23	0,03	-2,25	0,02	03.03.2016	13412	
Kar1537	GB 55211	0.52	8089	3,20	0,04	-1,78	0,05	03.03.2016	13360	
Kar1535	GB 55214	0.62	8747	3,13	0,02	-1,81	0,04	03.03.2016	13338	
Kar1505-B	GB 54696	0.41	6422	3,17	0,04	-2,28	0,06	14.01.2016	13327	0,707477868
Kar1505-A	GB 54695	0.40	5512	3,07	0,04	-2,29	0,05	14.01.2016	13325	
Kar1518-C	GB 54373	0.47	6847	3,17	0,02	-2,40	0,02	16.12.2015	13167	
Kar1518-A	GB 54687	0.40	6409	3,14	0,04	-5,35	0,04	14.01.2016	13166	0,707631826
Kar1518-B	GB 54371	0.44	6393	3,23	0,05	-2,34	0,05	16.12.2015	13166	
Kar1503-D	GB 54684	0.42	5517	3,34	0,03	-4,00	0,04	14.01.2016	13103	
Kar1503-A	GB 54363	0.41	6861	2,78	0,03	-4,65	0,03	16.12.2015	13102	0,707648277
Kar1503-B	GB 54364	0.48	7565	2,96	0,03	-3,71	0,06	16.12.2015	13102	
Kar1501	GB 54688	0.41	5413	3,12	0,04	-2,29	0,06	14.01.2016	13037	0,707693279
Kar1502-D	GB 54692	0.55	4676	3,19	0,03	-2,71	0,05	14.01.2016	12969	
Kar1502-C	GB 54690	0.40	5696	3,48	0,04	-2,51	0,04	14.01.2016	12969	
Kar1502-B	GB 54379	1.73	6948	3,49	0,03	-2,46	0,06	16.12.2015	12969	
Kar1502-A	GB 54689	0.41	5606	3,27	0,04	-2,47	0,05	14.01.2016	12968	
Kar1519	GB 54342	0.42	7431	2,41	0,03	-2,24	0,08	15.12.2015	10898	
Kar1520-A	GB 54201	0.41	8928	1,87	0,02	-0,65	0,07	23.11.2015	9860	0,707467854
Kar1521	GB 54346	0.43	7781	1,87	0,04	-0,50	0,05	15.12.2015	8125	0,707453847
Kar1522-A	GB 54343	0.48	7437	1,36	0,03	-1,46	0,06	15.12.2015	7493	
Kar1522-B	GB 54344	0.42	7279	1,42	0,03	-1,58	0,05	15.12.2015	7490	
Kar1523-B	GB 54339	0.38	6693	1,47	0,03	-0,96	0,06	15.12.2015	7246	
Kar1523-A	GB 54338	0.41	7425	1,94	0,03	-0,90	0,05	15.12.2015	7245	0,707479239
Kar1525A	GB 54329	0.38	6337	2,42	0,05	-1,08	0,05	15.12.2015	6109	
Kar1526	GB 54326	0.39	6236	1,75	0,02	-1,15	0,07	15.12.2015	4171	0,707406819
Kar1527-A	GB 54334	0.39	6185	1,69	0,03	-1,31	0,05	15.12.2015	4152	
Kar1527-B	GB 54335	0.38	4580	1,13	0,03	-1,79	0,07	15.12.2015	2847	

Kar1527-C	GB 54337	0.42	5780	1,18	0,04	-1,86	0,09	15.12.2015	2846	
Kar1528-A	GB 54323	0.40	6342	1,20	0,04	-1,27	0,05	15.12.2015	2845	
Kar1528-B	GB 54325	0.39	6344	1,61	0,03	-1,01	0,05	15.12.2015	1245	0,707344830
Kar1530	GB 54328	0.42	6875	1,70	0,03	-1,48	0,05	15.12.2015	1180	0,707287252
Excluded because of very negative O values:										
Kar1509-B	GB 54361	0.39	6774	2,91	0,03	-13,25	0,05	16.12.2015		
Akçakaya Profile										
Fes1580	GB 54220	0.37	7354	1,10	0,04	-1,85	0,08	24.11.2015	10600	
Fes1579	GB 54218	0.39	7896	1,00	0,03	-1,95	0,08	24.11.2015	10436	0,707345247
Fes1578-B	GB 54214	0.39	7605	0,94	0,05	-2,01	0,07	24.11.2015	10167	0,707328856
Fes1577	GB 54219	0.41	8313	1,14	0,04	-1,85	0,06	24.11.2015	10072	
Fes1576	GB 54217	0.39	7989	1,18	0,04	-1,87	0,07	24.11.2015	9795	0,707393825
Fes1575-A	GB 54216	0.40	8048	1,20	0,03	-1,78	0,09	24.11.2015	9605	0,707321823
Fes1574-A	GB 54262	0.40	7081	1,25	0,02	-1,49	0,06	30.11.2015	9328	
Fes1573A	GB 54222	0.43	8594	1,33	0,02	-1,47	0,07	24.11.2015	8964	0,707326233
Fes1572-A	GB 54224	0.39	7538	1,40	0,03	-1,77	0,08	24.11.2015	8644	
Fes1572-B	GB 54225	0.41	8521	1,42	0,05	-1,71	0,07	24.11.2015	8644	
Fes1571-A	GB 54265	0.40	7391	1,37	0,03	-1,47	0,04	30.11.2015	8557	
Fes1570	GB 54215	0.40	7571	1,34	0,04	-1,59	0,07	24.11.2015	8306	0,707387865
Fes1569-A	GB 54294	0.41	8053	1,24	0,03	-1,46	0,07	30.11.2015	7900	
Fes1567-A	GB 54395	0.38	7063	1,01	0,06	-1,90	0,05	16.12.2015	7225	
Fes1566-A	GB 54287	0.40	7534	1,22	0,02	-1,48	0,05	30.11.2015	7017	
Fes1565-A	GB 54295	0.41	8084	1,21	0,02	-1,61	0,05	30.11.2015	6757	
Fes1564-A	GB 54362	0.40	6477	1,15	0,05	-1,64	0,05	16.12.2015	6368	0,707399845
Fes1563-A	GB 54299	0.42	7726	1,22	0,03	-1,90	0,06	30.11.2015	6082	
Fes1562-A	GB 54291	0.40	7521	1,57	0,02	-1,70	0,05	30.11.2015	5805	
Fes1562-B	GB 54293	0.43	8237	0,99	0,02	-1,92	0,08	30.11.2015	5805	
Fes1561-B	GB 54298	0.42	6917	1,00	0,03	-1,87	0,06	30.11.2015	5589	
Fes1560	GB 54290	0.40	7918	1,89	0,05	-1,76	0,07	30.11.2015	5277	0,707363844
Fes1559	GB 54289	0.39	7571	1,55	0,03	-1,86	0,03	30.11.2015	5009	
Fes1558-A	GB 54202	0.39	8134	1,70	0,03	-2,12	0,08	23.11.2015	4645	
Fes1557	GB 54347	0.42	7163	1,30	0,03	-2,18	0,06	15.12.2015	4455	
Fes1556-A	GB 54332	0.40	6843	1,83	0,01	-2,10	0,03	15.12.2015	4299	0,707314849
Fes1556-B	GB 54333	0.40	6318	1,33	0,04	-2,10	0,03	15.12.2015	4299	
Fes1555	GB 54341	0.40	6605	1,08	0,04	-2,07	0,09	15.12.2015	3936	
Fes1554-A	GB 54388	0.39	6288	1,13	0,04	-1,75	0,03	16.12.2015	3659	
Fes1553-A	GB 54284	0.41	5910	1,33	0,04	-1,85	0,05	30.11.2015	3321	
Fes1553-B	GB 54285	0.42	7918	1,12	0,02	-1,89	0,05	30.11.2015	3321	
Fes1552	GB 54286	0.43	8036	0,97	0,03	-2,08	0,03	30.11.2015	3148	0,707663834
Fes1551	GB 54331	0.40	6745	1,16	0,03	-2,00	0,05	15.12.2015	2897	
Fes1550-A	GB 54330	0.40	6873	1,54	0,05	-2,12	0,05	15.12.2015	2464	
Fes1549	GB 54241	0.42	8756	1,65	0,03	-1,99	0,09	24.11.2015	2352	
Fes1548-B	GB 54376	0.40	6549	1,52	0,05	-1,63	0,08	16.12.2015	2049	
Fes1547	GB 54248	0.39	6211	1,24	0,03	-2,20	0,09	24.11.2015	1910	
Fes1546	GB 54282	0.41	7830	1,63	0,02	-1,67	0,04	30.11.2015	1677	
Fes1545-A	GB 54270	0.41	7319	1,37	0,03	-1,72	0,03	30.11.2015	1408	0,707275867
Fes1545-B	GB 54271	0.40	7492	1,20	0,04	-1,83	0,04	30.11.2015	1408	
Fes1545-C	GB 54272	0.40	7591	1,10	0,02	-2,02	0,04	30.11.2015	1408	
Fes1544	GB 54252	0.44	8746	0,93	0,03	-2,09	0,09	24.11.2015	1149	

Sedimentology

Fes1543	GB 54251	0.40	8107	1,19	0,03	-2,03	0,08	24.11.2015	880	
Fes1541-A	GB 54247	0.42	8277	1,20	0,02	-1,97	0,08	24.11.2015	569	0,707293272
Fes1540-A	GB 54246	0.45	9136	1,06	0,03	-2,03	0,09	24.11.2015	422	
Fes1540-B	GB 54394	0.45	7465	1,14	0,03	-1,85	0,02	16.12.2015	422	
excluded outlier:										
Fes1548-A	GB 54374	0.40	6796	-0,64	0,02	-6,65	0,03	16.12.2015		
Fesleğen profile									4400	
Fes1527	GB 54268	0.41	8049	2,31	0,03	-0,93	0,04	30.11.2015	4361	0,707524836
Fes1526	GB 54264	0.39	6291	2,33	0,02	-1,15	0,04	30.11.2015	4238	
Fes1525	GB 54238	0.42	8471	2,15	0,04	-0,94	0,07	24.11.2015	4186	0,707493842
Fes1523	GB 54239	0.42	8328	2,34	0,02	-1,37	0,07	24.11.2015	4062	0,707521856
Fes1522-A	GB 54278	0.39	7648	2,40	0,03	-1,06	0,08	30.11.2015	3986	0,707487226
Fes1522-B	GB 54281	0.38	7712	2,28	0,03	-1,34	0,04	30.11.2015	3986	
Fes1521	GB 54277	0.41	7579	1,91	0,02	-2,02	0,03	30.11.2015	3890	
Fes1520	GB 54229	0.41	8206	2,42	0,04	-1,10	0,08	24.11.2015	3824	0,707478821
Fes1519	GB 54230	0.41	8145	2,40	0,02	-0,97	0,10	24.11.2015	3680	0,707501233
Fes1518-A	GB 54242	0.41	8223	2,25	0,04	-1,22	0,07	24.11.2015	3614	
Fes1518-B	GB 54243	0.40	8326	2,31	0,02	-1,33	0,08	24.11.2015	3614	
Fes1517	GB 54234	0.41	8359	2,36	0,02	-1,10	0,08	24.11.2015	3512	0,707592845
Fes1516	GB 54233	0.41	8482	2,49	0,03	-2,48	0,09	24.11.2015	3385	
Fes1515	GB 54236	0.41	8731	2,30	0,03	-2,21	0,06	24.11.2015	3312	
Fes1514	GB 54275	0.44	8395	2,52	0,03	-1,61	0,06	30.11.2015	3230	
Fes1513	GB 54261	0.41	7282	2,31	0,04	-2,23	0,03	30.11.2015	3041	0,707576871
Fes1512	GB 54227	0.41	8629	1,92	0,02	-1,45	0,08	24.11.2015	2843	
Fes1511	GB 54276	0.42	7908	1,63	0,05	-1,42	0,06	30.11.2015	2401	0,707543254
Fes1510	GB 54274	0.39	7252	1,51	0,04	-1,55	0,05	30.11.2015	2190	
Fes1509A	GB 54232	0.43	8652	1,91	0,03	-1,35	0,09	24.11.2015	1936	
Fes1509B	GB 54237	0.41	8016	1,57	0,03	-1,29	0,07	24.11.2015	1936	
Fes1508	GB 54226	0.42	8965	1,58	0,04	-1,45	0,07	24.11.2015	1493	0,707512856
Fes1507	GB 54283	0.41	7753	2,27	0,03	-1,57	0,05	30.11.2015	1275	
Fes1506	GB 54228	0.39	8737	1,74	0,04	-1,28	0,08	24.11.2015	882	0,707525849
TÜ11 A				1,59	0,02	-1,59	0,04		709	
Fes1505-A	GB 54273	0.41	7605	1,68	0,05	-2,25	0,05	30.11.2015	558	
Fes1505-B	GB 54389	0.43	7811	1,53	0,03	-3,84	0,05	16.12.2015	558	
Fes1503-A	GB 54385	0.41	6906	1,81	0,02	-2,30	0,04	16.12.2015	512	0,707663834
Fes1503-B	GB 54386	0.42	5829	1,63	0,03	-2,32	0,05	16.12.2015	511	
Fes1501-A	GB 54266	0.41	7075	1,65	0,05	-1,39	0,05	30.11.2015	197	0,707511246
Additional Fesleğen samples for the C-O plot (close but not part of the profile):										
TU14A	GB 45233	0.40	4728	2,41	0,02	-0,85	0,06	18.07.2013		
TU14B	GB 45234	0.39	4659	2,34	0,02	-0,80	0,04	18.07.2013		
TU14C	GB 45235	0.41	5075	2,40	0,04	-0,78	0,03	18.07.2013		
TU14D	GB 45236	0.40	5248	2,34	0,03	-0,68	0,04	18.07.2013		
TÜ15-A	GB 47214	0.42	6033	1,41	0,03	-0,65	0,07	15.04.2014		
TÜ15-B	GB 47216	0.41	5006	1,41	0,03	-0,76	0,06	15.04.2014		
TÜ15-C	GB 47217	0.50	6422	1,46	0,02	-0,56	0,05	15.04.2014		
TÜ15-D	GB 47218	0.55	6993	1,59	0,01	-0,79	0,05	15.04.2014		
TÜ11-B	GB 47229	0.40	6073	1,66	0,03	-2,11	0,03	15.04.2014		
TÜ11	GB 45231	0.40	4588	1,74	0,04	-1,79	0,06	18.07.2013		
TÜ11-A	GB 47226	0.41	5915	1,58	0,02	-1,63	0,02	15.04.2014		

TÜ11-A	GB 47227	0.42	6109	1,61	0,02	-1,56	0,04	15.04.2014
TÜ16-A	GB 47231	0.61	8888	1,50	0,02	-0,95	0,05	15.04.2014
Fes1303-A	GB 47238	0.38	5122	1,36	0,03	-2,08	0,08	15.04.2014
Fes1303-A	GB 47239	0.40	5329	1,35	0,01	-2,05	0,03	15.04.2014
Fes1303-B	GB 47240	0.50	7788	1,62	0,02	-0,89	0,02	15.04.2014
Fes1304-B	GB 47260	0.48	6497	2,19	0,02	-1,76	0,03	16.04.2014
Fes1304-B	GB 47261	0.48	6569	2,23	0,03	-1,57	0,04	16.04.2014
Fes1304-D	GB 47251	0.45	6214	2,34	0,04	-1,22	0,08	15.04.2014
TU2	GB 45245	0.51	6169	2,13	0,04	-2,10	0,06	18.07.2013
TU1.2	GB 45230	0.38	4841	2,43	0,04	-0,93	0,04	18.07.2013
Bodrum								
Bod1506	GB 54312	0.49	7559	2,00	0,04	-1,77	0,02	15.12.2015
Bod1507	GB 54313	0.49	7877	1,59	0,04	-1,34	0,04	15.12.2015
Bod1505	GB 54683	0.51	7079	1,41	0,03	-0,81	0,04	14.01.2016
Bod1501-A	GB 54318	0.47	4810	2,27	0,04	-1,42	0,03	15.12.2015
Bod1501-B	GB 54319	0.47	6039	2,27	0,03	-1,65	0,05	15.12.2015
Bod1504	GB 54321	0.44	7358	0,99	0,02	-1,16	0,04	15.12.2015
Bod1502	GB 54322	0.48	5745	1,28	0,03	-1,76	0,06	15.12.2015
Ören								
Ören1502-A	GB 54244	0.40	7357	0,98	0,03	-1,18	0,08	24.11.2015
Ören1502-B	GB 54245	0.42	8590	0,97	0,03	-0,93	0,10	24.11.2015
Rock slab mapping								
FesBig A	GB 60483	0.1215	5208	2,20	0,04	-0,59	0,07	11.01.2017
FesBig B	GB 60479	0.124	5445	2,19	0,04	-0,48	0,03	11.01.2017
FesBig C	GB 60474	0.1085	4294	2,15	0,07	-0,44	0,03	11.01.2017
FesBig D	GB 60470	0.1175	5138	2,18	0,07	-0,75	0,03	11.01.2017
FesBig E	GB 60466	0.115	4833	2,23	0,05	-0,77	0,03	11.01.2017
FesBig F	GB 60460	0.116	5085	2,29	0,07	-0,58	0,06	11.01.2017
FesBig G	GB 60484	0.1045	4153	2,23	0,07	-0,74	0,04	11.01.2017
FesBig H	GB 60480	0.116	4662	1,73	0,05	-0,75	0,06	11.01.2017
FesBig I	GB 60476	0.1185	4742	2,18	0,06	-0,53	0,04	11.01.2017
FesBig J	GB 60471	0.132	5493	1,78	0,02	-1,16	0,05	11.01.2017
FesBig K	GB 60467	0.128	4635	1,80	0,05	-1,07	0,05	11.01.2017
FesBig L	GB 60461	0.119	4581	1,82	0,05	-1,22	0,06	11.01.2017
FesBig M	GB 60485	0.123	4724	1,69	0,06	-1,27	0,08	11.01.2017
FesBig N	GB 60481	0.121	4462	1,76	0,04	-1,13	0,03	11.01.2017
FesBig O	GB 60477	0.1445	5407	1,68	0,04	-1,15	0,07	11.01.2017
FesBig P	GB 60472	0.1185	5110	1,92	0,06	-0,77	0,02	11.01.2017
FesBig Q	GB 60468	0.1095	4652	2,21	0,09	-0,87	0,04	11.01.2017
FesBig R	GB 60464	0.1135	4969	2,27	0,08	-0,67	0,05	11.01.2017
FesBig S	GB 60493	0.1125	5403	2,15	0,06	-0,93	0,05	17.01.2017
FesBig T	GB 60482	0.1175	4814	2,10	0,04	-0,71	0,04	11.01.2017
FesBig U	GB 60478	0.1185	3120	1,76	0,06	-0,15	0,14	11.01.2017
FesBig V	GB 60473	0.113	909					signal too small
FesBig V	GB 60579	0.516	5366	1,33	0,06	-2,12	0,03	23.01.2017
FesBig W	GB 60469	0.1165	4999	2,23	0,06	-0,63	0,03	11.01.2017
FesBig X	GB 60465	0.1135	3749	1,93	0,04	-0,47	0,02	11.01.2017
FesBig Y	GB 60494	0.1245	5695	1,91	0,06	-0,82	0,06	17.01.2017
FesBig Z	GB 60495	0.1180	5460	2,24	0,04	-0,74	0,05	17.01.2017

FesBig 3	GB 60498	0.1215	4519	1,96	0,05	-1,12	0,03	17.01.2017
FesBig 4	GB 60499	0.1155	4408	1,86	0,10	-1,33	0,04	17.01.2017
FesBig 5	GB 60500	0.1155	3723	1,85	0,04	-0,28	0,06	17.01.2017
FesBig 6	GB 60501	0.1105	5356	2,20	0,07	-0,79	0,03	17.01.2017
FesBig 7	GB 60502	0.1115	4956	2,27	0,05	-0,52	0,06	17.01.2017
FesBig 8	GB 60504	0.1270	6031	2,18	0,03	-0,76	0,04	17.01.2017
FesBig 9	GB 60505	0.1105	5262	2,29	0,07	-0,40	0,05	17.01.2017
FesBig 10	GB 60506	0.1125	1250					signal too small
FesBig 10	GB 60580	0.4135	5229	1,66	0,06	-1,88	0,04	23.01.2017
FesBig 11	GB 60507	0.1420	6842	2,07	0,05	-0,61	0,04	17.01.2017
FesBig 12	GB 60508	0.1390	995					signal too small
FesBig 12	GB 60583	0.5030	4813	0,90	0,02	-2,08	0,02	23.01.2017

Excluded because they are located too far from the main mapping area:

FesBig 1	GB 60496	0.1105	4963	1,87	0,08	-1,10	0,03	17.01.2017
FesBig 2	GB 60497	0.1365	6815	1,94	0,06	-0,79	0,04	17.01.2017

Supplementary Data Table B: Sr isotopes

Dec 15

Standards	Value McArthur	Mean Value Bochum	± 2 s standard error	± 2 s standard diviation	number of repetitions [n]
NIST NBS 987	0,710247	0,710241	0,000002	0,000032	345
USGS EN-1	0,709175	0,709161	0,000002	0,000030	301

sample name or number	$^{87}Sr/^{86}Sr$ measured	± 2 s $_{mean}$	$^{87}Sr/^{86}Sr$ sample corrected to difference: NBS 987 value McArthur and NBS 987 measured with sample	$^{87}Sr/^{86}Sr$ sample corrected to difference: USGS EN-1 value McArthur and USGS EN-1 measured with sample	$^{87}Sr/^{86}Sr$ sample corrected to difference: NBS 987 value McArthur and NBS 987 Bochum mean value	$^{87}Sr/^{86}Sr$ sample corrected to difference: USGS EN-1 value McArthur and USGS EN-1 Bochum mean value
NIST NBS 987	0,710241	0,000005	0,710247	0,710211	0,710247	0,710255
Fes1578-B	0,707323	0,000005	0,707329	0,707293	0,707329	0,707337
Fes1570	0,707382	0,000006	0,707388	0,707352	0,707388	0,707396
Fes1575-A	0,707316	0,000005	0,707322	0,707286	0,707322	0,707330
Fes-1576	0,707388	0,000005	0,707394	0,707358	0,707394	0,707402
Fes1508	0,707507	0,000005	0,707513	0,707477	0,707513	0,707521
Fes1506	0,707520	0,000005	0,707526	0,707490	0,707526	0,707534
Fes1520	0,707473	0,000005	0,707479	0,707443	0,707479	0,707487
USGS EN-1	0,709205	0,000006	0,709211	0,709175	0,709211	0,709219
NIST NBS 987	0,710223	0,000005	0,710247	0,710239	0,710229	0,710237
Fes1517	0,707587	0,000006	0,707611	0,707603	0,707593	0,707601
Fes1525	0,707488	0,000005	0,707512	0,707504	0,707494	0,707502

Fes1523	0,707516	0,000005	0,707540	0,707532	0,707522	0,707530
Fes1513	0,707571	0,000005	0,707595	0,707587	0,707577	0,707585
Fes1527	0,707519	0,000005	0,707543	0,707535	0,707525	0,707533
Fes1545-A	0,707270	0,000005	0,707294	0,707286	0,707276	0,707284
Fes1552	0,707372	0,000005	0,707396	0,707388	0,707378	0,707386
Fes1560	0,707358	0,000005	0,707382	0,707374	0,707364	0,707372
USGS EN-1	0,709159	0,000005	0,709183	0,709175	0,709165	0,709173
NIST NBS 987	0,710231	0,000005	0,710247	0,710221	0,710237	0,710245
Kar1528-B	0,707339	0,000006	0,707355	0,707329	0,707345	0,707353
Kar1526	0,707401	0,000005	0,707417	0,707391	0,707407	0,707415
Fes1556-A	0,707309	0,000006	0,707325	0,707299	0,707315	0,707323
Kar1521	0,707448	0,000005	0,707464	0,707438	0,707454	0,707462
Kar1515	0,707332	0,000005	0,707348	0,707322	0,707338	0,707346
Fes1564-A	0,707394	0,000005	0,707410	0,707384	0,707400	0,707408
USGS EN-1	0,709185	0,000005	0,709201	0,709175	0,709191	0,709199
NIST NBS 987	0,710236	0,000005	0,710247	0,710249	0,710242	0,710250
Kar1518-A	0,707626	0,000006	0,707637	0,707639	0,707632	0,707640
Fes1503-A	0,707658	0,000005	0,707669	0,707671	0,707664	0,707672
Kar1520-A	0,707462	0,000005	0,707473	0,707475	0,707468	0,707476
Kar1505-B	0,707472	0,000005	0,707483	0,707485	0,707478	0,707486
USGS EN-1	0,709162	0,000005	0,709173	0,709175	0,709168	0,709176

June 2016

Standards	Value McArthur	Mean Value Bochum	± 2 s standard error	± 2 s standard diviation	number of repetitions [n]
NIST NBS 987	0,710247	0,710241	0,000002	0,000032	359
USGS EN-1	0,709175	0,709160	0,000002	0,000030	319

sample name or number	$^{87}Sr/^{86}Sr$ measured	± 2 s $_{mean}$	$^{87}Sr/^{86}Sr$ sample corrected to difference: NBS 987 value McArthur and NBS 987 measured with sample	$^{87}Sr/^{86}Sr$ sample corrected to difference: USGS EN-1 value McArthur and USGS EN-1 measured with sample	$^{87}Sr/^{86}Sr$ sample corrected to difference: NBS 987 value McArthur and NBS 987 Bochum mean value	$^{87}Sr/^{86}Sr$ sample corrected to difference: USGS EN-1 value McArthur and USGS EN-1 Bochum mean value
NIST NBS 987	0,710253	0,000005	0,710247	0,710278	0,710259	0,710268
Kar 1530	0,707281	0,000005	0,707275	0,707306	0,707287	0,707296
Fes 1522-A	0,707481	0,000008	0,707475	0,707506	0,707487	0,707496
Fes 1541-A	0,707287	0,000005	0,707281	0,707312	0,707293	0,707301
Fes 1511	0,707537	0,000005	0,707531	0,707562	0,707543	0,707552
Kar 1523-A	0,707473	0,000005	0,707467	0,707498	0,707479	0,707488
Fes 1573A	0,707320	0,000005	0,707314	0,707345	0,707326	0,707335
Fes 1501-A	0,707505	0,000005	0,707499	0,707530	0,707511	0,707520

1
2
3
4
5
6
7
8
9
10
11
12
13
14
15
16
17
18
19
20
21
22
23
24
25
26
27
28
29
30
31
32
33
34
35
36
37
38
39
40
41
42
43
44
45
46
47
48
49
50
51
52
53
54
55
56
57
58
59
60

Fes 1579	0,707339	0,000006	0,707333	0,707364	0,707345	0,707354
Kar 1503-A	0,707642	0,000006	0,707636	0,707667	0,707648	0,707657
Kar 1501	0,707687	0,000005	0,707681	0,707712	0,707693	0,707702
Fes 1519	0,707495	0,000005	0,707489	0,707520	0,707501	0,707510
USGS EN-1	0,709150	0,000005	0,709144	0,709175	0,709156	0,709165